

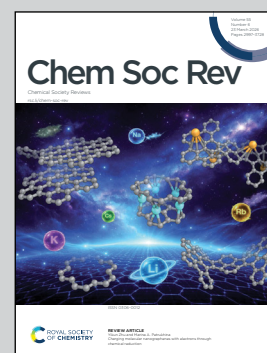
Showcasing research from Professor Juyoung Yoon's laboratory, Department of Chemistry and Nanoscience, Ewha Womans University, Seoul 03760, Republic of Korea.

Molecular fluorophore dimerization: a new paradigm for precision phototheranostics

Molecular dimerization introduces new excited-state manifolds beyond single chromophores. This review maps how dimer architectures regulate photophysical processes and biophysical behaviors, offering a unifying framework for the rational design of next-generation phototheranostics

Image reproduced by permission of Juyoung Yoon from *Chem. Soc. Rev.*, 2026, **55**, 3139.

As featured in:



See Dandan Ma, Yahui Chen, Xiaoqiang Chen, Xiaojun Peng, Juyoung Yoon *et al.*, *Chem. Soc. Rev.*, 2026, **55**, 3139.



Cite this: *Chem. Soc. Rev.*, 2026, 55, 3139

Molecular fluorophore dimerization: a new paradigm for precision phototheranostics

Hui Bian,^{id ae} Dandan Ma,^{*b} Yahui Chen,^{*b} Jeongyeon Hong,^{ad} Yi Nan,^{ad} Hai Xu,^{id a} Myung Hwa Kim,^{id e} Xiaoqiang Chen,^{*b} Xiaojun Peng^{id *c} and Juyoung Yoon^{id *ad}

Molecular fluorophore dimerization has recently emerged as a powerful and versatile design strategy in phototheranostics, offering a distinct regulatory regime that is fundamentally different from conventional single-molecule, polymeric, or aggregate-based systems. In this review, we present the first systematic and unified analysis of molecular dimerization as an independent paradigm for precision phototheranostics. Unlike previous reviews that primarily focus on isolated small-molecule fluorophores, polymeric architectures, or aggregates, this work highlights dimeric systems as an intermediate yet well-defined state that bridges molecular-level precision and collective-level functionality. We first comprehensively elucidate the fundamental photophysical mechanisms governing dimerization, and demonstrate how these processes uniquely regulate excited-state dynamics. Then, we reveal how dimerization enhances biophysical performance, such as controllable self-assembly and improved tumor accumulation. Representative dimeric systems across multiple dye families, including BODIPY, cyanine, porphyrins, donor–acceptor molecules, and metal complexes, are systematically categorized and analyzed, with an emphasis on structure–activity relationships and dimer-specific functional advantages in imaging-guided therapy. Finally, we discuss the current challenges and outline future directions, especially for artificial-intelligence-assisted molecular design. By positioning molecular dimerization as a distinct intermediate state between single molecules and higher-order assemblies, this review provides conceptual clarity and design principles for the development of next-generation phototheranostic agents.

Received 25th December 2025

DOI: 10.1039/d5cs01306b

rsc.li/chem-soc-rev

^a Department of Chemistry and Nanoscience, Ewha Womans University, Seoul 03760, Republic of Korea. E-mail: jyoon@ewha.ac.kr

^b College of Materials Science and Engineering, Shenzhen University, Shenzhen 518060, P.R. China. E-mail: madandan616@163.com, chenxq@szu.edu.cn

^c State Key Laboratory of Fine Chemicals, Frontiers Science Center for Smart Materials, Dalian University of Technology, Dalian, 116024, P.R. China.

E-mail: pengxj@dlut.edu.cn

^d Graduate Program in Innovative Biomaterials Convergence, Ewha Womans University, Seoul 03760, Republic of Korea

^e New and Renewable Energy Research Center, Ewha Womans University, Seoul 03760, Republic of Korea



Hui Bian

Hui Bian received his PhD in 2022 from Dalian University of Technology under the supervision of Prof. Yi Xiao. He subsequently worked as a Research Fellow at Nanyang Technological University before joining Prof. Juyoung Yoon's group at Ewha Womans University as a Postdoctoral Researcher in 2024. His research expertise centers on the design and synthesis of NIR-II small-molecule fluorescent dyes and the development of multifunctional phototheranostics.



Dandan Ma

Dandan Ma received her PhD in 2022 from Dalian University of Technology under the supervision of Prof. Xiaojun Peng and Yukui Zhang. She subsequently conducted postdoctoral research at Shenzhen University under the guidance of Prof. Xiaoqiang Chen and Lei Wang. Her research primarily focuses on developing novel and highly efficient photosensitizers for targeted cancer therapy and antimicrobial treatment.



1. Introduction

Phototheranostics has emerged as a transformative medical paradigm integrating diagnostic and therapeutic functions, thereby fundamentally reshaping contemporary disease management. By leveraging precise optical control, it enables exceptional spatiotemporal selectivity, offering distinct advantages in treating major diseases such as cancer, bacterial infections, inflammatory disorders, and Alzheimer's disease (AD).¹ Among its clinical applications, photodynamic therapy (PDT) has proven particularly effective in dermatology, where it is used to manage refractory skin conditions such as psoriasis and lupus erythematosus, providing non-invasive, targeted therapies that surpass the scope of conventional approaches.^{2,3}

Phototheranostics fundamentally relies on the precise manipulation of photophysical processes (Scheme 1).⁴⁻⁷ As illustrated in the Jablonski diagram, when photosensitizers (PSSs) absorb photons of specific wavelengths, their molecules transition to singlet excited states, whose energy is subsequently directed through multiple pathways to achieve theranostic functions.⁸⁻¹⁰ In particular, radiative transitions yield fluorescence signals suitable for precise lesion localization, while intersystem crossing (ISC) generates triplet states that participate in energy or electron transfer with environmental oxygen,

H₂O, or other biomolecules to produce reactive oxygen species (ROS) for photodynamic or photocatalytic effects. Alternatively, internal conversion (IC) and vibrational relaxation (VR) redirect the energy through non-radiative decay pathways to produce heat for photothermally induced cellular damage. This sophisticated framework for energy allocation enables phototheranostics to simultaneously deliver visible diagnostic effects and achieve effective therapeutic outcomes while providing real-time treatment feedback, thereby underscoring its substantial clinical value.¹¹

Small organic molecules have garnered particular attention in the development of photofunctional materials owing to their distinct advantages.^{2,12,13} Compared to nanomaterials, these molecular systems offer well-defined chemical structures, excellent reproducibility, tunable photophysical properties, and clear metabolic pathways, making them well-suited for precision medicine.¹⁴ Leveraging these attributes, recent efforts have focused on optimizing excited-state energy distribution efficiency through molecular engineering strategies to improve overall performance (Scheme 1).⁸ For example, in imaging-guided applications, researchers have developed high-brightness, target-specific fluorescent probes while actively exploring near-infrared (NIR)-II imaging technologies to address tissue penetration limitations.¹⁵⁻¹⁸ In PDT optimization, both traditional heavy-atom strategies



Yahui Chen

Yahui Chen received his PhD in 2020 from Nanjing Tech University under the supervision of Prof. Xiaoqiang Chen. He then worked as a Postdoctoral Fellow in the group of Prof. Juyoung Yoon at Ewha Womans University. He is currently an Assistant Professor at Shenzhen University. His research interests focus on the design and development of organic smart photoresponsive materials.



Jeongyeon Hong

Jeongyeon Hong earned her BS degree at Ewha Woman's University, and continued her Master's study from 2025 at Ewha Womans University. Her main research interest is organic fluorescent materials design for phototheranostics.



Yi Nan

Yi Nan earned her BS degree at Shandong University in 2023. Currently, she is pursuing her Master degree under the supervision of Prof. Juyoung Yoon at Ewha Woman's University. Her research interest is focused on small molecular fluorophores design and imaging.



Hai Xu

Hai Xu received his PhD degree from the Southwest Jiaotong University in 2023. Then he joined Prof. Juyoung Yoon's group as a postdoctoral researcher. His current interests include the design and development of fluorescent chemosensors, molecular recognition, and NIR-II imaging and therapy.



(incorporating Br, I, and Se) designed to promote ISC and innovative heavy-atom-free mechanisms, including spin-orbit charge transfer (SOCT), symmetry-breaking charge transfer (SBCT), resonance energy transfer (RET), and donor-acceptor (D-A) structural optimization, have been explored.^{19–21} Similarly, in photothermal therapy (PTT), approaches such as photo-induced electron transfer (PET), twisted intramolecular charge transfer (TICT), and intramolecular motion regulation have been employed to improve non-radiative decay channels.^{22,23}

However, prevailing research paradigms remain constrained by several critical limitations. Specifically, most studies have primarily addressed single-molecule system design, paying limited attention to collective molecular effects. These studies have leveraged phenomena such as aggregation-induced emission (AIE) and J-aggregation to modulate excited-state behaviors, offering distinct advantages.²⁴ For instance, J-aggregation not only induces spectral red-shifting but also narrows the singlet-triplet energy gap, thereby enhancing photodynamic efficacy.²⁵ However, the stability of the resulting assembled structures under complex biological conditions has typically been overlooked. Specifically, biological microenvironments,

such as lipid bilayers and hydrophobic protein pockets, can disassemble these structures, resulting in substantial degradation of optical performance. Moreover, while macromolecular systems such as organic semiconductor polymers exhibit favorable optical properties through strong D-A interactions and energy-level splitting, they continue to face inherent limitations, including poor reproducibility and limited biocompatibility.

In response, intramolecular dimerization has been proposed as a critical bridge between single-molecule design and supramolecular assembly or polymerization.^{26–28} By integrating two chromophores into a single molecular framework *via* covalent bonding or self-assembly, this strategy imparts unique photo-physical and biophysical properties while preserving molecular structures. Moreover, it facilitates energy transfer, charge separation, and exciton coupling between chromophores through spatial confinement, enabling precise regulation of excited-state behavior. For example, boron-dipyrromethene (BODIPY) dimers have been reported to exhibit markedly enhanced triplet yields *via* SOCT and SBCT. Dimerization also improves absorption characteristics and increases two-photon absorption cross-sections. Beyond these optical advantages, this strategy also



Myung Hwa Kim

Myung Hwa Kim received his PhD in 2006 from State University of New York at Stony Brook (Stony Brook University). Now, he is a full professor at the Department of Chemistry and Nanoscience, Ewha Womans University.



Xiaoqiang Chen

Xiaoqiang Chen received his PhD in 2007 from the State Key Laboratory of Fine Chemicals at Dalian University of Technology under the supervision of Prof. Xiaojun Peng. Now, he is a full professor at Shenzhen University, specializing in organic/supramolecular photochemistry, biological sensors, and mRNA delivery materials.



Xiaojun Peng

Xiaojun Peng received his PhD in 1990 at Dalian University of Technology. After completing postdoctoral research at Nankai University (China), he has worked at the Dalian University of Technology since 1992. In 2001 and 2002 he was a visiting scholar at Stockholm University and Northwestern University (USA). Currently he is the director of the State Key Laboratory of Fine Chemicals at Dalian University of Technology. His research interests cover dyes for fluorescent bio-imaging/labelling and digital printing/recording.



Juyoung Yoon

Juyoung Yoon is a distinguished professor at the Department of Chemistry and Nanoscience, Ewha Womans University. He received his PhD (1994) from Ohio State University and conducted his postdoctoral work at UCLA and Scripps Research Institute. His research interests include investigations of fluorescence imaging probes, photo therapy and theranostics. He has been listed as a highly cited researcher in chemistry since 2014.



enables fine-tuning of key parameters such as molecular hydrophobicity, rigidity, and self-assembly propensity to optimize pharmacokinetics.⁵ A representative example includes cyanine dye dimers linked by flexible spacers that enhance water solubility and promote ordered self-assembly, thereby achieving efficient tumor targeting without carrier assistance.

While numerous reviews have systematically summarized the advances in small molecules, polymers, AIE systems, and J/H-aggregated frameworks for phototheranostics, the molecular dimerization strategy remains underexplored. To bridge the aforementioned gap, this review systematically examines the mechanisms by which molecular dimerization enhances photophysical processes and biophysical properties. It also assesses design principles and recent progress across dimeric systems, including BODIPY, cyanines, porphyrins, D-A molecules, and metal complexes. Furthermore, it identifies prevailing technical challenges alongside future directions, with particular emphasis on artificial-intelligence-driven approaches in the field. Overall, by establishing a comprehensive framework for molecular dimerization, this review seeks to equip researchers in chemistry, chemical biology, materials science, and medicine with both a solid theoretical foundation and new avenues for innovation.

Notably, in the rapidly advancing field of phototheranostics, molecular dimerization marks a pivotal shift from single-function optimization toward collaborative design. It not only deepens the current understanding of intermolecular interactions but also establishes new directions for the development of next-generation intelligent theranostic systems. As insights into photophysical behavior continue to expand and synthetic technologies evolve, molecular dimerization is poised to open a new chapter in precision medicine.

2. Regulating molecular properties through dimerization

Current rational strategies for modulating excited-state energy distributions are broadly categorized into single-molecule design, polymeric engineering, and aggregation-based approaches, each aiming to precisely control the fate of excited-state energy, either by promoting ISC to generate ROS or facilitating IC and VR to produce heat. To contextualize these strategies, Scheme 1 summarizes key design approaches and assembly modes, illustrating how structural modifications reshape excited-state energy landscapes and regulate their associated competitive photophysical pathways.^{2,27,29–31}

Molecular dimerization represents an intermediate yet highly versatile design paradigm serves as a bridge between single-molecule engineering and polymeric/aggregate-level modulation. Dimeric systems maintain molecular discreteness while exploiting the exciton resonance or electron-transfer interactions between identical chromophores to generate new excited-state configurations and precisely modulate energy-flow pathways. Unlike complex monomer-level modifications, dimerization can be achieved using straightforward and rational linkages while avoiding the biocompatibility and targeting limitations often associated with polymeric architectures (Fig. 1).

This strategy also offers distinct advantages beyond those of monomeric and aggregated systems, including enhanced light-harvesting capacity (*e.g.*, high molar extinction coefficients) and substantially improved nonlinear optical responses, such as two-photon absorption (*e.g.*, doubled σ_2 values), collectively boosting the optical performance essential for phototheranostics. Positioned at the boundary between isolated chromophores and bulk assemblies, molecular dimers combine the

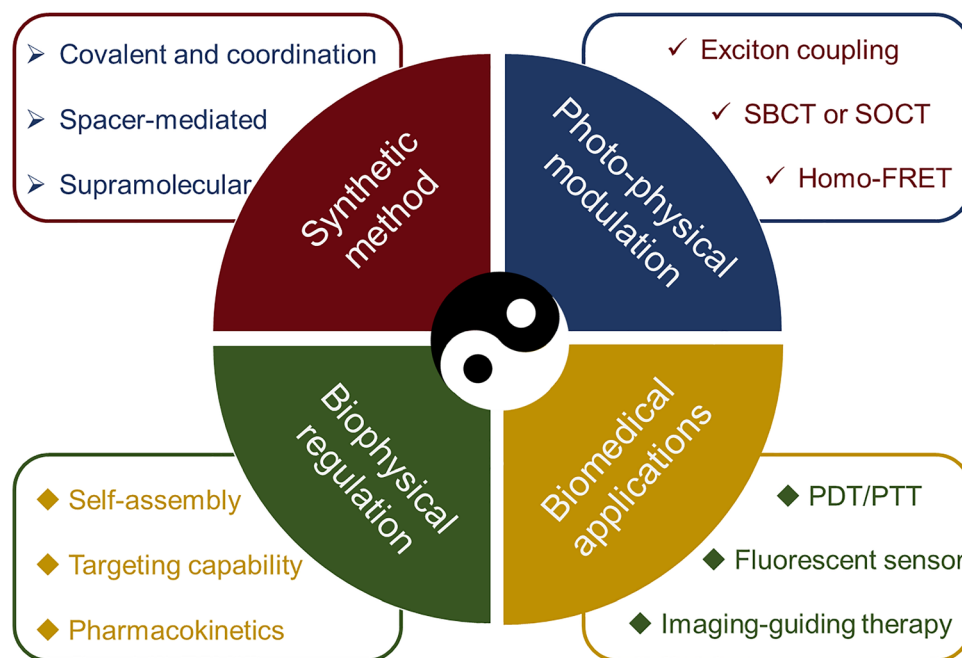


Fig. 1 Construction strategies, photophysical performance modulation approaches, and representative applications of molecular dimers.



advantages of both regimes, namely enhanced energy coupling, tunable photophysical behaviors, and integrated multifunctionality, offering a promising structural blueprint for next-generation intelligent phototheranostic agents.

2.1 Construction strategies for molecular dimers

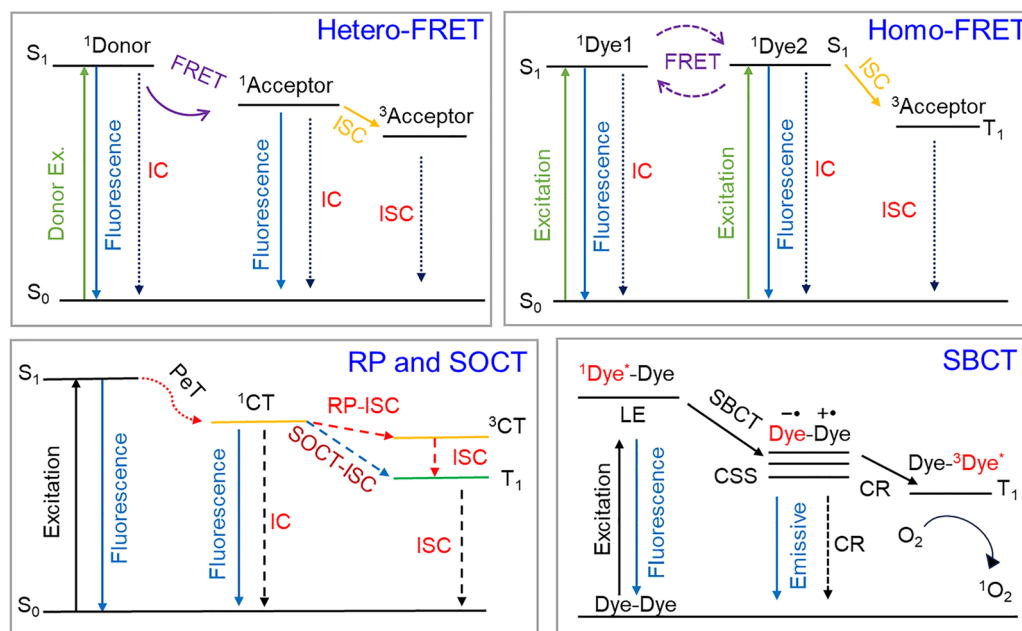
Molecular dimers are broadly classified as intramolecular or intermolecular variants, depending on their linkage mode. Their construction typically follows three primary strategies, each defined by specific bonding modes that shape their photophysical properties. (1) Covalent or coordination linkages employ direct σ -bonds or metal coordination centers to form structurally rigid dimers with fixed interchromophore distances and orientations, thereby enabling strong electronic coupling and promoting efficient energy transfer. A notable example includes orthogonally arranged dimers connected *via* single bonds, which facilitate SBCT and substantially enhance triplet-state generation. (2) Spacer-mediated connections use flexible alkyl or glycol chains and rigid aromatic bridges to link chromophores. The length and flexibility of the spacer directly govern the balance between conformational freedom and electronic communication. Specifically, short spacers promote Förster resonance energy transfer between identical fluorophores (homo-FRET) *via* dipole-dipole interactions, whereas optimized chain lengths support controlled PET, enabling precise modulation of excited-state dynamics.

(3) Supramolecular self-assembly leverages non-covalent interactions, including π - π stacking, hydrophobic effects, and electrostatic forces, to drive spontaneous dimer formation. These dynamic assemblies exhibit J- or H-aggregate-like behavior, characterized by strong exciton coupling and efficient interchromophore energy transfer. The responsive nature of these non-covalent interactions allows structural reorganization

across diverse environments while preserving intermolecular communication essential for modulating photophysical properties. Each of these strategies contributes distinctive advantages in controlling molecular arrangement and electronic interactions, thereby enabling the targeted design of dimeric systems for phototheranostic applications.

2.2 Photophysical properties

Intramolecular dimerization, a refined molecular design strategy, actively couples the excited-state dynamics of two chromophores by covalently confining them within a nanoscale range (typically < 2 nm), thereby eliminating passive reliance on concentration-driven encounters. This precise spatial preorganization enables a coordinated cascade of photophysical processes, resulting from the interplay among exciton coupling, energy migration, CT, and competitive non-radiative relaxation. Among these, exciton coupling reshapes the absorption profile through energy-level splitting and spectral shifts, while efficient homo-FRET drastically suppresses fluorescence anisotropy and promotes energy dissipation across the dimeric network (Scheme 2).^{32,33} The close proximity between chromophores in intramolecular dimers further facilitates photoinduced CT, PET, and most notably, highly efficient SOCT-ISC, which collectively reconfigure the distribution of excited-state energy. Consequently, both the emissive characteristics, namely intensity, wavelength, and lifetime, and the distribution of excited-state populations between singlet and triplet states are systematically modulated. This inherent “programmability” of photophysical behavior underpins its pivotal role in advanced theranostics. Specifically, leveraging aggregation-caused quenching (ACQ) or PET supports the development of “turn-on” fluorescent probes with minimal background for ultra-sensitive detection. Further, maximizing SOCT-ISC efficiency through rational design directs



Scheme 2 Representative photophysical modulation strategies in molecule dimer.



excitation energy into triplet states, thereby enhancing singlet oxygen generation for improved PDT. Conversely, augmenting non-radiative decay *via* strong ACQ effects or intramolecular CT efficiently converts photons into heat, yielding potent photothermal agents. Thus, intramolecular dimerization transcends mere molecular addition; it represents a foundational paradigm for designing photofunctional materials through the deliberate control of intramolecular interactions, thereby unlocking vast opportunities for next-generation theranostic platforms.

(1) **Homo-FRET.** The homo-FRET mechanism, defined by rapid dipole–dipole-mediated energy transfer between spatially proximate and optimally oriented chromophores in intramolecular dimers, forms an efficient energy migration network that substantially affects therapeutic efficacy.^{34,35} Although this process does not produce detectable changes in absorption or emission spectra, it enables excitation energy transfer to quenching sites through depolarization-induced effects. Notably, the functional role of homo-FRET differs considerably between photothermal and photodynamic applications. Specifically, in PTT, it facilitates non-radiative decay by channeling excitation energy into molecular vibrations, thereby enhancing photothermal conversion efficiency (PCE). However, in PDT, it acts as a competitive energy dissipation pathway that suppresses triplet-state formation by interfering with ISC, ultimately lowering singlet oxygen quantum yields (Φ_{Δ}). This functional divergence necessitates strategic molecular design, where homo-FRET is suppressed to optimize PDT sensitizers and enhanced to improve the performance of PTT agents.

(2) **SBCT.** SBCT is a distinct photophysical process occurring in molecular dimers formed by two identical chromophores.^{36–38} It is characterized by the spontaneous symmetry breaking of the delocalized excited state upon photoexcitation, producing a charge-separated state wherein the hole and electron localize on different chromophores, yielding a Dye⁺–Dye[–] configuration (Scheme 2).^{39,40} Beyond its spectroscopic manifestations, SBCT also functions as a dynamic relaxation pathway for the excited state and occurs only when three fundamental conditions are met. First, the excitation energy of the monomeric chromophore must be nearly degenerate with or exceed the redox gap of the dimer to permit thermodynamically favorable charge separation. Second, the chromophores must be arranged to minimize orbital overlap and excitonic coupling, typically through an orthogonal geometry. Third, the inter-chromophore distance must be sufficiently short to enable rapid intramolecular electron transfer, allowing SBCT to outcompete singlet-state decay pathways such as fluorescence and non-radiative relaxation. Notably, SBCT is characterized by ultrafast formation kinetics; discernible spectral signatures of the charge-separated state in transient spectroscopy; and a notably low exchange energy between the resulting singlet and triplet states, which is a direct result of the orthogonal chromophore geometry. This low exchange energy renders the SBCT state an efficient intermediate to the localized triplet state, supporting its application in PDT. Specifically, by promoting ISC to long-lived triplet states, SBCT facilitates effective singlet oxygen sensitization and offers a sophisticated molecular design strategy for developing novel, heavy-atom-free PSS with high therapeutic value.

(3) **SOCT-ISC.** SOCT-ISC is an efficient triplet-state-generation mechanism prominent in orthogonal D–A dyads, with a near-orthogonal spatial arrangement between the electron donor and acceptor units.^{41,42} This configuration suppresses ground-state orbital overlap while enabling rapid formation of a singlet charge-transfer (¹CT) state upon excitation.⁴³ Upon photoexcitation, either the donor or the acceptor is promoted to its locally excited singlet state. From this state, a rapid photoinduced electron transfer occurs from the donor to the acceptor, yielding ¹CT. The subsequent charge recombination process is the key step that governs triplet formation. Two distinct pathways can operate during recombination: in the first, the radical pair undergoes intersystem crossing to form a triplet charge-transfer state (³CT), which then relaxes to the locally excited triplet state (T_1) of either the donor or acceptor. In the second, more direct pathway, charge recombination populates the local triplet state directly *via* SOCT-ISC. In this process, the large change in orbital angular momentum associated with electron back-transfer compensates for the required spin flip, thereby conserving total angular momentum and enabling highly efficient ISC in the absence of heavy atoms.

SOCT-ISC is conceptually related to SBCT, as both mechanisms exploit orthogonal molecular geometries to minimize exchange energy in the charge-transfer state and promote spin conversion. However, a fundamental distinction lies in molecular symmetry: SBCT occurs in homodimeric systems composed of identical chromophores, whereas SOCT-ISC is intrinsic to heterodimeric donor–acceptor architectures. This structural asymmetry provides additional degrees of freedom for tuning electronic coupling, energy-level alignment, and redox properties, making SOCT-ISC a particularly versatile design principle for heavy-atom-free photosensitizers in photodynamic therapy and related photochemical applications.

(4) **Exciton coupling mediated by intramolecular aggregation.** In molecular dimer systems, covalent linkages not only reduce the spatial separation between chromophores but also determine their packing arrangement and govern excited-state coupling through precise spatial pre-organization. These linkages facilitate strong intramolecular interactions between the two fluorophores, particularly promoting vibrational coupling, exciton coupling, and energy transfer processes, which often manifest as self-quenching phenomena. Given the identical nature of the chromophores, photoexcitation can promote the vibrational coupling of excited states and facilitate energy-level degeneracy, resulting in photophysical characteristics distinct from those of monomeric systems, such as reduced excitation energies and narrowed singlet–triplet energy gaps. These modified excited-state properties create favorable conditions for either enhanced ISC or increased vibrational relaxation, depending on the specific therapeutic application, thereby improving performance in photodynamic or photothermal modalities.

Molecular aggregation encompasses several structural arrangements, most notably categorized as H-aggregation and J-aggregation according to the assembly geometry, with each exhibiting distinct excitonic coupling characteristics and energy distribution profiles.^{44,45} Among these, H-aggregation constitutes the most



characteristic packing arrangement, defined by a parallel “face-to-face” stacking setup of chromophores that results in strong excitonic coupling, typically evidenced by a blue shift in the absorption spectrum. In contrast, J-aggregation adopts a “head-to-tail” orientation, generally accompanied by red-shifted and spectrally sharpened absorption features. Notably, upon aggregation, excitation is no longer confined to individual molecules but becomes delocalized through long-range excitonic coupling, thereby transforming the excited state into a collective property and altering the system’s electronic energy landscape. From a photophysical standpoint, such close packing results in a dual character: π -stacking interactions can effectively bridge the singlet–triplet energy gap, theoretically enhancing ISC and promoting singlet oxygen generation; however, aggregation concurrently establishes highly efficient non-radiative decay channels, wherein energy dissipation through VR substantially outcompetes that through radiative channels. Consequently, although the reduced energy gap theoretically favors triplet state formation, the excited-state energy is more readily converted into heat *via* non-radiative pathways, markedly suppressing ISC. This intrinsic competition dictates the functional orientation of aggregated systems. Specifically, their superior heat conversion capacity is advantageous for PTT, whereas efficient PDT can be achieved through precise molecular engineering to balance non-radiative relaxation against ISC for optimal singlet oxygen yields.

Notably, dimer systems offer an innovative platform for enabling controlled intramolecular aggregation. Although individual small molecules can also aggregate *via* intermolecular interactions, the structural stability of such assemblies under biological conditions remains limited. Specifically, the complexity of the biological environment, rich in phospholipids, proteins, and other biomacromolecules, combined with the inherent hydrophobicity of most phototheranostic agents, raises valid concerns regarding potential disassembly in physiological environments. Dimeric architectures address this challenge through covalent pre-organization, thereby preserving aggregation behavior and ensuring consistent phototherapeutic performance in biological applications.

2.3 Biophysical properties

In addition to its profound impact on photophysical tuning, dimerization also substantially alters the biophysical properties of functional molecules. Specifically, structural changes induced by dimerization, including modified rigidity and flexibility, hydrophilicity and hydrophobicity, and intermolecular interactions, critically influence molecular behavior in biological environments. Recent studies have demonstrated that dimerization can impart improved self-assembly to otherwise poorly soluble or highly hydrophobic drug molecules, facilitating the formation of stable nanoparticles (NPs).^{46–48} Such assemblies typically offer prolonged blood circulation, enhanced tumor accumulation, improved cellular uptake, and increased drug stability, thereby augmenting therapeutic efficacy. Notably, homodimeric prodrugs have been shown to achieve drug-loading capacities exceeding 60%, thereby reducing dependence on external carriers. Anticancer drugs bearing planar aromatic moieties, such as

doxorubicin, camptothecin, and SN-38, often undergo strong π - π stacking upon dimerization, resulting in their precipitation in aqueous media. To mitigate this issue, molecular defects are commonly introduced through flexible linkers (*e.g.*, sulfide bonds) or rotatable σ -bonded bridging groups (*e.g.*, phenylene), which reduce rigidity and inhibit long-range ordered packing. Collectively, these findings underscore dimerization as a powerful strategy not only for manipulating photophysical states but also for modulating biophysical properties and enhancing the therapeutic potential of small molecules.

The prototype Cy7 exhibits pronounced hydrophobicity, limited tumor accumulation, and low PCE owing to its dominant radiative decay pathways. To overcome these challenges, Peng and co-workers⁴⁹ developed a series of *ortho*-, *meta*-, and *para*-linked Cy7 dimers using phenyldithiol bridges (Fig. 2). This covalent dimerization strategy not only modified the dyes’ electronic structures but also reshaped their supramolecular behavior. Photophysically, this dimerization resulted in intramolecular H-aggregation and PET, resulting in nearly complete fluorescence quenching and markedly enhanced nonradiative decay. Consequently, the dimers exhibited substantially higher PCEs than the Cy7 monomer (74.1% for the *meta*-dimer *versus* 17.2% for the monomer), in agreement with their stronger photoacoustic signals. Biophysically, dimerization mitigated the solubility and stability limitations of monomeric Cy7. Accordingly, the dimers spontaneously assembled into NPs approximately 100 nm in diameter, exhibiting excellent colloidal stability and prolonged circulation. In particular, the *para*-dimer exhibited the most favorable pharmacokinetic profile and tumor accumulation, resulting in superior *in vivo* anticancer efficacy.

ICG, the only NIR dye approved by the Food and Drug Administration (FDA), exhibits excellent solubility and biosafety; however, its clinical application in PDT and PTT remains limited by poor photostability, rapid clearance, and insufficient tumor specificity.⁵⁰ To address these limitations, Zhou and co-workers⁵¹ developed a zwitterionic ICG dimer (ICG-tk-ICG) incorporating a thioketal linker to modulate intermolecular interactions (Fig. 3). Notably, this dimer self-assembles into zwitterionic NPs (ZN-dICG) with an ultra-low critical micelle concentration ($< 6.5 \times 10^{-8}$ M) and high colloidal stability. Photophysically, ZN-dICG undergoes fluorescence self-quenching and demonstrates markedly enhanced PCE (55.1% *vs.* 19.4% for ICG) and increased ROS generation. The aggregates display a characteristic shoulder peak at 700–730 nm, indicative of H-type interactions,

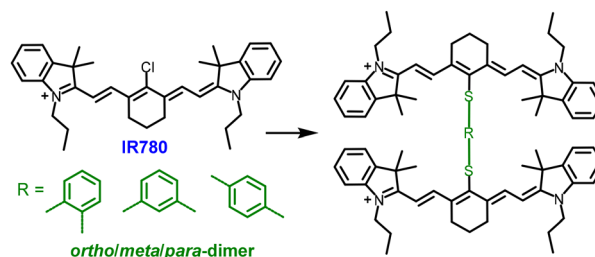


Fig. 2 Cyanine (IR780) dimers bearing *ortho*-, *meta*-, and *para*-substituted phenyl units.



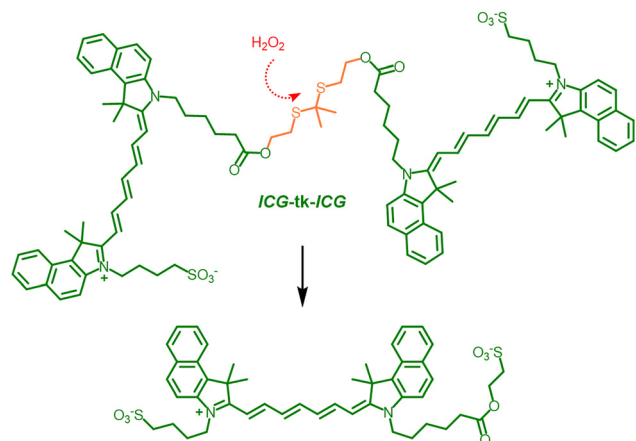


Fig. 3 Chemical structure and oxidative cleavage mechanism of the indocyanine green (ICG) dimer ICG-tk-ICG.⁵¹

with fluorescence nearly fully quenched in aqueous solutions, thereby promoting nonradiative decay and thermal energy generation. Biophysically, ZN-dICG exhibits robust colloidal stability in biological media, prolonged circulation, and enhanced tumor accumulation through the enhanced permeability and retention (EPR) effect. Within the tumor microenvironment, elevated levels of ROS cleave the tk linker, releasing free ICG. The released ICG binds to albumin, enhancing NIR fluorescence and thereby improving the signal-to-background ratio in tumor imaging. *In vivo*, ZN-dICG enables the sensitive detection of both primary and metastatic tumors and facilitates efficient tumor ablation under NIR laser irradiation, underscoring its translational potential as a biocompatible phototheranostic platform.

3. Dimeric dyes for phototheranostics: a spectrum of structural diversity

3.1 BODIPY dimers

BODIPY dyes have emerged as among the most attractive classes of PSs owing to their distinctive combination of properties, including high molar absorption coefficients, elevated fluorescence quantum yields, excellent photochemical stability, synthetic accessibility, and favorable biocompatibility.^{52,53} Conventional strategies aimed at boosting their photodynamic performance have targeted ISC by incorporating heavy atoms (*e.g.*, Br and I) at the β -position to facilitate singlet–triplet transitions. Although these approaches have enhanced triplet yield, they have also introduced drawbacks such as shortened triplet lifetimes, dark toxicity, and diminished compatibility with biomedical applications.

To overcome these limitations, heavy-atom-free designs, such as orthogonal D–A structures and configurations with enhanced D–A strength, have emerged as viable alternatives. Because ROS generation depends on ISC efficiency, recent strategies have further aimed to enhance spin conversion by incorporating spin-converting units, engineering D–A systems, or extending π -conjugation.⁵⁴ Notably, BODIPY dimerization



Fig. 4 Standard numbering system for positions on the BODIPY molecule.

has emerged as a potent strategy for promoting ISC and ROS generation. The simplest method involves linking two BODIPY units *via* a single bond, and the abundance of tunable sites on the core supports versatile dimer architectures. Reported dimeric motifs include α , α -; β , β -; *meso*, *meso*-; β , *meso*-; α , *meso*-; α , β -; and α , γ -linked BODIPYs (Fig. 4). Alternatively, flexible chains or aromatic spacers are often used to connect BODIPY units, maintaining intramolecular flexibility and enabling a detailed mechanistic analysis of dimerization-induced photophysical behavior. Collectively, these developments underscore dimerization and other heavy-atom-free approaches as effective means of overcoming the inherent limitations of BODIPY dyes in PDT.

3.1.1 Direct linkage of two BODIPY molecules at the α -, β -, γ -, and *meso* positions

(1) α - α and β - β -linked BODIPY dimers. In 2008, Flamigni *et al.*^{55,56} synthesized a series of α , α -(3,3')-linked BODIPY dimers and systematically compared their photophysical properties to those of their monomers (Fig. 5 and Table 1). Their findings revealed that while the monomers typically exhibited a single absorption band near 530 nm and emission centered around 540 nm, with quantum yields approaching unity, the synthesized dimers displayed exciton-split absorption bands and a pronounced Stokes shift in emission while retaining high absorption and fluorescence efficiency. As shown in Fig. 5, Mon1 exhibited a primary absorption peak at 534 nm, whereas Dim1 showed bifurcated bands at 492 and 565 nm, reflecting strong excitonic coupling and distinct exciton splitting between the two BODIPY units. Notably, although the fluorescence quantum yields and lifetimes of these dimers in toluene were comparable to those of the monomers, they proved highly sensitive to solvent type, exhibiting substantially diminished luminescence and shorter lifetimes in acetonitrile. More importantly, the dimers exhibited markedly stronger triplet absorption and considerably higher $^1\text{O}_2$ yields, reaching approximately 0.4 in toluene and 0.5 in dichloromethane, compared to less than 0.1 for the monomers. Overall, this study pioneered the field of BODIPY-dimer-based PS design and demonstrated that such dimers can serve as efficient singlet-oxygen-generating agents with appropriate solvent selection.

Similar to Flamigni's group, Jiao's group⁵⁷ also designed and synthesized α , α -linked bisBODIPYs (Fig. 6) but subsequently functionalized them with one or two TPE moieties to produce TPEB and 2TPEB. Here, incorporating TPE extended the π -conjugation of the BODIPY core, yielding red-shifted absorption and emission ($\lambda_{\text{abs/em}} = 740/810$ nm) and enabling aggregation-induced emission near 912 nm. Upon self-assembly with the surfactant F-127, the resulting NPs efficiently generated



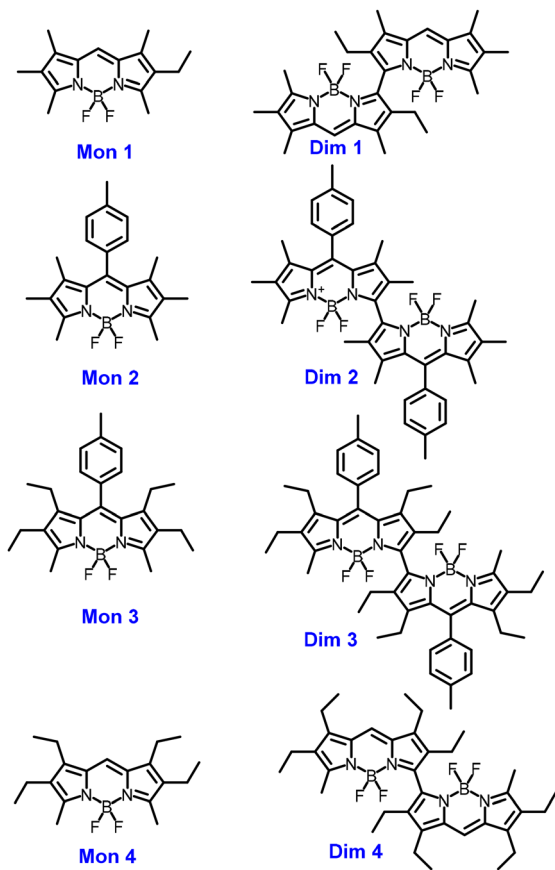


Fig. 5 Chemical structures of representative α - α -linked BODIPY dimers.

ROS ($^1\text{O}_2$ and $\cdot\text{OH}$) and achieved high PCE (68%). Mechanistically, the electron-rich TPE donors and electron-deficient BODIPY acceptors established a D-A structure, which enhanced spin-orbit coupling and narrowed the S_1 - T_1 energy gap, thereby facilitating ISC and ROS production. The rotational flexibility of TPE further promoted nonradiative decay, improving

photothermal performance. Compared to the monomer and commercial ICG, 2TPEB NPs demonstrated superior ROS generation, photothermal stability, and antitumor efficacy (half-maximal inhibitory concentration, $\text{IC}_{50} = 4.1 \mu\text{M}$), underscoring their potential as high-performance phototheranostic agents.

(2) α -Meso-, β -meso-, and meso-meso-linking. Shinokubo and co-workers⁵⁸ synthesized β , β -linked BODIPY dimers and trimers (Fig. 7), wherein the BODIPY cores adopted a coplanar geometry with minimal steric hindrance, facilitating extended π -conjugation. This configuration produced notably red-shifted absorption maxima compared to the monomer (501 nm for the monomer, 609 nm for the dimer, and 678 nm for the trimer). However, this enhanced conjugation was accompanied by a decline in fluorescence quantum yield, dropping from 0.92 (monomer) to 0.15 (dimer) and 0.25 (trimer). Although extended conjugation may promote triplet-state formation, the singlet oxygen generation efficiency of these oligomers was not assessed in that study. Xie *et al.*⁵⁹ later synthesized a series of β - β -linked BODIPY oligomers (D1–D3 and T1) to investigate the influence of substituent groups and oligomer size on singlet oxygen generation. These dimers and trimers exhibited low $^1\text{O}_2$ quantum yields in dimethyl sulfoxide (DMSO), specifically, 0.10 for D1, 0.11 for D2, 0.08 for D3, and 0.06 for T1. These values were substantially lower than those of analogues linked at alternative positions. This poor performance was attributed to two primary factors: (1) distorted dihedral angles between adjacent BODIPY units (55° for D1 and 64° for D2), which hindered efficient ISC; and (2) electron-rich substituents that stabilized the intramolecular CT state, thereby suppressing singlet-to-triplet conversion. Consequently, although these β - β -linked oligomers maintained high fluorescence efficiencies, their capacity for ROS sensitization remained limited.

In 2011, Akkaya *et al.*⁶⁰ first performed theoretical calculations to demonstrate that doubly substituted BODIPY molecules (Fig. 8), particularly those adopting orthogonal conformations,

Table 1 Photophysical parameters (absorption/emission maxima and fluorescence quantum yields) and ROS generation efficiencies of monomers and α - α - and β - β -linked BODIPY dimers

Molecules	λ_{abs} (nm)	λ_{em} (nm)	Φ_{F}	ROS type	Φ_{Δ}	Synthetic yield	Ref.
Mon 1	534	540	1.0	$^1\text{O}_2$	≤ 0.1	69%	55 and 56
Dim 1	492/565	648	0.71	$^1\text{O}_2$	0.4	45%	
Mon 2	526	538	0.88	$^1\text{O}_2$	≤ 0.1	42%	57
Dim 2	489/558	638	0.67	$^1\text{O}_2$	0.4	65%	
Mon 3	529	538	0.80	—	—	45%	58
Dim 3	490/559	638	0.69	$^1\text{O}_2$	0.3	65%	
Mon 4	535	540	1.0	—	—	—	59
Dim 4	494/567	650	0.76	$^1\text{O}_2$	0.3	45%	
BDP	663	703	0.71	—	—	—	57
TPEB	702	774	0.15	$\cdot\text{OH}$, $^1\text{O}_2$	—	30%	
2TPEB	742	810	0.11	$\cdot\text{OH}$, $^1\text{O}_2$	—	22%	58
Mon 5	501	514	0.92	—	—	—	
Dim 5	609	655	0.15	—	—	81%	59
Tri 1	678	731	0.25	—	—	71%	
D1	534	572	0.06	$^1\text{O}_2$	0.10	26%	59
D2	526	564	0.02	$^1\text{O}_2$	0.11	22%	
D3	559	597	0.11	$^1\text{O}_2$	0.08	45%	
T1	559	599	0.10	$^1\text{O}_2$	0.06	8%	



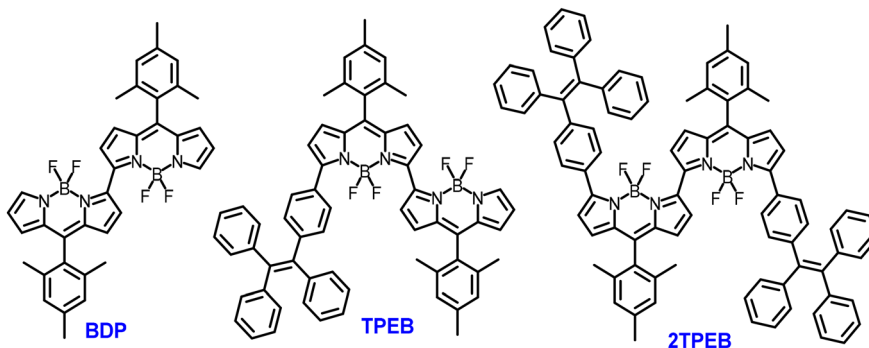


Fig. 6 Chemical structures of boron-dipyrromethene (BDP), tetraphenylethene-functionalized BDP (TPEB), and bis-tetraphenylethene-functionalized BDP (2TPEB).

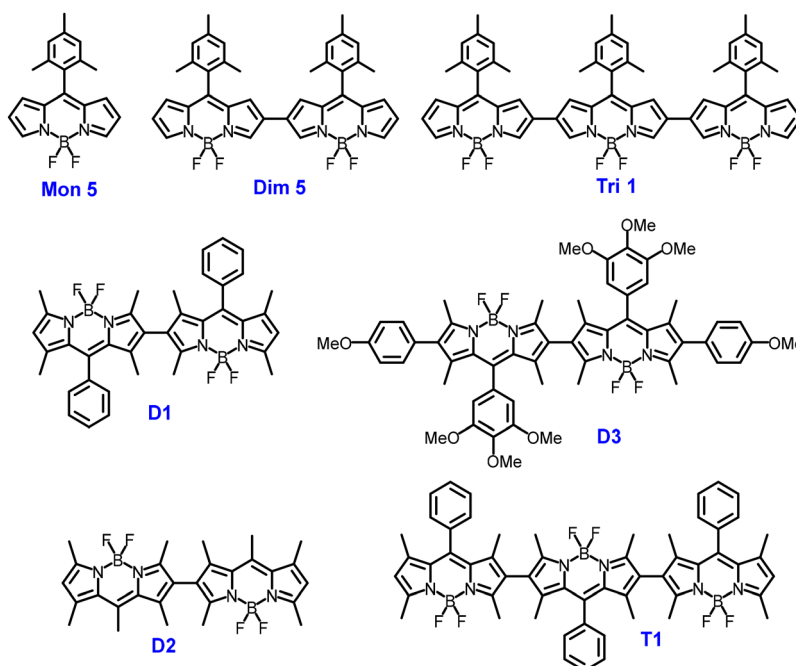


Fig. 7 Chemical structures of representative β,β -linked BODIPY dimers and trimers.

substantially enhance S_1 - T_1 coupling efficiency. Building on this insight, they synthesized a series of orthogonally linked BODIPY dimers using various linkages, including *meso-meso* (Dim 7 and 8) and β -*meso* (Dim 6) connections (Dim 6). These structural variations led to distinct photophysical behaviors. For instance, both quantum chemical calculations and X-ray crystallography confirmed that the representative β -*meso* Dim 6 adopted a nearly orthogonal geometry ($\sim 90^\circ$ dihedral angle), preserving the intrinsic electronic structure of each BODIPY unit while enabling efficient ISC. Consequently, the orthogonal dimers exhibited substantially quenched fluorescence while markedly enhancing singlet oxygen generation. Dim 6 exhibited a Φ_Δ of 0.51 in dichloromethane, closely matching that of the clinical PS methylene blue (MB, 0.57). Notably, Dim 7 and 8 maintained high fluorescence quantum yields, suggesting their potential as dual-function agents for fluorescence imaging and PDT. They also exhibited notable singlet oxygen quantum yields

(0.46 and 0.21, respectively), although these were lower than that of Dim 6. Subsequent studies confirmed that the enhanced triplet population in these BODIPY dimers originated from SOCT or SBCT mechanisms, with the relative efficiency of each pathway strongly dependent on the specific linkage geometry.^{37,40,61,62} Building on this strategy, they subsequently synthesized two β -*meso*-linked BODIPY trimers (Fig. 8), further validating the design concept.⁶³ Remarkably, both trimers exhibited efficient singlet oxygen generation in dichloromethane, with quantum yields of 0.53 (Tri 2) and 0.55 (Tri 3), rivaling benchmark PSs and demonstrating the scalability of orthogonal dimer-based triplet enhancement. Jiao and Hao *et al.*⁶⁴ also synthesized a series of *meso*- β -linked BODIPY dimers featuring tunable dihedral angles between the two subunits. Dimers 2a and 2c, lacking pyrrolic substituents, exhibited smaller dihedral angles (34° - 39°), which facilitated excitonic coupling and resulted in broadened, red-shifted absorption bands alongside inefficient singlet oxygen



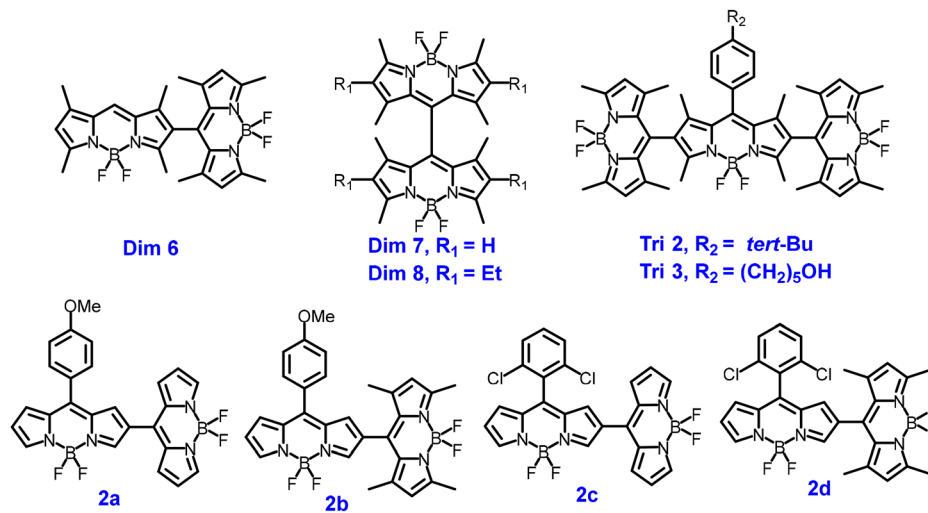


Fig. 8 Chemical structures of β -*meso*- and *meso*-*meso*-linked BODIPY dimers.

generation. In contrast, pyrrolic substitution at the 1,7-positions in 2b and 2d induced nearly orthogonal geometries (84° – 89°), which suppressed excitonic interactions and substantially enhanced ISC efficiency, with dimer 2b exhibiting the highest singlet oxygen quantum yield within the series (Table 2).

Jiao and Hao *et al.*⁶⁵ designed α -*meso*-linked bisBODIPYs (BDP-a and BDP-b) to achieve red-shifted emission while preserving an orthogonal geometry, in contrast to β -*meso* and *meso*-*meso*-linked analogues (Fig. 9). In BDP-a and BDP-b, steric hindrance from the 2-ethyl group imposed an $\sim 84^\circ$ dihedral angle between the BODIPY subunits, effectively restricting rotation and enhancing ISC to the triplet state. Consequently, these orthogonal bisBODIPYs exhibited high singlet oxygen quantum yields ($\Phi_\Delta = 0.62$ – 0.70 in toluene). Meanwhile, BDP-c, BDP-c, which lacks steric constraints, exhibited a lower Φ_Δ of 0.17 owing to diminished orthogonality. The emissions of BDP-a and BDP-b were notably red-shifted (630–671 nm), indicating enhanced electronic coupling without compromising their orthogonal arrangement.

María J. Ortiz and co-workers⁶⁶ advanced BODIPY multi-chromophore engineering by synthesizing fully orthogonal trimers (Tri 4–7, Fig. 9) and systematically elucidating the role of linkage geometry in governing their excited-state behavior. These trimers exhibited monomer-like absorption centered at 505–510 nm, with Tri 7 displaying only a weak long-wavelength shoulder, consistent with the minimal excitonic coupling of its 2-8'/3-8' mixed junctions. Notably, the molar absorption coefficients were highly dependent on linkage geometry: Tri 5, with exclusive 2-8' connections, exhibited a nearly additive value of $2.3 \times 10^5 \text{ M}^{-1} \text{ cm}^{-1}$, while the incorporation of 3-8' linkages substantially diminished absorption efficiency, as observed for Tri 6 ($9.0 \times 10^4 \text{ M}^{-1} \text{ cm}^{-1}$). The 3-8' linkage also stabilized the CT character, resulting in marked fluorescence quenching ($< 0.02\%$ for Tri 6 even in nonpolar solvents) and red-shifted ICT emission, reaching ~ 610 nm for Tri 5 and ~ 675 nm for Tri 4. The trimers collectively underwent SOCT-ISC and efficiently generated singlet oxygen. However, ROS production was reduced in 3-8' linked architectures, particularly Tri 6, where enhanced

Table 2 Photophysical parameters (absorption and emission maxima and fluorescence quantum yields) and ROS generation efficiencies of α -*meso*-, β -*meso*-, and *meso*-*meso*-linked BODIPY dimers and trimers

Molecules	λ_{abs} (nm)	λ_{em} (nm)	Φ_{F}	ROS type	Φ_Δ	Synthetic yield	Ref.
Dim 6	514	527	0.03	$^1\text{O}_2$	0.51	20%	60
Dim 7	515	588	0.31	$^1\text{O}_2$	0.46	16%	
Dim 8	542	605	0.49	$^1\text{O}_2$	0.21	9%	
Tri 2	507/522	—	—	$^1\text{O}_2$	0.53	40%	63
Tri 3	—	—	—	$^1\text{O}_2$	0.55	56%	
BDP-a	514	633	0.03	$^1\text{O}_2, \text{O}_2^{\bullet-}$	0.62	31%	65
BDP-b	516	628	0.07	$^1\text{O}_2, \text{O}_2^{\bullet-}$	0.70	29%	
BDP-c	516	671	0.09	$^1\text{O}_2, \text{O}_2^{\bullet-}$	0.17	78%	
Tri 4	513	545	0.09	$^1\text{O}_2$	0.49	7%	66
Tri 5	513	535	0.23	$^1\text{O}_2$	0.78	51%	
Tri 6	508	617	0.019	$^1\text{O}_2$	0.29	5%	64
Tri 7	505	612	0.179	$^1\text{O}_2$	0.72	32%	
2a	521	563	0.007	$^1\text{O}_2$	—	31%	
2b	507	540	0.002	$^1\text{O}_2$	—	23%	
2c	538	568	0.002	$^1\text{O}_2$	—	33%	
2d	507	542	0.002	$^1\text{O}_2$	—	25%	



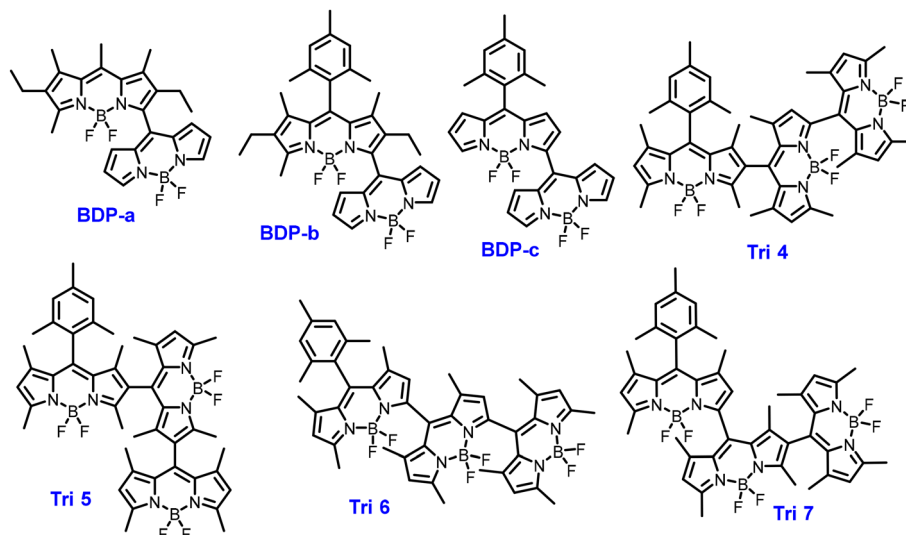


Fig. 9 Chemical structures of α -meso-linked BODIPY dimers and trimers.

CS stabilization facilitated nonradiative decay and concurrently suppressed fluorescence and ISC. Overall, this study underscored linkage-controlled excited-state modulation as a powerful design strategy for optimizing the photophysical performance of heavy-atom-free BODIPY systems.

Notably, the efficient implementation of SBCT is vital for designing high-performance PSS, yet its efficacy is strongly dictated by molecular architecture and the interplay of competing photophysical processes.³⁷ A representative case is the long-wavelength BODIPY dimer 3D, as reported by Winter and co-workers.³⁶ Although 3D undergoes SBCT in polar solvents, forming an intramolecular CT state, its singlet oxygen quantum yield ($\Phi_{\Delta} = 0.5\%$) is notably lower than that of its monomeric counterpart 3M ($\Phi_{\Delta} = 1.4\%$). Detailed analyses revealed that while the ICT state in 3D forms rapidly (~ 1 ps in methanol, ~ 500 fs in dimethylformamide), it does not constitute the sole excited-state decay route; rather, it competes with ISC, fluorescence, and nonradiative relaxation. This competition becomes particularly pronounced in polar solvents, where greater channeling into the ICT pathway diminishes ISC efficiency. These findings underscore the need to carefully balance photophysical decay pathways when engineering symmetric dimers and highlight a critical design consideration for long-wavelength dyes prone to nonradiative losses (Fig. 10).

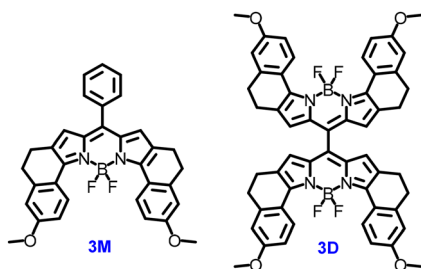


Fig. 10 Chemical structures of 3M and 3D.

Although BODIPY dimerization notably enhances photosensitizing performance, most reported dimers rely on the Type-II mechanism to generate singlet oxygen, which may compromise their efficacy in treating hypoxic tumors. To address this challenge, Yang *et al.*⁶⁷ developed a series of α - β -linked BODIPY dimers and a trimer exclusively producing superoxide radicals ($O_2^{\bullet -}$) via the Type-I mechanism, offering a promising strategy for hypoxia-resistant PDT. Notably, in dimer 1a, the two BODIPY units were joined at the α, β -positions, partially preserving planarity while modulating electronic interactions. Consequently, Dim 9a exhibited red-shifted absorption at 628 nm ($\epsilon = 4.7 \times 10^4 \text{ M}^{-1} \text{ cm}^{-1}$), weak fluorescence at 746 nm ($\Phi_F = 0.8\%$), and a nearly planar configuration with a dihedral angle of 19.7° . Electrochemical analysis revealed an anodic shift promoting electron acceptance, consistent with its ability to generate $O_2^{\bullet -}$. Laser flash photolysis confirmed a prolonged triplet lifetime (1514 μs) and a T_1 energy below the threshold for singlet oxygen generation, validating its exclusive Type-I behavior. Tri 8 further exhibited red-shifted absorption at 740 nm in DMSO ($\epsilon = 6.0 \times 10^4 \text{ M}^{-1} \text{ cm}^{-1}$) while maintaining a long triplet lifetime of 1060 μs . It demonstrated potent phototoxicity toward HepG2 cells under normoxic conditions ($IC_{50} = 0.39 \mu\text{M}$) and retained high activity under hypoxic conditions ($IC_{50} = 0.56 \mu\text{M}$). These findings underscore the potential of α - β -linked BODIPY oligomers as effective Type-I PSS for treating hypoxic tumors (Fig. 11).

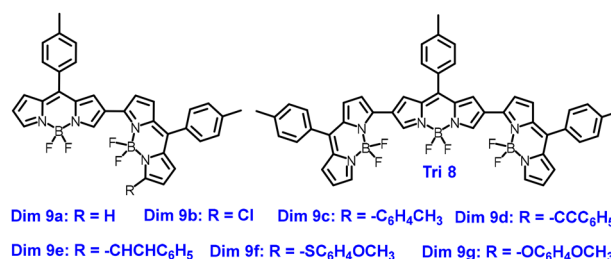


Fig. 11 Chemical structures of α, β -linked BODIPY dimers and trimers.



Collectively, these findings demonstrate that the linkage topology exerts a decisive influence on triplet-state accessibility and ROS generation efficiency. Co-planar dimers (α - α - and β - β -) typically display red-shifted absorption and emission in the NIR region but fail to generate ROS, while orthogonal dimers (*meso-meso*-; β -*meso*-; α -*meso*-; α - β -; and α - γ -) serve as heavy-atom-free PSs capable of producing singlet oxygen. To clarify this structure–function relationship, Fan’s team⁶² conducted theoretical calculations and examined the photodynamic behavior of BODIPY dimers with diverse linkage configurations. By optimizing molecular geometries and examining frontier orbitals, electron density differences, SOC matrices, and excited-state decay rates, they found that β - β - and α - α -linked dimers tend to adopt planar geometries in the T_1 state, suppressing ISC and limiting singlet oxygen generation. In contrast, *meso*- β -, *meso-meso*-, and α - γ -linked dimers preserve dihedral angles of 125° – 143° in the T_1 state, thereby facilitating ISC and enhancing ROS production. Notably, the α - γ -linked dimer exhibited long-wavelength emission originating from $S_1 \rightarrow S_0$ transitions involving lowest-unoccupied-molecular-orbital-to-highest-occupied-molecular-orbital (LUMO \rightarrow HOMO) excitations with moderate oscillator strength, consistent with experimental observations. Additionally, substantial SOC matrix elements further improved ISC efficiency. Notably, in these favorable systems, the $S_1 \rightarrow T_1$ process entails pronounced CT from the 1CT state to 3LE state, indicative of an SOCT-ISC mechanism. Overall, this study underscores the importance of controlling the T_1 -state dihedral angle as a design strategy for enhancing the photosensitivity of BODIPY PSs in therapeutic and imaging contexts.

Despite their promise as a heavy-atom-free strategy for PS design, directly linked BODIPY dimers present inherent limitations. Specifically, their photodynamic performance is highly sensitive to solvent polarity: while high singlet oxygen yields are typically achieved in low-polarity media, efficiency markedly declines in polar environments owing to ultrafast intramolecular charge transfer, which suppresses ISC. This polarity-dependent behavior may compromise their reliability in complex biological environments. Nevertheless, their inherent lipophilicity promotes accumulation in lipid-rich organelles or protein pockets following cellular uptake, potentially mitigating polarity-induced quenching to some extent. Extending absorption into the longer-wavelength region introduces further challenges. As exemplified by dimer 3D, red-shifted systems may exhibit greater competition from non-radiative decay pathways, ultimately diminishing ROS generation efficiency. These findings underscore the importance of co-optimizing linkage geometry, electronic coupling, and spectral characteristics to develop robust, broadly applicable heavy-atom-free PSs.

(3) *BODIPY dimers linked by spacers*. Beyond direct linkage, incorporating a molecular spacer between two BODIPY units has emerged as a widely adopted design strategy. Compared with covalently fused dimers, spacer-linked architectures offer greater structural diversity, enabling precise control over interchromophore distance, orientation, and conformational dynamics. This tunability facilitates systematic exploration of

excited-state dynamics. Moreover, by attenuating excessive electronic coupling while maintaining effective interunit communication, the spacer strategy provides a versatile platform for optimizing triplet formation, ROS yield, and aggregation behavior in molecular dimers.

Yoon and co-workers⁶⁸ recently introduced a RP-ISC strategy to design heavy-atom-free PSs (Fig. 12). In their designed configuration, two BODIPY chromophores were conjugated to a phenoxazine (PXZ) donor, yielding A–D–A-type molecules (BDP-8 and BDP-9). The resulting architectures adopted strongly twisted geometries, with near-perpendicular ($\sim 90^\circ$) torsional angles between the BODIPY and PXZ units, as confirmed by density functional theory (DFT) calculations. This structural distortion ensured well-separated HOMO/LUMO distributions and a remarkably small ΔE_{ST} . Unlike the conventional D–A-type BODIPY (BDP-5), which undergoes SOCT-ISC from the singlet CT state (S_1) to the triplet local excited (LE) state (T_1), the A–D–A systems exhibited multiple ISC pathways. Specifically, the near degeneracy of the S_1/S_2 and T_3/T_4 states facilitated efficient CT from singlet to triplet CT states, consistent with the RP-ISC mechanism. Consequently, the calculated k_{ISC} values of BDP-8 and BDP-9 reached 2.44×10^5 and 2.31×10^5 s^{-1} , respectively, nearly an order of magnitude higher than that of BDP-5 (5.99×10^4 s^{-1}). Importantly, their 1O_2 generation efficiencies were comparable to those of the benchmark 2,6-diiodo-BODIPY PS under identical conditions, demonstrating that RP-ISC is a viable alternative to heavy-atom-based ISC enhancement. To further assess their biomedical applicability, BDP-8 and BDP-9 were formulated into polymer-encapsulated NPs (BDP-8/BDP-9 NPs), which exhibited bright red emission, photostability across physiological pH conditions, efficient ROS production, and pronounced phototoxicity. *In vivo*, BDP-8 NPs achieved $\sim 75\%$ tumor growth inhibition under green LED irradiation, while control groups (light only or PS only) displayed rapid tumor progression. These findings underscore the potential of RP-ISC-based BODIPY derivatives as a next-generation class of heavy-atom-free, biocompatible, and efficient PSs for photodynamic cancer therapy.

Triphenylamine (TPA), characterized by a propeller-shaped geometry, functions as an effective spacer imposing a fixed

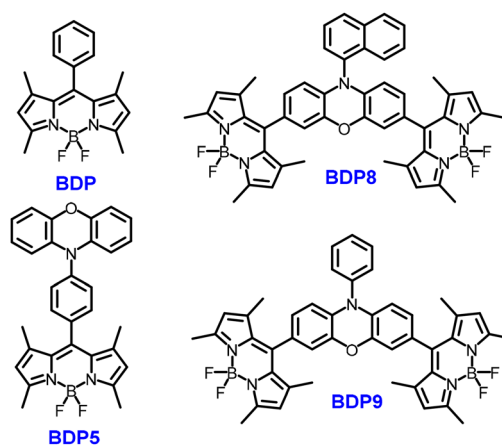


Fig. 12 Structures of phenoxazine-linked BODIPY dimers.



dihedral angle between two chromophores while preserving electronic communication through its π -conjugated framework. Building on this structural advantage, Qian *et al.*⁶⁹ developed a vinyl-pyridine-substituted BODIPY dimer (VP-BDP2), derived from T-BDP2, which exhibited efficient photodynamic activity in pure aqueous systems (Fig. 13). Relative to T-BDP2, VP-BDP2 displayed a considerably higher singlet oxygen quantum yield (increasing from 22.2% to 9.38%), faster CT dynamics (decreasing from ~ 30 ps to ~ 10 ps), and red-shifted emission advantageous for imaging applications. Notably, VP-BDP2 could also generate superoxide radicals ($O_2^{\bullet-}$) in water, thereby expanding its ROS repertoire. Studies confirmed that ROS generation occurs through an SOCT-ISC mechanism. In aqueous media, aggregation-induced emission stabilized the CT state, while vinyl-pyridine substitution minimized energy loss, enhanced charge separation, and facilitated ISC. The triplet energy gap was also reduced ($T_3 \rightarrow T_5$: 0.13 eV for VP-BDP2 *vs.* 0.48 eV for T-BDP2), favoring triplet state and ROS generation.

Advancing their spacer-engineered dimer design, Qian *et al.*⁷⁰ further extended the absorption wavelength of BODIPY systems and developed a heavy-atom-free BODIPY dendrimer PS (TM4-BDP) employing a spin-vibronic coupling (SV-ISC) mechanism to enable efficient one- and two-photon PDT. Notably, TM4-BDP exhibited an intense absorption band at 685 nm ($\epsilon = 1.28 \times 10^5 \text{ M}^{-1} \text{ cm}^{-1}$) and fluorescence emission at 720 nm, accompanied by a weak CT emission tail spanning 750–800 nm. Relative to its analogues, the singlet oxygen yields of TM-BDP, TM2-BDP, and TM4-BDP increased from 0.18% to 4.21% in dichloromethane and reached 11.2% in carbon tetrachloride, underscoring the role of the BODIPY-indole module as the “functional zone” for ISC. EPR analysis demonstrated superoxide radical generation under 660 nm irradiation. Moreover, in CNE-2 cancer cells, TM4-BDP preferentially localized in lysosomes, triggering pronounced

phototoxicity with an IC_{50} of 22.1 μM . Notably, TM4-BDP exhibited a two-photon absorption cross-section of 383 GM at 1030 nm, corresponding to a $\sim 33\%$ enhancement over TM2-BDP. Electronic structure analysis revealed that the ISC process transitioned from conventional SOCT-ISC to SV-ISC, mediated by the out-of-plane vibrational modes ($6.59\text{--}7.34 \text{ cm}^{-1}$) of the indole-BODIPY fragment, which facilitated singlet-triplet state mixing. The near-resonant energy gap between the $S_{1/2}$ (1.83 eV) and $T_{3/4}$ (1.84 eV) states further supported the SV-ISC pathway.

Alkenes represent an attractive class of molecular spacers, as they not only bridge chromophoric units but also partially extend π -conjugation, thereby modulating the electronic coupling between them. Building on this concept, Hao and Jiao *et al.*⁷¹ synthesized a series of BODIPY dimers (Dim 10), trimers (Tri 9), and tetramers (Tera 1) using a “ground-state conjugation, excited-state rotation” design principle (Fig. 14). Extending conjugation *via* ethene linkages led to red-shifted absorption maxima at 700, 864, and 1002 nm, with high molar extinction coefficients ($\epsilon = 2.16 \times 10^5 \text{ M}^{-1} \text{ cm}^{-1}$ at 694 nm for Dim 10; $2.17 \times 10^5 \text{ M}^{-1} \text{ cm}^{-1}$ at 857 nm for Tri 9; $1.38 \times 10^5 \text{ M}^{-1} \text{ cm}^{-1}$ at 992 nm for Tera 1 in CH_2Cl_2), each substantially higher than that of the monomeric analogue ($\epsilon = 6.3 \times 10^4 \text{ M}^{-1} \text{ cm}^{-1}$ at 500 nm). Their emission profiles likewise shifted into the deep-NIR region, with maxima at 716, 890, and 1071 nm in toluene. Notably, oligomeric extension led to a systematic decline in fluorescence quantum yield (93% for the monomer, 40% for the dimer, 0.58% for the trimer, and $<0.01\%$ for the tetramer), indicating progressive suppression of radiative decay in favor of nonradiative processes. The dimer maintained singlet oxygen generation ($\Phi_{\Delta} = 0.12$ in toluene), while the trimer and tetramer exhibited substantially reduced ROS yields but enhanced photothermal performance. Notably, the trimer exhibited a remarkable PCE of 72.4%, attributed to efficient intramolecular rotation in the

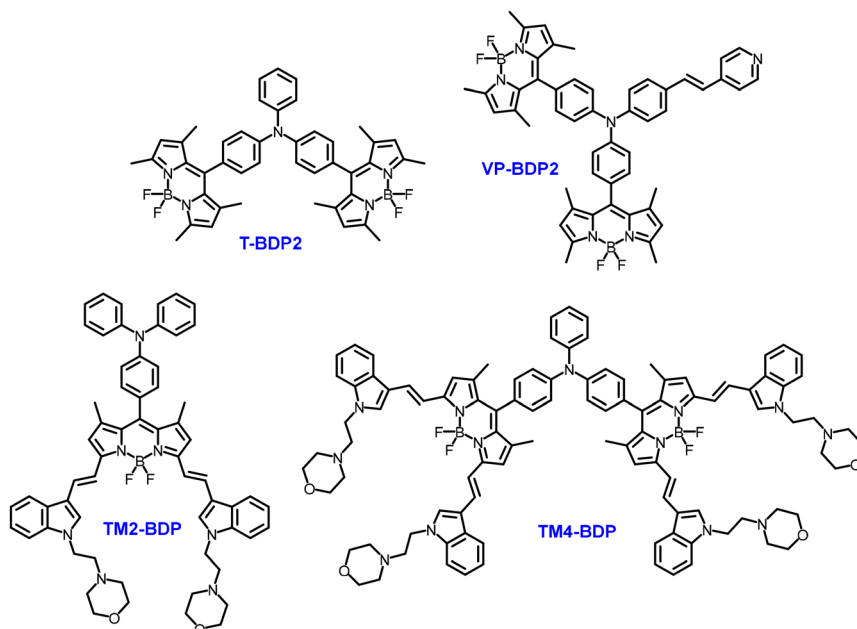


Fig. 13 Molecular structure of BODIPY dimers linked by a triphenylamine spacer.



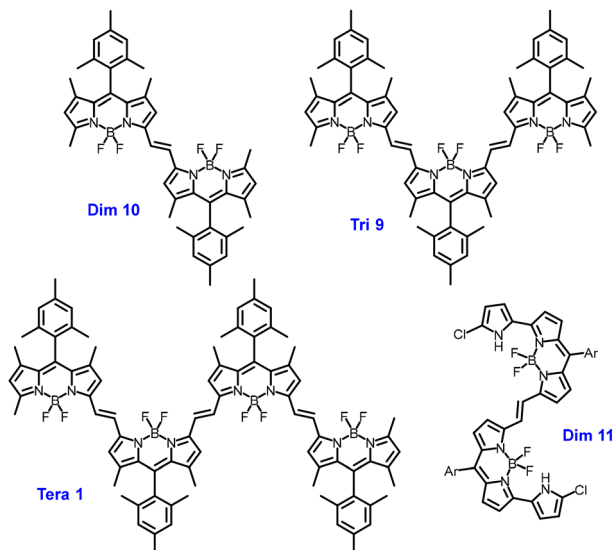


Fig. 14 Structures of ethene-linked BODIPY dimers and trimers.

excited state. This behavior was confirmed by potential-energy surface calculations, which revealed low rotational energy barriers and consistently small E_{gap} values. For biomedical use, the hydrophobic oligomers were encapsulated within a pH-responsive poly(ethylene glycol)-*block*-poly(2-(diisopropylamino)ethyl methacrylate) diblock copolymer, forming NPs featuring a uniform size distribution, excellent photostability, and tumor acidity-triggered release. Among these NPs, trimer NPs (absorption at 857 nm, $\epsilon = 2.17 \times 10^5 \text{ M}^{-1} \text{ cm}^{-1}$, PCE = 72.4%) demonstrated notable tumor photoablation efficacy, achieving complete tumor eradication without recurrence *in vivo* under 808 nm laser irradiation. Subsequently, the authors⁷² synthesized a 3-pyrrolyl BODIPY dimer (Dim 11), which exhibited dual emission peaks at 878 and 983 nm, despite a low fluorescence quantum yield of 0.02 in toluene. DFT calculations revealed stabilized frontier molecular orbitals, with substantial electron density localized over the pyrrole units and ethylene linker, indicating intramolecular CT from the pyrrole moieties to the electron-deficient BODIPY cores. Upon encapsulation within Pluronic F-127 NPs, the dimer exhibited a high PCE of 72.5%, exceeding the value of 46.2% recorded in toluene, along with excellent photo- and thermal stability.

Like alkenes, alkynes are widely employed as spacers in BODIPY dimers. This is because, unlike vinyl linkers, the $\text{C}\equiv\text{C}$ unit provides limited conjugation to the BODIPY core while offering greater rotational freedom, thereby reducing electronic coupling and allowing more flexible excited-state evolution. In a previous study, Zhu *et al.*⁷³ synthesized a symmetrical D-A-D-type BODIPY dimer (P-P) through one-pot oxidative homocoupling (Fig. 15). In this setting, triphenylamine functioned as the donor, BODIPY functioned as the acceptor, and butadiyne functioned as the π -bridge. Acetyl-protected glucose was introduced into both P and P-P to enhance aqueous solubility and facilitate cellular uptake. Compared to P, P-P exhibited broadened and red-shifted absorption (465–725 nm), enhanced

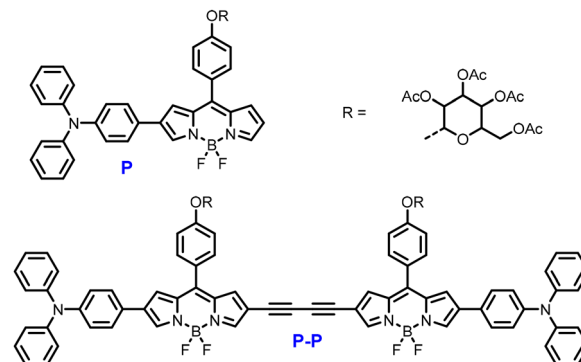


Fig. 15 Structures of alkyne-linked BODIPY dimers.

charge separation, and a prolonged triplet-state lifetime (165 μs vs. 104 μs). Time-dependent DFT (TD-DFT) calculations revealed a reduced ΔE_{ST} for P-P (0.48 eV vs. 1.31 eV for P), attributed to SBCT, which promoted efficient ISC and ROS generation. Further, ROS measurements confirmed the superior activity of P-P. The Φ_{Δ} values of P-P and P-P NPs reached 0.877 and 0.795, respectively, both exceeding that of rose bengal (0.76). P-P also produced substantial amounts of $\text{O}_2^{\bullet-}$. Further, it exhibited strong photothermal conversion, inducing a temperature increase from 28.3 to 43.2 $^{\circ}\text{C}$ at 50 μM under 730 nm irradiation (0.5 W cm^{-2} , 10 min). Biological evaluation revealed excellent dark biocompatibility (>85% cell viability). Upon irradiation, however, P-P NPs exhibited potent phototoxicity, reducing HepG2 cell viability to 19% at 25 μM , with an IC_{50} of 15.2 μM . Although these compounds exhibited promising photophysical properties and dual PDT/PTT functionality, their therapeutic efficacy in cellular assays remained moderate, suggesting that structural refinement or improved delivery is necessary to realize their full biological potential.

Another elegant strategy for constructing BODIPY dimers involves using a single heteroatom as the bridging unit.⁷⁴ Unlike π -conjugated linkers or flexible spacers, heteroatom bridges (*e.g.*, N, S) enforce a compact geometry and impose strong electronic perturbations without considerable structural extension. In a previous study, Jiao' group^{75,76} introduced a novel α -bridged BODIPY dimer design wherein two BODIPY units were connected by a heteroatom (Fig. 16). When using sulfur-bridged oligo-BODIPYs as heavy-atom-free PSs, the lone

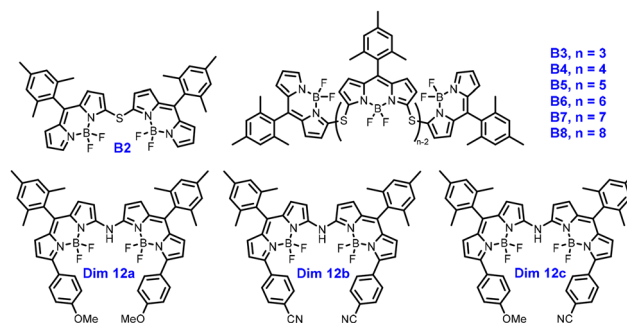


Fig. 16 Molecular structures of heteroatom-bridged BODIPY dimers.



pair on sulfur disrupted extended π -conjugation between the subunits while preserving electronic communication. This fine-tuned both the singlet and triplet excited states, resulting in favorable NIR absorption and efficient singlet oxygen generation through enhanced SOC coupling. Notably, the T_1 energies of B2–B4 (1.37–1.24 eV) rendered them suitable triplet donors, while their calculated SOC values (0.76 – 3.03 cm^{-1}) proved adequate to facilitate ISC. Consequently, B2 and B3 exhibited greater efficiency in generating $^1\text{O}_2$ and $\text{O}_2^{\bullet-}$ than the reference azaBODIPY, indicating the involvement of both energy and electron transfer pathways. The sulfur-bridged strategy was subsequently advanced by replacing sulfur with nitrogen, yielding α - α -nitrogen-bridged BODIPY dimers. In these dimers, the nitrogen bridge facilitated strong excitonic coupling and efficient p-electron delocalization across the two BODIPY cores. This structural configuration produced distinct absorption bands at 518 and 716 nm and a strong NIR emission at 746 nm, indicative of pronounced intramolecular excitonic interactions. The resulting electronic structure supported efficient ISC through exciton-assisted mechanisms. Consistent with these features, the nitrogen-bridged dimer 2a exhibited a moderate ROS quantum yield of 10% in toluene, demonstrating that such exciton-coupled, heavy-atom-free BODIPY dimers can effectively serve as PSs.

Modulating exciton coupling offers a powerful approach for tailoring the photophysical behavior of dyes, although intermolecular interactions are generally more accessible than intramolecular ones. Hao and co-workers⁷⁷ designed vinyl-bridged aza-BODIPY dimers (BDP3 and BDP4) supporting both intra- and intermolecular exciton interactions, thereby enabling efficient tumor PTT (Fig. 17). Relative to their monomeric counterparts, BDP3 and BDP4 exhibited absorption bands red-shifted by approximately 100 nm at 758 and 774 nm in dichloromethane, with BDP3 displaying a marked emission red-shift from 690 to 974 nm, reflecting expanded π -conjugation through the β -ethene bridge. Strikingly, BDP3 displayed Davydov splitting, characterized by two dominant absorption bands at 758 and 582 nm, with the latter blue-shifted relative to the monomer. These spectral signatures indicate enhanced dipole-dipole interactions and strengthened transition dipole moments. Upon self-assembly in water, BDP3 formed J-aggregated NPs (BDP3 NPs), with absorption and emission peaks further red-shifted to 936 and 1003 nm, respectively. This slip-stacked arrangement substantially narrowed the bandgap and conferred ultraphotostability, a high PCE (60.3%), and potent phototoxicity ($\text{IC}_{50} = 7.7$ μM) to the NPs. *In vivo*, BDP3 NPs achieved complete tumor ablation under 915 nm laser irradiation at

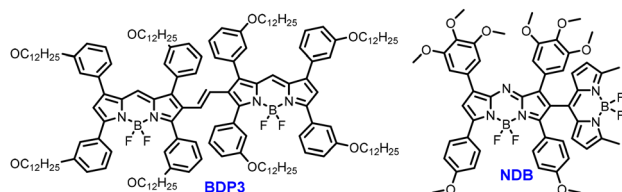


Fig. 17 Structures of aza-BODIPY dimers.

ultralow power density, underscoring their strong potential for NIR-II-guided PTT. Nonetheless, the requirement for precise J-aggregation conditions highlights the need for simplified molecular design strategies to realize effective J-aggregate-based theranostic agents.

Dong *et al.*⁷⁸ developed an orthogonally configured aza-BODIPY–BODIPY dyad (NDB; Fig. 17) to enhance ROS generation through the SOCT-ISC mechanism. The optimized geometry featured a 76° torsion angle between the aza-BODIPY and BODIPY units, thereby accounting for the orthogonal configuration and facilitating efficient ISC. In toluene, NDB exhibited dual absorption bands at 513 nm (BODIPY) and 703 nm (aza-BODIPY), an optical bandgap of 1.65 eV, and an emission maximum at 744 nm with a fluorescence lifetime of 2.8 ns. Upon irradiation at 730 nm, NDB demonstrated a three-fold higher ROS generation efficiency than that of ICG. To improve solubility and biocompatibility, NDB NPs were prepared using DSPE-PEG2000 and PEGylated phenylboronic acid. These NPs exhibited a high PCE (39.1%), notable photostability, and excellent antibacterial efficacy. *In vitro* assays against methicillin-resistant *Staphylococcus aureus* revealed a survival rate of only 8% for NDB NPs under laser irradiation, compared with 75% for NDB NPs alone and 88% for laser exposure alone. Collectively, these results highlight the dual PDT/PTT applicability of NDB NPs, which integrate ROS generation and photothermal effects for effective bacterial eradication, positioning them as a promising halogen-free platform for photo-initiated antibacterial therapy.

(4) *Activatable and targeted BODIPY dimers.* While earlier BODIPY dimers focused on tuning photophysical properties to enhance ROS generation or heat production, a parallel strategy has emerged: the development of activatable or targeted PSs.⁷⁹ This approach seeks to achieve selective tumor ablation while sparing surrounding healthy tissue. These stimuli-responsive BODIPY dimers are designed to remain functionally inert during systemic circulation. Their therapeutic and diagnostic functions are activated only upon the recognition of a tumor-specific biomarker within the tumor microenvironment.

Akkaya and co-workers⁸⁰ developed a GSH-activatable BODIPY dimer for heavy-atom-free PDT. As depicted in Fig. 18, BDP was initially condensed with pyridinecarboxaldehyde, followed by quaternization of the pyridine unit, a modification that increases the susceptibility of the double bond to nucleophilic attack by GSH. Because intracellular GSH levels in normal cells are approximately one-fifth of those in cancer cells, this design enables efficient discrimination between healthy and malignant

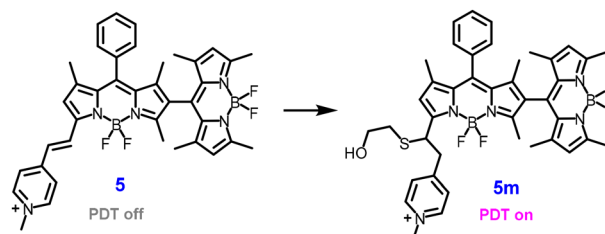


Fig. 18 Structures of glutathione (GSH)-activatable BODIPY dimers.



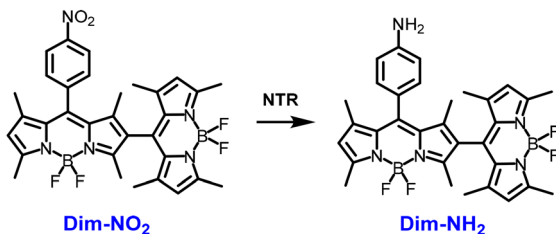


Fig. 19 Structure of a nitroreductase (NTR)-responsive BODIPY dimer.

cells, thereby facilitating selective cytotoxicity in cancer cells. Notably, the above study marked the first demonstration of selective, GSH-triggered intracellular activation enhancing photocytotoxicity in cancer cells (Fig. 19).

Tan *et al.*⁸¹ synthesized a BODIPY dimer (Dim-NO₂) responsive to NTR, designed as a hypoxia-activatable photosensitizer for tumor-selective PDT. A nitro group was introduced at the *meso*-position to quench both fluorescence and singlet oxygen generation in the native state. Upon exposure to NTR, enzymatic reduction of the nitro group reinstated strong fluorescence and PDT efficacy. Further, incubation with 1 mg mL⁻¹ NTR increased the Φ_{Δ} value from 0.05 to 0.46, confirming enzyme-mediated activation and substantial ¹O₂ generation.

Yin *et al.*⁸² developed a lysosome-targeting BODIPY dimer (Dim-Lyso) by incorporating two morpholine groups (Fig. 20), which conferred strong lysosomal affinity and pronounced NIR absorption ($\lambda_{\text{abs}} = 673$ nm) and emission ($\lambda_{\text{em}} = 732$ nm). Under 660 nm laser irradiation, the dimer exhibited efficient ROS generation and photothermal conversion. Upon self-assembly with Pluronic F127, Dim-Lyso formed stable nanomicelles (Dim-Lyso NPs) that enhanced cellular uptake and lysosomal localization. In DMSO, Dim-Lyso generated considerably more singlet oxygen than Dim-Cl. In aqueous media, Dim-Lyso NPs maintained high ¹O₂ generation efficiency, outperforming the clinically approved Ce6. Mechanistically, Dim-Lyso NPs accumulated in lysosomes and, upon irradiation at 660 nm, induced severe lysosomal disruption, thereby concurrently initiating pyroptosis and immunogenic cell death through NLRP3/Gasdermin D (GSDMD) and caspase-3/GSDME signaling. Notably, lysosomal dysfunction also impaired protective autophagy, further enhancing therapeutic efficacy. Consequently, both intratumoral and intravenous administration of BDPd NPs followed by laser irradiation markedly inhibited tumor growth in a triple-negative breast cancer model. Such treatment also

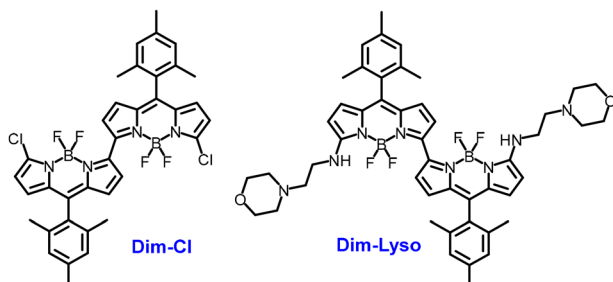


Fig. 20 Structure of a lysosome-targeting BODIPY dimer.

elicited systemic antitumor immune responses, extended survival, and achieved complete tumor eradication in ~60% of intravenously treated mice.

3.2 Cyanine dimers

3.2.1 Dimers based on symmetric polymethine cyanines.

Cyanine derivatives are widely regarded as promising agents for bioimaging and PDT, owing to their excellent biosafety, high molar extinction coefficients in the NIR region, and straightforward synthesis.⁵⁰ However, their clinical translation remains constrained by their inherent drawbacks, including short triplet-state lifetimes and low singlet oxygen quantum yields. To address these limitations, Peng and colleagues⁸³ synthesized a series of dimeric cyanine dyes by linking pentamethine cyanine units with alkyl chains of various lengths (Fig. 21). Notably, spectroscopic analyses revealed pronounced H-aggregate absorption bands in these dimers, with excitonic coupling progressively weakening as the linker length increased, indicative of reduced chromophore interactions. In parallel, the fluorescence quantum yield increased with chain extension, reaching near-monomeric levels with C10 bridging. X-ray crystallography corroborated the presence of H-aggregate packing modes in representative dimers, a structural arrangement that suppressed radiative singlet decay and stabilized triplet states. Consequently, the dimers exhibited extended triplet lifetimes and considerably enhanced singlet oxygen quantum yields (14–20%), which were up to 28-times that of the monomer (0.7%). These improvements translated into superior therapeutic outcomes, as demonstrated by Cy-He-D, which displayed substantial ROS production, minimal dark toxicity (IC₅₀ = 0.92 μ M), and strong mitochondrial localization in 4T1 cells. *In vivo* studies in 4T1 tumor-bearing mice further confirmed that Cy-He-D effectively inhibited tumor growth, underscoring dimerization as a robust strategy for developing heavy-atom-free PSs with improved PDT efficacy (Table 3).

Peng *et al.*⁸⁴ developed a dimeric pentamethine cyanine dye incorporating a fused benzene ring (Cy-D-5) to enable synergistic PTT/PDT (Fig. 22). Relative to its monomeric counterpart

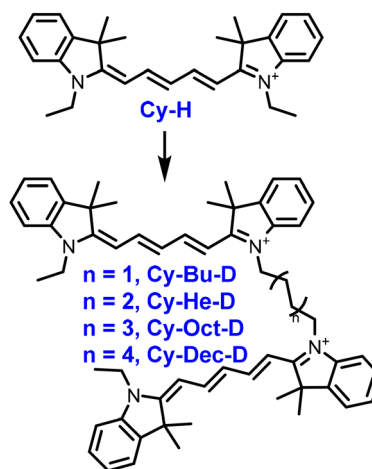


Fig. 21 Chemical structures of pentamethine cyanine dimers bearing alkyl linkers of varying lengths.

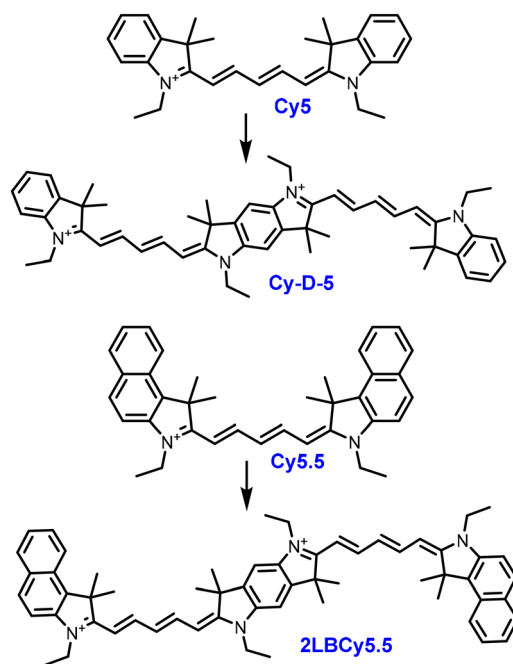


Table 3 Photophysical parameters (absorption/emission maxima and fluorescence quantum yield), ROS generation capacity, and photothermal performance of cyanine monomers and dimers

Molecules	λ_{abs} (nm)	λ_{em} (nm)	Φ_{F}	ROS	Φ_{Δ}	PCE	Synthetic yield	Ref.
Cy-H	640	660	0.15	$^1\text{O}_2$	0.007	—	—	83
Cy-Bu-D	655	672	0.01		~ 0.14		28%	
Cy-He-D	646	670	0.06		0.19		38%	
Cy-Oct-D	644	670	0.106		0.20		0.35%	
Cy-Dec-D	642	670	0.14		~ 0.14		0.34%	
Cy-D-5	778	801	0.009		—	64.4%	60%	84
Cy5.5	692	720	0.33	—	—	—	70.34%	85
2LBCy5.5	802	850	0.06	$^1\text{O}_2, \text{O}_2^{\bullet-}, \bullet\text{OH}$	—	22.3%	40.38%	
2o-Cy	692	730	0.08		0.16	—	40.3%	86
2m-Cy	693	731	0.05		0.18			
2p-Cy	691	731	0.10		0.27			
ICG	780 ± 10	820	—	$^1\text{O}_2$	—	47.2%	—	87
ICG dimer	780 ± 10	—	—	—	—	95.6%	58.2%	
T780T	780	810	—	$^1\text{O}_2$	—	38.5%	40%	88
T780T-TPP	783	826	—		0.05	40.2%	20%	89
T780T-TPP-C12	783	822	—		0.07	35.0%		
HCy dimer	717	798	0.0019		0.023	46.8%	39%	90
mBHCy dimer	747	832	0.0011		0.028	56.8%	34%	
oBHCy dimer	878	1057	0.00074	—	—	49.2%	21%	

Cy5, Cy-D-5 exhibited substantially altered photophysical properties, including a red-shifted absorption maximum at 778 nm in ethanol (comparable to that of ICG) and a molar extinction coefficient of $3.19 \times 10^5 \text{ M}^{-1} \text{ cm}^{-1}$, which is 1.2-fold higher than that of ICG. Despite this, its fluorescence quantum yield declined to 0.9%, while its photostability improved considerably relative to that of ICG. In the fused configuration, dimerization markedly increased the non-radiative decay rate (k_{nr}), which reached a value approximately 12.6 times greater than that of ICG. Cy-D-5 also exhibited an extended triplet-state lifetime, facilitating energy transfer to oxygen and promoting singlet oxygen generation. Remarkably, Cy-D-5 underwent both H- and J-type aggregation in phosphate-buffered saline (PBS), a mode that synergistically enhanced its phototherapeutic efficacy. In PBS, for instance, its singlet oxygen quantum yield was fivefold higher than that of ICG, while its PCE reached 64.4%. Theoretical calculations provided further mechanistic insight: benzene fusion narrowed the bandgap, red-shifted the absorption, expanded the conjugated plane, and increased oscillator strength, thereby raising the extinction coefficient and reducing the singlet-triplet energy gap to promote ISC. Consequently, in 4T1 cells, Cy-D-5 demonstrated potent synergistic PTT/PDT activity ($\text{IC}_{50} = 4.08 \mu\text{M}$, combination index = 0.63).

Further, Fan and colleagues⁸⁵ developed a novel NIR cyanine-based photosensitizer, 2LBCy5.5, by linking two Cy5.5 units through a dual-cationic benzo[1,2-*b*:4,5-*b'*]dipyrrrole bridge, yielding an expanded and distorted D- π -A- π -D framework (Fig. 22). This dimerization strategy imparted substantial photophysical enhancements, notably a 110 nm red shift in the absorption maximum to 802 nm and a substantially higher molar extinction coefficient ($4.2 \times 10^5 \text{ L mol}^{-1} \text{ cm}^{-1}$), surpassing those of Cy5.5 (692 nm, $2.5 \times 10^5 \text{ L mol}^{-1} \text{ cm}^{-1}$) and ICG (795 nm, $3.2 \times 10^5 \text{ L mol}^{-1} \text{ cm}^{-1}$). The optimized electronic structure produced a narrow ΔE_{ST} that accelerated ISC (1.21 ns^{-1}), affording a high triplet-state quantum yield of 26.1% under 808 nm irradiation and enabling strong type-I PDT activity. The PS exhibited

**Fig. 22** Structures of benzene-ring-fused dimeric pentamethine cyanines.

outstanding ROS generation, with the $^1\text{O}_2$ yield enhanced by 10.6–21.1-fold, $\text{O}_2^{\bullet-}$ production elevated by ~ 8.7 -fold, and $\bullet\text{OH}$ generation increased 3.2-fold relative to that in Cy5.5 and ICG. Furthermore, 2LBCy5.5 maintained a favorable PCE of 22.3% and displayed excellent photostability, supporting dual-mode phototherapy *via* simultaneous type-I ROS generation and photothermal effects under single-wavelength NIR excitation.

Cyanine dyes are often limited by inefficient ISC and short triplet-state lifetimes, which constrain their effectiveness in PDT. To address this, Fan and co-workers⁸⁶ recently introduced a dimerization strategy to modulate exciton coupling by linking



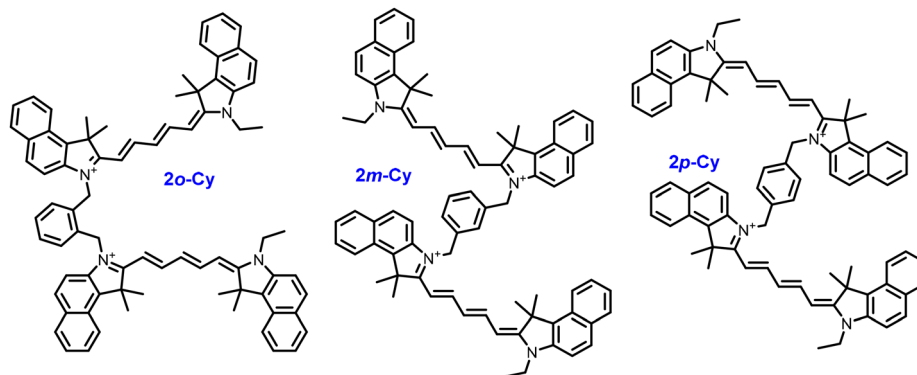


Fig. 23 Structures of pentamethine cyanine dimers incorporating different linkers.

two Cy5.5 molecules at the *N*-indole position using *ortho*-, *meta*-, or *para*-bis(bromomethyl)-benzene linkers (*2o*-Cy, *2m*-Cy, and *2p*-Cy) (Fig. 23). This head-to-tail configuration induced strong dipole–dipole interactions, which split excited-state energy levels and generated delocalized exciton states that promoted efficient ISC. Relative to the Cy5.5 monomer ($\Phi_{\text{ISC}} \approx 11\%$, $\tau_{\text{T}} \approx 4.5 \mu\text{s}$), each dimer exhibited substantially higher triplet quantum yields ($>30\%$) and extended triplet-state lifetimes ($>10 \mu\text{s}$). Among the dimers, *2p*-Cy demonstrated the most pronounced exciton-coupled effect, favoring the $S_1 \rightarrow T_2$ transition through a high SOC constant. This facilitated ultrafast ISC, singlet oxygen yields of up to 26.8%, and substantial ROS generation. In therapeutic evaluations, *2p*-Cy nanoparticles effectively ablated primary tumors and suppressed distant metastases *via* caspase-1/GSDMD-mediated pyroptosis, thereby eliciting a synergistic antitumor immune response. Collectively, these findings underscore exciton coupling in dimeric cyanines as an effective strategy to overcome the intrinsic photophysical limitations of monomeric dyes, offering a rational design framework for developing high-performance, heavy-atom-free PSs in cancer theranostics.

ICG is the only FDA-approved small-molecule fluorophore suitable for clinical imaging and holds substantial potential for surgical navigation and phototherapy. However, its broad clinical application is constrained by its poor photostability and relatively low PCE, rendering structural modification of the

parent scaffold a longstanding research priority. Subsequent studies revealed that one photochemical byproduct of ICG produced under light irradiation is its dimeric form, which has attracted considerable attention. Buzzá and co-workers⁹¹ reported that mixing ICG monomers with glyceryl trioctanoate oil to form a nanoemulsion, followed by storage at 4 °C, induced oxidative dimerization within the core–shell nanostructure, resulting in nearly 100% conversion to the ICG dimer (Fig. 24). More importantly, the resulting dimer underwent spontaneous J-aggregation on the nanoemulsion shell, forming a nanostructured assembly of dimeric ICG (Nano-dICG). Further investigations revealed that Nano-dICG formation was thermodynamically controlled, with dimerization and J-aggregation occurring nearly simultaneously. Relative to monomeric ICG, Nano-dICG exhibited markedly altered optical properties, including a red-shift in the absorption maximum from 780 nm to 894 nm and an increase in the molar extinction coefficient to $4.1 \times 10^5 \text{ M}^{-1}$, more than twice that of ICG ($1.8 \times 10^5 \text{ M}^{-1} \text{ cm}^{-1}$). In parallel, Nano-dICG exhibited nearly complete fluorescence quenching. Collectively, these features conferred exceptionally high PCE and strong photoacoustic signals to Nano-dICG, enabling efficient photoacoustic imaging-guided photothermal ablation of orthotopic breast tumors.

To obtain a stable ICG dimer, Wang's group⁸⁷ leveraged the reactivity of the ICG radical, which readily couples with another dye molecule, followed by deprotonation and electron loss to yield ICG-II. A similar approach enabled the efficient, high-yield

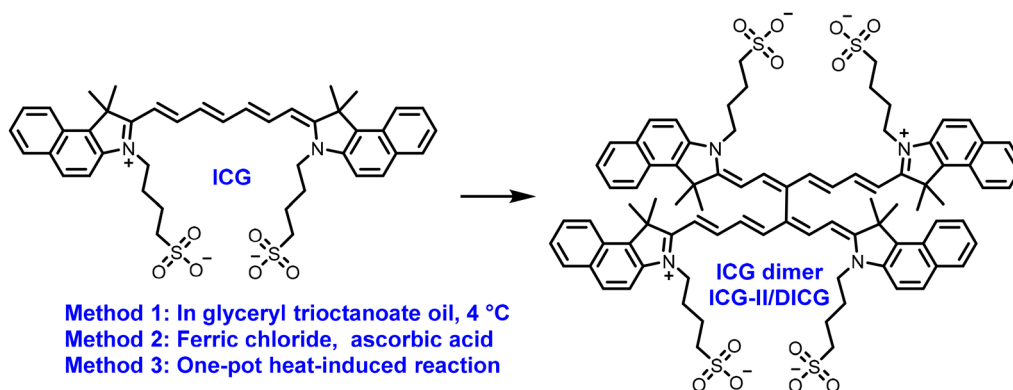


Fig. 24 Strategies for constructing ICG dimers.



synthesis and purification of ICG-II. Notably, ICG-II exhibits photophysical properties distinct from those of monomeric ICG. Although their absorption maxima differ only slightly (785 nm), the dimer exhibits a markedly higher molar extinction coefficient (14.69×10^4 vs. $9.54 \times 10^4 \text{ M}^{-1} \text{ cm}^{-1}$). In contrast, its fluorescence is strongly quenched, and singlet oxygen generation is entirely suppressed. Strikingly, ICG-II achieves a PCE of 95.6%, nearly double that of ICG (47.2%). Theoretical calculations offer mechanistic insights into these distinctive properties. First, TD-DFT analysis reveals two S_0 minima ($\sim 65^\circ$ and $\sim 115^\circ$) separated by a $\sim 1 \text{ kcal mol}^{-1}$ barrier, where steric hindrance from benz-indolyl groups confines motion to a “butterfly” vibration (40° – 140°). This conformational constraint narrows the S_0 – S_1 gap upon excitation, thereby enhancing IC and quenching fluorescence. Second, dimerization alters excited-state alignment: in MICG, the $S_1 \rightarrow T_2$ gap is $\sim 0.24 \text{ eV}$; however, in MICG-II, T_2 lies above S_1 , rendering $S_1 \rightarrow T_1$ ($\sim 0.50 \text{ eV}$) the dominant pathway and thereby suppressing ISC and photodynamic activity. Third, MICG-II exhibits a substantially lower internal reorganization energy (3.0 vs. $12.4 \text{ kcal mol}^{-1}$), which limits structural relaxation and inhibits T_1 formation. Finally, the T_1 state in MICG-II is more extensively delocalized over both monomers than in MICG, imparting greater stability and lower reactivity, thereby favoring photothermal over photodynamic deexcitation. *In vivo* experiments further underscore the therapeutic potential of ICG-II. Specifically, direct intratumoral injection followed by just 2 min of NIR irradiation was sufficient to eradicate xenograft tumors in some mice. Moreover, *ex vivo* analysis revealed that just 1 min of ICG-II irradiation induced greater tumor cell death than 5 min of irradiation with an equivalent ICG dose. Together, these findings highlight the remarkable potential of ICG-II as a photothermal agent and provide new insights for the rational design of high-performance photothermal materials.

Building on the unique properties of ICG dimers, Gu and co-workers⁹² developed an oxygen-nanobubble-loaded ICG dimer (DICG/ O_2 -NBs) platform enabling self-cascading PTT and PDT for hypoxia-reversible tumor treatment. In their study, ICG dimers were synthesized *via* a one-pot, heat-induced reaction (Fig. 24), and subsequent characterization confirmed the formation of the γ - γ -linked dimer rather than the widely assumed *meso*-linked species. Consistent with previous reports, the prepared ICG dimers readily formed J-aggregates in aqueous solutions, resulting in a red-shifted absorption peak at 895 nm. The dimers were subsequently incorporated into oxygen nanobubbles to yield DICG(J)/ O_2 -NBs, which exhibited a high dissolved oxygen content of 30.69 mg L^{-1} , thereby directly addressing tumor hypoxia. Notably, this J-aggregated dimer system exhibited behavior distinct from that in prior reports: upon light irradiation, the J-aggregates disassembled into monomeric DICG (DICG(M)), thereby establishing the basis for cascaded photothermal and photodynamic processes. The PCE values of DICG(J)/ O_2 -NBs and DICG(J) were calculated to be 51.45% and 51.34%, respectively. The localized heating induced by PTT not only detonated the nanobubbles to release O_2 but also facilitated the transition from DICG(J) to DICG(M) while simultaneously generating abundant

$\cdot\text{OH}$ radicals. Moreover, DICG(M) further reacted with the liberated O_2 to produce 1O_2 for type-II PDT. The 1O_2 quantum yields of DICG(J), DICG(M), DICG(J)/ O_2 -NBs, and DICG(M)/ O_2 -NBs were determined to be 0.23%, 0.88%, 0.06%, and 3.37%, respectively. Notably, DICG(M)/ O_2 -NBs achieved the highest 1O_2 yield, approximately 17-fold greater than that of free ICG (0.20%). Through the synergistic combination of PTT with cascaded type-I and type-II PDT, DICG/ O_2 -NBs exhibited strong antitumor efficacy, achieving a tumor growth inhibition rate of 94.26% together with pronounced hypoxia-reversible therapeutic capability *in vivo*.

Controlling the aggregation behavior of organic dyes remains challenging, primarily owing to complex intermolecular interactions and steric hindrance. Song and colleagues⁹³ addressed this limitation by designing Pt-coordinated cyanine dimers, CyR–Pt (R = Me, Et), which spontaneously assembled in aqueous solutions (Fig. 25). Notably, the bulkier ethyl-substituted CyEt–Pt formed loose, amorphous aggregates ($>15 \text{ nm}$), in contrast to the smaller methyl-substituted CyMe–Pt, which assembled into compact J-aggregates ($<3 \text{ nm}$), driven by a subtle “butterfly effect” arising from reduced steric hindrance. This minor structural variation markedly influenced the photophysical properties: CyMe–Pt J-aggregates exhibited a pronounced red-shifted absorption (900–1100 nm), enhanced nonradiative decay, quenched fluorescence, and improved PCE (37% vs. 20% for CyEt–Pt). These J-aggregates demonstrated exceptional stability, forming even at $0.1 \mu\text{M}$, indicative of strong intermolecular interactions. Steric modulation further enabled CyMe–Pt aggregates to suppress ROS generation and enhance photostability. *In vitro* and *in vivo* experiments confirmed that CyMe–Pt nanostructures mediated effective tumor ablation under 980 nm laser irradiation at a safe power, underscoring the value of steric-hindrance-directed aggregation in optimizing both the photophysical behavior and therapeutic efficacy of NIR cyanine dyes.

IR780 was the first NIR dye reported to possess inherent tumor-targeting ability, facilitated by the glycolysis- and hypoxia-induced expression of HIF-1 α and organic anion transporting polypeptides (OATPs), and remained unaffected by ATP-binding cassette transporter-mediated efflux. This enables its selective accumulation in cancer cells, with a strong preference for mitochondrial localization. However, similar to other tricarbocyanines, IR780 exhibits pronounced photobleaching and a limited photothermal conversion efficiency (≈ 3 – 20%). To address these drawbacks, Meng and co-workers⁸⁸ initially substituted the chlorine atom in IR780 with a TPE unit, which was

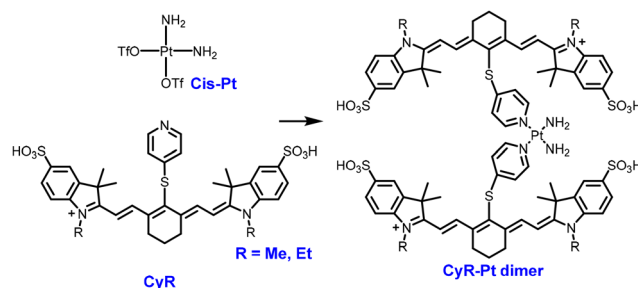


Fig. 25 Structures of Pt-directed cyanine dimers.



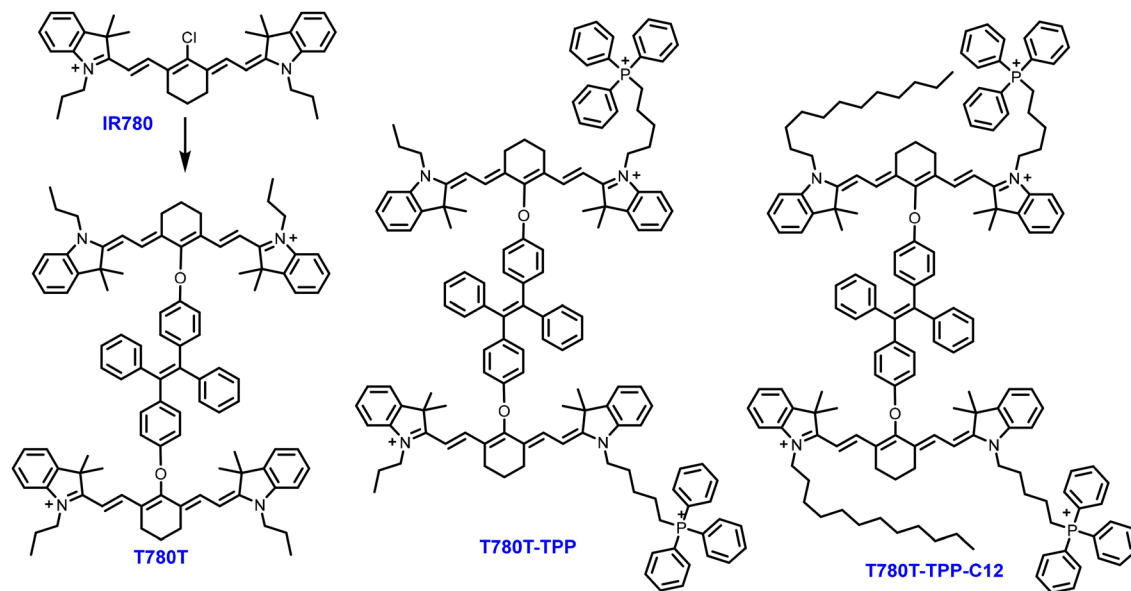


Fig. 26 Structures of TPE-linked cyanine dimers.

subsequently employed as a linker to couple two IR780 molecules into a dimer (T780T, Fig. 26). This twisted conformation promoted excited-state intramolecular motion and suppressed π - π stacking, resulting in reduced molecular packing density. T780T nanoaggregates (~ 200 nm) exhibited enhanced tumor accumulation *via* the EPR effect, with a markedly higher PCE of 38.5%. Efficient OATP-mediated uptake and mitochondrial enrichment contributed to potent anticancer activity *in vitro* and *in vivo*. Notably, although a dimeric structure was constructed, the study primarily focused on TPE's role in enhancing photothermal performance, leaving the specific influence of dimerization on photophysical behavior largely unexplored.

In 2024, the same group⁸⁹ advanced this approach by incorporating triphenylphosphine (TPP) to facilitate mitochondrial targeting while simultaneously introducing steric shielding and electronic deactivation. This yielded four derivatives: IR780-TPP, IR780-TPP-C12, T780T-TPP, and T780T-TPP-C12 (Fig. 26). Although long alkyl chains (C12) were expected to improve photostability, experimental results revealed a counterintuitive reduction in stability relative to shorter chains, though still outperforming monomers. These observations suggest that steric hindrance alone does not fully account for the stabilization effect, with dimerization likely playing the dominant role. Supporting this conclusion, the dimeric analogues achieved considerably higher PCEs, specifically, 40.18% for T780T-TPP and 34.95% for T780T-TPP-C12, compared to their monomeric counterparts (29.50% and 20.54%). Dimerization also enhanced ROS generation. These dyes preserved efficient OATP-mediated uptake and mitochondrial localization, resulting in severe mitochondrial damage and induction of both apoptosis and pyroptosis. In murine tumor models, they demonstrated strong therapeutic efficacy.

Helicobacter pylori (*H. pylori*), which infects over half of the global population, represents a severe threat to human health,

with biofilm formation serving as a key contributor to its antibiotic resistance. Phototherapy presents a promising non-antibiotic strategy to circumvent its resistance development. In 2023, Meng *et al.*⁹⁴ extended their IR780 dimer (T780T) system to antibacterial therapy by incorporating positively charged Gu groups, yielding T780T-Gu (Fig. 27). This modification enhanced water solubility and facilitated electrostatic interaction with the negatively charged bacterial surface, thereby improving biofilm penetration and enabling selective bacterial targeting. Dimerization further increased the photothermal conversion efficiency ($\eta = 46.6\%$) and ROS generation, allowing T780T-Gu to rapidly bind *H. pylori* and induce bacterial death through synergistic photothermal and photodynamic mechanisms. Importantly, Gu conjugation reduced nonspecific uptake by mammalian cells, resulting in negligible dark and light toxicity and thereby ensuring antibacterial selectivity. RNA-seq analysis revealed upregulation of genes encoding heat shock proteins (*grpE*, *groES*, *hrcA*) and outer membrane proteins (*omp6*, *omp27*, *HP0487*), confirming heat stress and membrane disruption. Concurrently, genes associated with translation and ribosomal function were downregulated, indicating impaired bacterial metabolism following phototherapy. Overall, this study underscores how molecular dimerization, coupled with rational surface-charge engineering, can enable potent, selective, and resistance-free eradication of *H. pylori*, offering a compelling alternative to conventional antibiotics.

Cyanine dyes are widely employed in imaging and phototherapy; however, their susceptibility to ROS-mediated oxidative cleavage undermines stability during treatment. When configured as dimers, intrinsic self-quenching between closely spaced cyanine units suppresses fluorescence in the intact state; however, oxidative cleavage of one chromophore reactivates fluorescence from the intact chromophore, converting this vulnerability into a sensing advantage. Building on this concept, Yang *et al.*⁹⁵ developed the first V-shaped asymmetric



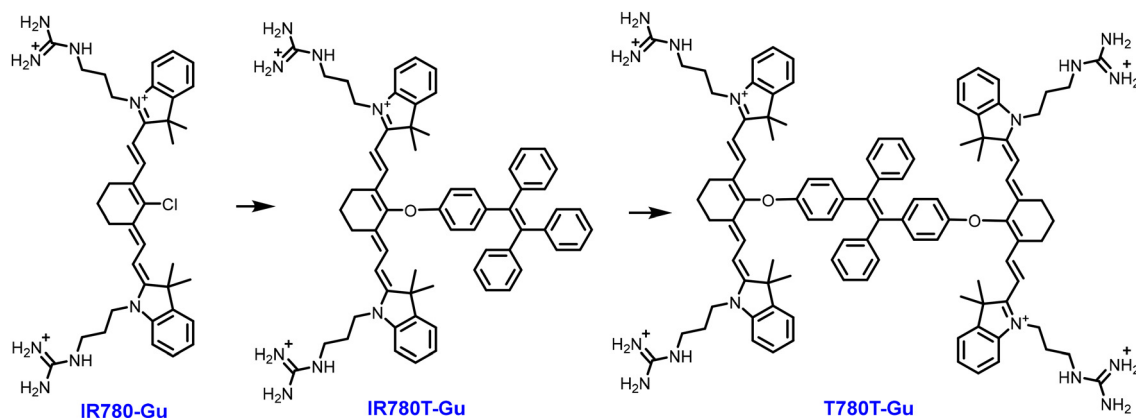


Fig. 27 Structures of guanidinium (Gu)-modified cyanine dimers.

cyanine dimer (VAD1080), a short-wave infrared turn-on fluorescent probe for sensing oxidative stress (Fig. 28). Notably, rational structural design produced a rigid dimeric architecture facilitating ultrafast intramolecular SBCT, effectively quenching fluorescence in the native state. Notably, exposure to highly reactive oxygen species, including ONOO^- , ClO^- , and HO^\bullet , induced selective cleavage of the cyanine backbone, disrupting the SBCT pathway and restoring near-infrared emission with a 61-fold enhancement in fluorescence. Detailed spectroscopic analysis elucidated the photophysical implications of this dimerization strategy. The monomeric IR1080 reference displayed characteristic absorption at 1030 nm and emission at 1068 nm, with a quantum yield of 1.2%. In contrast, the VAD1080 dimer exhibited a modified absorption profile centered at 1020 nm and markedly quenched fluorescence, yielding a quantum yield of just 0.08%. This pronounced quenching effect was mechanistically corroborated by transient absorption spectroscopy, which revealed ultrafast decay of the excited state into a non-emissive SBCT state within 0.6 ps. The probe exhibited remarkable selectivity in its reactivity profile, undergoing strong activation in the presence of highly reactive oxidants while remaining inert toward weaker oxidants and biological thiols. This selective activation pathway was further confirmed *via in vivo* imaging, wherein VAD1080 enabled real-time monitoring of oxidative stress dynamics. A rapid fluorescence increase was observed in the vasculature within 1 h of

acetaminophen overdose, a response notably attenuated by *N*-acetylcysteine (NAC) pretreatment, thereby establishing the probe's suitability for tracking pathological processes in living systems.

Despite recent progress, the development of NIR triplet dyes remains difficult owing to the exponential decline in ISC efficiency at longer wavelengths. Although conventional H- or J-aggregates modestly enhance ISC relative to monomeric dyes, their triplet quantum yields remain inherently low. To address this, Chen and Yang⁹⁶ introduced a strategy using obliquely packed chromophores linked by a spiro-conjugated bridge to yield the novel heptamethine cyanine dimer SZ780 (Fig. 28). The finely tuned V-shaped architecture enforced an uncommon oblique packing arrangement, thereby suppressing non-radiative relaxation pathways and enabling multi-channel ISC processes. Spectroscopic analysis confirmed that SZ780 achieved a record-breaking ISC rate constant of $\sim 10^{11} \text{ s}^{-1}$, the highest reported for NIR triplet dyes, along with a notable triplet quantum yield of 18.9% under 750 nm excitation. Notably, this performance represents a nearly three-fold enhancement over the H-aggregated dimer SC780 (6.7%) and an order-of-magnitude improvement relative to the monomeric IR780 (2.1%). Crucially, these enhanced photophysical properties enable exceptional singlet oxygen generation, with SZ780 achieving a quantum yield of 13.8% under 808 nm irradiation. This value represents nearly a 20-fold increase over the clinical reference ICG, underscoring its considerable

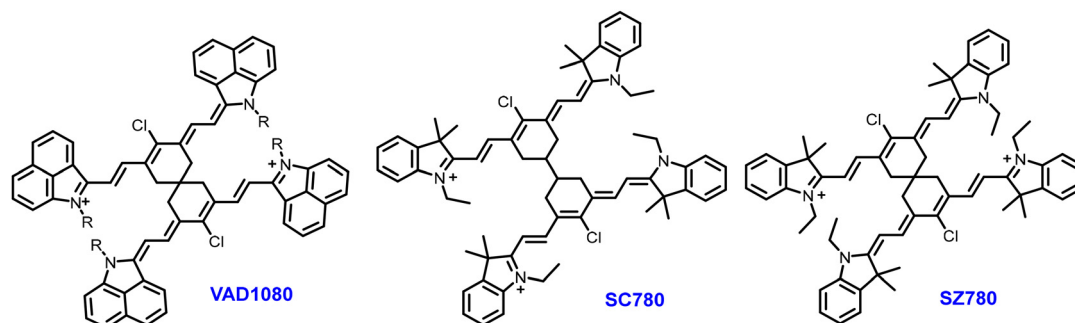


Fig. 28 Structures of cyanine dimers with different linkers.



potential as a PDT agent. Transient absorption spectroscopy directly captured the ultrafast exciton dynamics, confirming that the oblique packing geometry facilitated rapid ISC while suppressing energy trapping in excimer states, a common limitation in conventional H-aggregates. The dye exhibited effective photodynamic destruction of cancer cells with minimal dark toxicity. Collectively, this study established oblique packing *via* spiro-conjugation as a powerful molecular design paradigm, opening new avenues for the development of high-performance NIR triplet sensitizers for biomedical applications.

NIR-II fluorophores and probes offer considerable potential for high-resolution biomedical imaging; however, most of them rely on large π -conjugated planar scaffolds that inherently exhibit several limitations. First, strong π - π stacking interactions in aqueous media lead to aggregation, poor water solubility, blue-shifted absorption, and fluorescence quenching. Second, their extended conjugation makes them susceptible to oxidative and reductive degradation, thereby compromising chemical stability. Third, their hydrophobic nature often causes nonspecific protein binding and large particle formation. Although cyanine dyes such as Cy7 can emit in the NIR-II region, they still suffer from poor water solubility and limited stability.

To overcome these intrinsic limitations, Wu and co-workers⁹⁷ introduced a structural strategy termed the “homo-dyad with outer hydration layer” approach (Fig. 29). Two heptamethine cyanines were linked *via* a flexible spacer, increasing steric hindrance to suppress π - π stacking and enhancing chemical stability, photostability, and spectral stability. Furthermore, four PEG9 chains attached at each terminus formed a hydration shell that markedly enhanced water solubility. More than 10 g of dye dissolved in 1 g of water at 20 °C, while spectral features were preserved and aggregation was avoided. The incorporation of biomarker-responsive units at the *meso*-positions led to the development of HD-FL-4PEG9-N, an NO-activatable probe featuring a rapid response (<10 min),

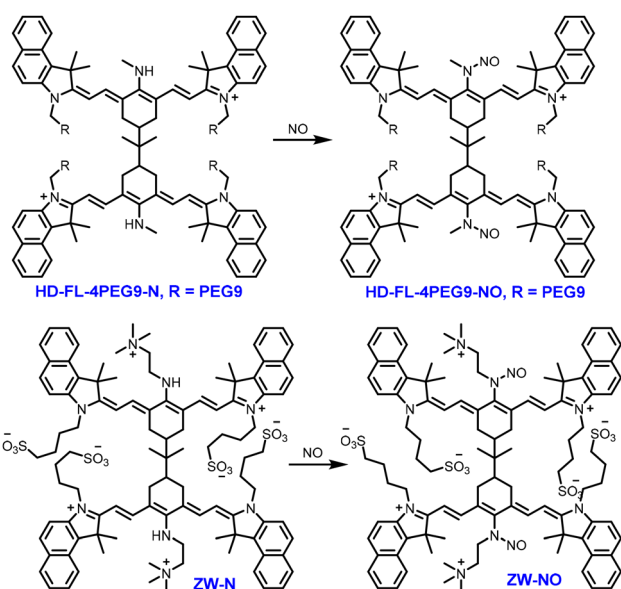


Fig. 29 Structures of NO-activated cyanine dimers.

high sensitivity (detection limit: 0.21 μ M), and dual NIR-II fluorescence/optoacoustic readouts. This probe was successfully applied to monitor drug-induced acute kidney injury and bacterial wound infections, demonstrating the clinical potential of this design strategy.

Building on the optimized homo-dyad scaffold, Wu and coworkers⁹⁸ further developed a zwitterionic chromophore (ZW-N), designed as both a biomarker-activatable probe and a therapeutic agent for lipopolysaccharide-induced acute lung injury (ALI) associated with bacterial infection (Fig. 29). In this system, ZW-N linked two heptamethine cyanines *via* a flexible propanyl spacer and incorporated multiple sulfonate-based zwitterionic groups to confer high aqueous solubility, along with quaternary ammonium moieties imparting antimicrobial activity. To enable NO-responsive imaging, two secondary amines were introduced into the scaffold, allowing ZW-N to detect inflammatory NO through both NIR-II fluorescence and optoacoustic modalities. Notably, ZW-N exhibited potent bactericidal activity at concentrations $\geq 6 \mu$ M and, when co-administered with the clinically approved antioxidant NAC, substantially mitigated ALI progression *in vivo*. Although amine-NO adducts are typically photolabile and susceptible to NO release, Wu and colleagues consistently demonstrated the exceptional stability of the ZW-N-NO adduct, thereby ensuring reliable biomarker detection. This atypical stability not only enhanced the translational promise of ZW-N but also challenged prevailing assumptions regarding the fragility of such adducts, paving the way for the development of robust NO-responsive imaging therapeutics.

Li's group⁹⁰ developed a series of cyanine dye dimers as efficient photothermal agents by linking two cyanine chromophores using hydroquinone moieties. Among these systems, the dimeric oBHCy exhibited notable photothermal performance, achieving a high PCE of 49.2% under 808 nm laser irradiation, together with intense NIR-II fluorescence emission centered at 1057 nm and excellent photostability. Structural analysis indicated that the dimeric configuration induced highly twisted geometries, with dihedral angles of 66.93°, 74.88°, and 80.20° for the respective dimers, while still maintaining delocalized frontier molecular orbitals. Notably, the exceptionally low T_1 energy level of dimeric oBHCy (0.593 eV) was below the oxygen sensitization threshold (0.98 eV), which effectively suppressed ISC and ROS generation. This electronic feature promoted nonradiative decay through intensified intramolecular motion and extended π -conjugation, thereby rendering the system particularly suitable for photothermal applications while minimizing photodynamic activity (Fig. 30).

3.2.2 Dimers based on hemicyanines. In addition to symmetric polymethine cyanines, asymmetric architectures, particularly hemicyanines, have emerged as versatile scaffolds for dimer design.⁹⁹ Unlike classical cyanines, hemicyanines possess a D- π -A electronic configuration, imparting enhanced electronic polarization and expanded structural tunability. Huang *et al.*¹⁰⁰ integrated hemicyanine with bipyridine to construct three variably substituted hemicyanine-bipyridine dimers (Fig. 31), thereby red-shifting bipyridine absorption into the visible region. For instance, bpyCN ($\epsilon_{373\text{nm}} = 6.3 \times 10^4 \text{ M}^{-1} \text{ cm}^{-1}$), bpySN



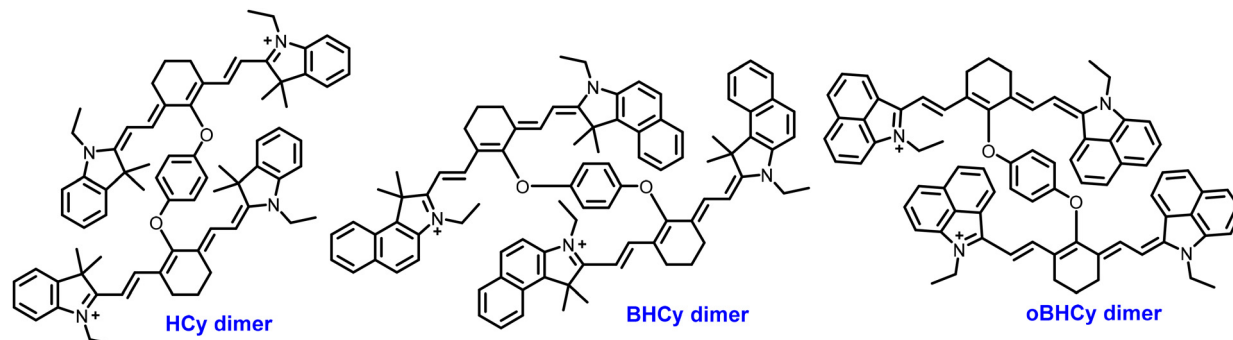


Fig. 30 Representative cyanine dimers for PTT.

($\epsilon_{358\text{nm}} = 4.8 \times 10^4 \text{ M}^{-1} \text{ cm}^{-1}$), and bpyPCN ($\epsilon_{306\text{nm}} = 5.0 \times 10^4 \text{ M}^{-1} \text{ cm}^{-1}$) all exhibited substantially higher extinction coefficients than unsubstituted bpy ($\epsilon_{280\text{nm}} = 1.7 \times 10^4 \text{ M}^{-1} \text{ cm}^{-1}$). Among the three, bpyPCN demonstrated superior photodynamic performance, showing the highest Φ_{Δ} (0.10 in aqueous solutions) alongside robust photocatalytic activity in nicotinamide adenine dinucleotide (NAD)H oxidation (turnover frequency, TOF = 10.1 h^{-1}). In the presence of NADH as an electron mediator, oxygen was converted into $\text{O}_2^{\bullet-}$ and also facilitated the generation of H_2O_2 , thereby enabling concurrent type-I and type-II photodynamic pathways. Furthermore, the high lipophilicity ($\log P$) of

bpyPCN promoted its accumulation in both mitochondria and lysosomes, where light irradiation triggered ROS generation and NADH photo-oxidation, ultimately resulting in potent cancer cell cytotoxicity ($\text{IC}_{50} = 11.8 \mu\text{M}$ against HeLa cells).

Zhou and colleagues¹⁰¹ designed a series of two-photon-excitable superoxide radical generators based on coumarin-pyridinium conjugates linked by alkyl chains of varying lengths (EBD, Fig. 31). Among these structures, the PSs exhibited an inverse correlation between alkyl chain length and therapeutic efficacy: EBD-1, with the shortest chain, showed the highest $\text{O}_2^{\bullet-}$ generation efficiency, whereas EBD-5, with the longest,

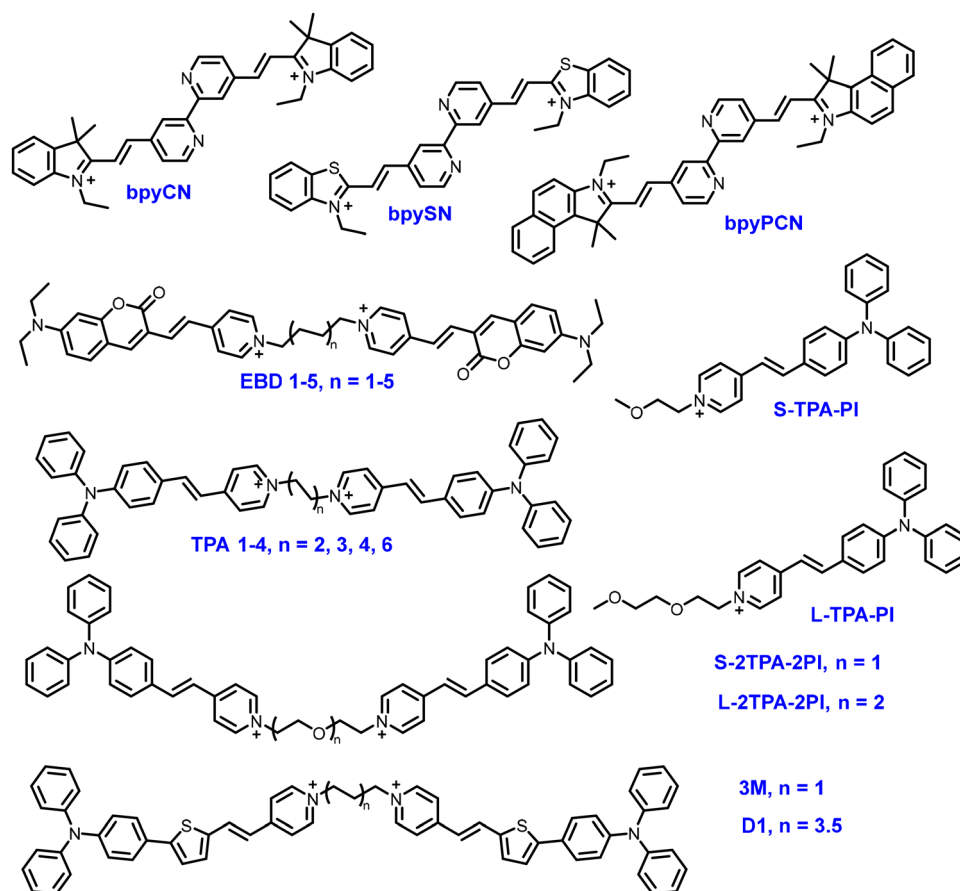


Fig. 31 Asymmetric D- π -A cyanine dimers.



displayed the lowest. This trend was attributed to simultaneous increases in fluorescence quantum yield and intramolecular vibration in the longer-chain derivatives. Remarkably, for EBD-1, real-time monitoring revealed intracellular redistribution of red fluorescence from the plasma membrane to the nucleus, enabling direct visualization of ROS-induced cell death and establishing a self-reporting platform for therapeutic efficacy assessment.

Zhou's team¹⁰² developed a series of bilateral D- π -A AIEgen-based theranostic agents (TPA1-4) by systematically investigating how alkyl chain length influences molecular properties, thereby demonstrating the advantages of the dimerization strategy in optimizing phototheranostic performance (Fig. 31). All compounds exhibited characteristic aggregation-induced emission behavior, with weak fluorescence in ethanol (1.03–1.76%) that was markedly enhanced in an ethanol/cyclohexane mixture (90% cyclohexane), yielding quantum efficiencies of 6.69–17.45%. Among the synthesized compounds, TPA3 exhibited the highest ROS yield, attributed primarily to its smallest ΔE_{ST} . Furthermore, TPA3 showed strong specificity for autophagy vacuoles, enabling real-time monitoring of mitophagy during early apoptosis and inducing pronounced photocytotoxicity in skin cancer models in nude mice. For the first time, the researchers visualized the dynamic autophagy process, including mitochondria, autophagy vacuoles, and lysosomes, in real time using confocal microscopy, thereby establishing a self-monitoring platform for therapeutic assessment.

In subsequent research, Zhou's group¹⁰³ replaced alkyl linkers with hydrophilic glycol chains to develop a next-generation dimeric system (Fig. 31). Systematic photophysical analysis revealed that the incorporation of glycol chains enhanced water solubility and biocompatibility while optimizing excited-state energy allocation by modulating intramolecular motion and electronic coupling. Comparative analysis of monomers (S-TPA-PI/L-TPA-PI) and dimers (S-2TPA-2PI/L-2TPA-2PI) demonstrated the substantial influence of molecular dimerization on photophysical behavior. The dimeric S-2TPA-2PI exhibited a >20-fold increase in ROS generation efficiency despite a lower fluorescence quantum yield (1.85% vs. 14.27% for the monomer), indicating the activation of non-radiative decay channels.

Structural analysis showed that while monomers formed J-aggregates with π - π distances of ~ 3.69 Å, dimers adopted an end-to-end stacking pattern with shorter π - π contacts (~ 3.29 – 3.34 Å) and distinctly different dihedral angles ($41.44^\circ/10.23^\circ$ vs. $15.03^\circ/25.55^\circ$ in the monomer). Mechanistic studies revealed that dimer aggregates exhibited a ~ 500 -fold increase in exciton lifetime and an enhanced ISC rate constant, supported by a reduced S_1 - T_1 energy gap (0.386 eV vs. 0.487 eV in J-aggregates and 0.925 eV in the isolated state) and stronger SOC (0.25 cm⁻¹ vs. 0.14 cm⁻¹ in J-aggregates). Host-guest studies with CB[8] confirmed stacking-dependent ROS generation, while low-temperature phosphorescence (720 nm emission, 2.69 ms lifetime) provided direct evidence of efficient triplet formation in dimers, collectively validating molecular dimerization as a potent strategy for enhancing photodynamic therapy (Table 4).

Expanding on the D- π -A framework composed of triphenylamine and pyridinium groups, Li and colleagues¹⁰⁵ designed a new dimer incorporating thiophene units as stronger electron donors and molecular bridges (Fig. 31). This modification notably enhanced D-A interactions and reduced the S_1 - T_1 energy gap, leading to a spectral red shift and improved ROS generation efficiency. Theoretical calculations revealed highly favorable energy alignments in dimer D1, with a $\Delta E_{S_1T_4}$ of only 0.0001 eV and $\Delta E_{S_1T_1}$ of 0.6716 eV, markedly more favorable than those of monomer M1, thereby considerably enhancing ISC efficiency. The dimeric configuration also facilitated non-radiative transitions by enabling intramolecular stretching vibrations and rotations owing to increased spatial separation between donor and acceptor units. This molecular design yielded notable therapeutic efficacy: D1 generated a high ¹O₂ quantum yield of 89.4% and also efficiently produced type-I ROS species. The membrane-targeted, AIE-active dimer exhibited precise subcellular localization and strong self-assembly ability, enabling pyroptosis-mediated photodynamic/photothermal immunotherapy *via* its pronounced intramolecular CT character and near-infrared AIE properties, marking a notable improvement over traditional monomer-based PS in comprehensive cancer photoimmunotherapy.

As a further refinement of their molecular design, Li's team¹⁰⁴ systematically reduced the alkyl chain length from

Table 4 Photophysical properties (absorption/emission maxima and fluorescence quantum yield) and ROS generation capabilities of various asymmetric D- π -A cyanine dimers

Molecules	λ_{abs} (nm)	λ_{em} (nm)	Φ_F	ROS	Φ_Δ	Synthetic yield	Ref.
bpyPCN	435	600	0.1	¹ O ₂ , O ₂ ^{•-}	0.1	65%	100
EBD1	489	633	0.01	¹ O ₂ , O ₂ ^{•-}	0.90	93%	101
EBD2	486	630	0.09		0.76	88%	
EBD3	485	628	0.17		0.78	85.1%	
EBD4	485	627	0.20		0.83	83.2%	
EBD5	483	626	0.26		0.56	78.4%	
TPA1	468	601	0.016	¹ O ₂	—	70.2%	102
TPA2	469	608	0.013			68.6%	
TPA3	470	601	0.01			65.9%	
TPA4	471	607	0.018			65.1%	
S-TPA-PI	450	744	0.14	¹ O ₂ , O ₂ ^{•-}	—	63.2%	103
S-2TPA-2PI	450	744	0.018	¹ O ₂ , O ₂ ^{•-}		50.7%	
3M	487	679	—			56.3%	104
D1	497	675	—	¹ O ₂ , O ₂ ^{•-} , •OH	0.89	61.4%	105



eight (8M) to three (3M) carbon atoms, uncovering marked enhancements in photophysical performance. Computational analysis revealed that although both molecules exhibited similar electron density distributions, with the LUMO primarily localized on the pyridinium unit and the HOMO localized on the terminal triphenylamine group, the shorter-chain derivative 3M displayed superior characteristics for photodynamic applications. Notably, 3M possessed a reduced ΔE_{ST} (0.6640 eV) compared to 8M, facilitating more efficient ISC. It also exhibited a substantially larger dipole moment (14.5583 D vs. 0.0394 D for 8M), promoting more effective charge separation. Under irradiation, this optimized molecular framework enabled 3M to simultaneously produce type-I and type-II ROS and a photothermal effect, collectively inducing mitochondrial dysfunction and triggering pyroptotic cell death. Although both linkage configurations yielded comparable spectral profiles, the consistently superior ROS generation by shorter-chain dimers aligns with Zhou's earlier findings, further substantiating 3M's remarkable ROS-generating capacity for synergistic PDT-PTT.

3.3 Porphyrin and phthalocyanine dimers

Porphyrins are extended π -conjugated macrocyclic compounds comprising four pyrrole subunits joined by methine bridges, forming a delocalized aromatic system.¹⁰⁶ This framework imparts intense absorption in the visible and near-infrared regions, high ISC efficiency, and efficient singlet-oxygen generation, positioning porphyrins and their derivatives as compelling candidates for PDT. Their modular architecture also permits chemical modification at peripheral sites and coordination with various central metal ions, enabling precise tuning of photophysical, chemical, and biological properties. Collectively, these features support their broad utility in imaging, diagnosis, and cancer therapy. Porphyrin derivatives have been extensively explored for PDT, and several are already in clinical use. Photofrin, Verteporfin, and Foscan, approved by the FDA or EMA, serve as efficient singlet-oxygen generators. Beyond these classical porphyrins, next-generation derivatives have also advanced to clinical trials or gained regulatory approval. Lutrin (lutetium texaphyrin, $\lambda_{max} \approx 732$ nm) progressed to clinical trials, whereas Redaporfin (a halogenated bacteriochlorin,

$\lambda_{max} \approx 749$ nm) and Tookad (a Pd(II) bacteriopheophorbide, $\lambda_{max} \approx 746$ nm) were recently approved for PDT applications.^{107,108} Similar to other dimers, porphyrin dimers not only enhance light absorption and singlet-oxygen generation but also address a key limitation of monomeric porphyrins in two-photon PSs. A persistent drawback, however, is their typically low 2PA (σ_2) cross-sections, often around 1 GM, which hampers deep-tissue treatment under two-photon excitation. Typical chromophores exhibit low 2PA cross-sections (~ 1 –100 GM), which are insufficient for clinical two-photon PDT (verteporfin ≈ 50 GM; Photofrin ≈ 10 GM).

Fortunately, conjugated dimerization overcomes this constraint: dimer formation can increase the 2PA cross-section by up to ≈ 500 -fold. For example, Anderson *et al.*^{107,108} synthesized a series of conjugated porphyrin dimers bearing electron-accepting aromatic terminals that both red-shifted one- and two-photon absorption bands and enhanced 2PA. Among these, P1 achieved ≈ 17000 GM at 916 nm (Fig. 32). The dimers in the series also exhibited high singlet-oxygen quantum yields in methanol ($\Phi_{\Delta} = 0.60, 0.54, 0.70, 0.16,$ and 0.69 for compounds P1–5, respectively). One-photon PDT assays indicated that the cationic dimers (P1–3) displayed activity comparable to that of verteporfin, whereas the anionic analogs (P4–5) were less active. An *in vivo* proof-of-concept was demonstrated: intravenous administration of P1 at 10 mg kg^{-1} , followed by 15 min of irradiation, consistently induced blood-vessel closure in treated animals. In addition to enhancing 2PA, porphyrin dimers also intensify absorption within the tissue-transparent red/NIR window (~ 600 –850 nm). Closely related dimers (P2, P3, and P4) exhibit the longest-wavelength absorption maxima at ~ 705 –712 nm with $\epsilon \approx 6.2 \times 10^4 \text{ M}^{-1} \text{ cm}^{-1}$, whereas more extensively π -conjugated dimers (P4 and P2) display ϵ values approaching $1.2 \times 10^5 \text{ M}^{-1} \text{ cm}^{-1}$ within approximately 746–769 nm. These extinction coefficients not only compare favorably with but frequently surpass those of clinical PSs, such as verteporfin ($3.8 \times 10^4 \text{ M}^{-1} \text{ cm}^{-1}$ at 690 nm; lutetium texaphyrin: $4.2 \times 10^4 \text{ M}^{-1} \text{ cm}^{-1}$ at 732 nm; Tookad: $1.09 \times 10^5 \text{ M}^{-1} \text{ cm}^{-1}$ at 763 nm). The synergy of enlarged 2PA cross-sections, strong one-photon extinction, and substantial Φ_{Δ} positions porphyrin dimers as promising candidates for one- and two-photon PDT targeting deep-seated tissues.

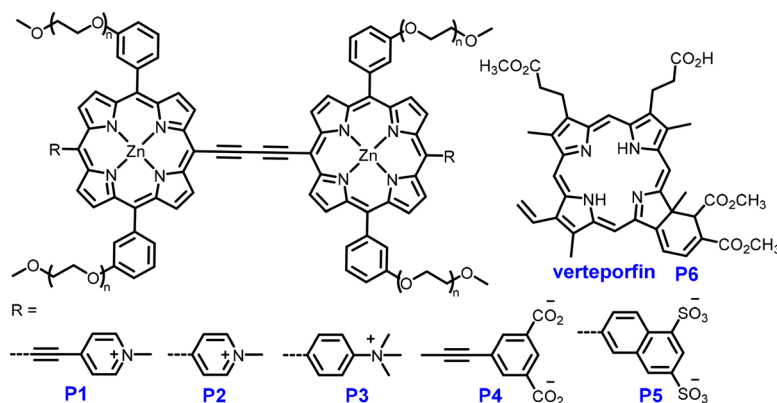


Fig. 32 Zinc porphyrin dimers bearing diverse substitutions.



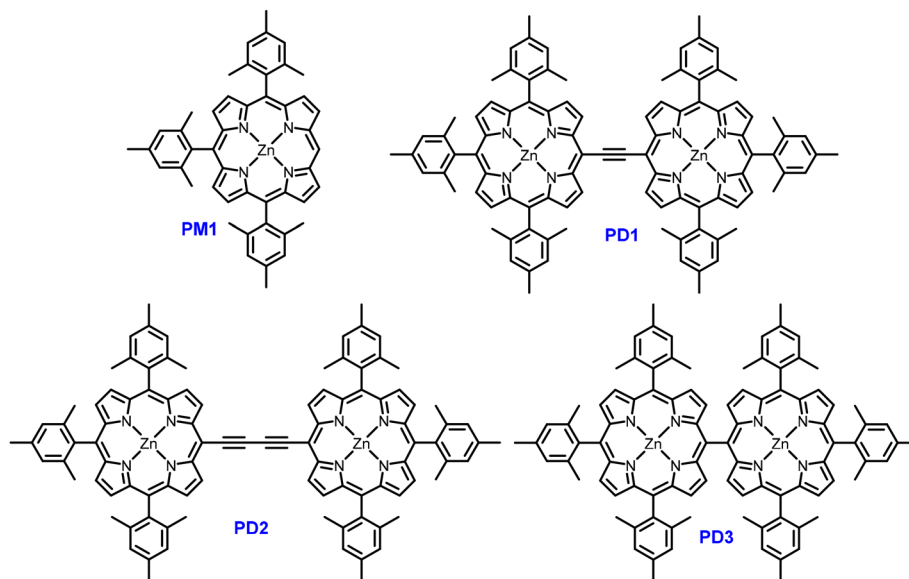


Fig. 33 Structures of zinc porphyrin dimers with various linkers.

In a complementary study, Matczyszyn and co-workers¹⁰⁹ systematically examined zinc porphyrins in monomeric and dimeric forms, connected by single, ethyne, or diethyne linkers (PD1–3, Fig. 33), to assess the influence of π -delocalization on two-photon absorption and singlet oxygen generation. Relative to the monomer ($\Phi_{\Delta} = 15\%$), the dimers displayed markedly enhanced Φ_{Δ} values, ranging from 27% to 47% depending on the linker. Notably, the ethyne- and diethyne-bridged dimers adopted nearly planar geometries, enabling extended π -conjugation and thereby markedly increasing Φ_{Δ} values to 35% and 47%, respectively. Concurrently, the two-photon absorption cross sections rose substantially, reaching maxima of ~ 8000 GM at 725 nm, far exceeding that of the monomer (~ 1000 GM). The two-photon singlet oxygen production metric ($\sigma_2 \times \Phi_{\Delta}$) reached ~ 3700 GM in the diethyne-linked dimer, nearly 500 times higher than that of commercial tetraphenylporphyrin. Spectroscopic analysis revealed broadened and bathochromically shifted Q-bands in the dimers, consistent with stronger excitonic coupling and enhanced electron delocalization. Remarkably, even the sterically hindered, non-conjugated

dimer exhibited a twofold increase in Φ_{Δ} relative to the monomer, underscoring that dimerization intrinsically promotes ROS generation regardless of the linker. Overall, these findings demonstrate that structural optimization through conjugated linkers between porphyrin macrocycles enhances both two-photon absorption and singlet oxygen photogeneration, offering a compelling design strategy for efficient PSs suitable for deep-tissue PDT.

Ventura *et al.*¹¹⁰ developed a theranostic agent comprising a linear π -conjugated Zn(II) porphyrin dimer linked at both ends to [GdDOTA]-type complexes, thus integrating PDT and MRI capabilities (Fig. 34). The Zn-porphyrin dimer exhibited pronounced red-shifted absorption ($\epsilon = 1.17 \times 10^5 \text{ M}^{-1} \text{ cm}^{-1}$ at 746 nm) and efficient singlet oxygen generation, with Φ_{Δ} values of 0.36 in DMSO and ~ 0.21 – 0.29 in aqueous media. Two-photon absorption measurements revealed high cross-sections (> 7000 GM) within the 870–940 nm range, peaking at 9400 GM at 920 nm. The corresponding two-photon singlet oxygen sensitization value ($\sigma_2 \times \Phi_{\Delta}$) reached ~ 3400 GM, underscoring the dimer's considerable potential for deep-tissue PDT. In cellular

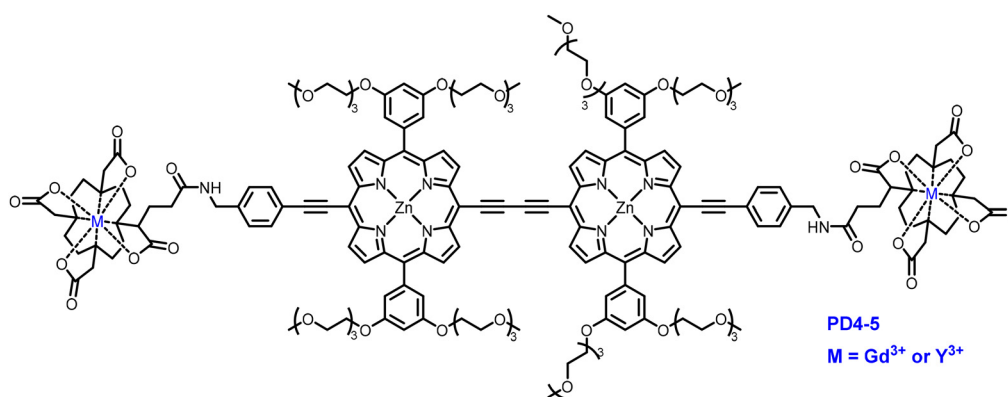


Fig. 34 Structures of magnetic-resonance-imaging (MRI)-active Zn(II) porphyrin dimers.



assays, the amphiphilic structure facilitated efficient uptake, resulting in 26-fold higher internalization relative to $[\text{GdDTPA}]^{2-}$ at a Gd concentration of 4 μM . Upon irradiation (740 nm, 30 min), a 50% reduction in cell viability was observed at a power of 40 J cm^{-2} , while dark toxicity remained negligible ($\text{IC}_{50} > 1 \mu\text{M}$). Notably, both one-photon (740 nm) and two-photon (910 nm) excitation induced marked cytotoxicity in HeLa cells, demonstrating the system's dual activation capability. As an MRI agent, the conjugate exhibited a relaxivity of 14.4 $\text{mM}^{-1} \text{s}^{-1}$ (per Gd, 40 MHz, 25 $^{\circ}\text{C}$), approximately fourfold higher than that of commercial counterparts. This advantage was further aided by strong cellular uptake, driven by the amphiphilic design. Therefore, this dual-function system enables real-time imaging of tumor accumulation and treatment while offering a flexible therapeutic window: one-photon PDT for superficial tumors and two-photon PDT for deeper-seated malignancies. Such integration of high-performance porphyrin dimers with MRI-active Gd complexes marks a promising advancement toward personalized, image-guided phototherapies.

Owing to their strong planarity and hydrophobicity, porphyrins often exhibit distinct self-assembly behavior upon dimerization. In 2017, Xie *et al.*¹¹¹ synthesized porphyrin dimers containing Se-Se, S-S, and C-C bonds (TPP-SeSe, TPP-SS, and TPP-CC; Fig. 35), which readily self-assembled into NPs *via* a facile nanoprecipitation method. In organic solvents, the dimers exhibited efficient $^1\text{O}_2$ generation; although their activity declined in aqueous media, the assembled NPs retained moderate ROS production. Notably, the Se-Se and S-S bonds responded to intracellular reductive species such as GSH. For instance, the hydrodynamic diameter of TPP-SeSe NPs increased from 193.5 nm to 970 nm after 1.5 h of incubation in 10 mM GSH and further expanded to 3745 nm after 24 h, indicating greater redox-responsiveness than the S-S and C-C analogues. This elevated sensitivity promoted intracellular structural disruption, thereby enhancing photodynamic cytotoxicity.

In a related study, two structurally distinct porphyrins were linked *via* disulfide bonds (Fig. 36) to form TPC-SS and TPP-SS dimers, both of which spontaneously self-assembled into well-defined spherical NPs.¹¹² Photophysical characterization revealed

that TPC-SS NPs exhibited a high molar extinction coefficient of $9.90 \times 10^4 \text{ M}^{-1} \text{ cm}^{-1}$ at 650 nm, considerably higher than that of TPP-SS. Despite aggregation-induced fluorescence quenching, the 1,3-diphenylisobenzofuran consumption rate was 4.26-fold greater than that of the control, indicating a notably enhanced $^1\text{O}_2$ generation capacity. Furthermore, TPC-SS nanoparticles demonstrated a photothermal conversion efficiency of $\sim 37\%$ and substantially elevated photoacoustic signals in tumor tissues. Following intravenous administration, tumor photoacoustic intensity progressively increased, reaching a peak at 12 h, indicative of effective tumor accumulation. Under continuous irradiation, TPC-SS nanoparticles produced synergistic photothermal and photodynamic effects, resulting in marked tumor growth inhibition. Although disulfide linkages were employed, the study did not evaluate the influence of intracellular reductive species on the assemblies' stability or performance. Collectively, these findings demonstrate that porphyrin dimers can spontaneously assemble into responsive, functional nanoparticles without external carriers. These assemblies preserve photosensitizing capacity while harnessing cleavable dynamic bonds to enable stimulus responsiveness, thereby enhancing combined photodynamic and photothermal therapeutic efficacy. This design strategy provides valuable direction for the development of carrier-free, stimuli-responsive, and tumor-targeted therapeutic systems.

Like porphyrins, phthalocyanines are rigid, planar macrocycles with a highly conjugated 18- π electron system, which confers distinctive optical and electronic properties, including strong visible-NIR absorption and exceptionally high molar extinction coefficients. Given these advantages, phthalocyanines have attracted substantial attention as both photosensitizers and photothermal agents.^{113,114}

In addition to peripheral substitution, axial metal-ligand coordination has emerged as an effective means of modulating their supramolecular structures and associated optoelectronic properties. For example, Huang and co-workers¹¹⁵ assembled four supramolecular complexes (1–4) from unsubstituted zinc(II) phthalocyanine (ZnPc) dimers *via* axial coordination with bipyridine derivatives. Single-crystal X-ray diffraction revealed distinct dimeric configurations: H-shape (1), saddle-like (2), and

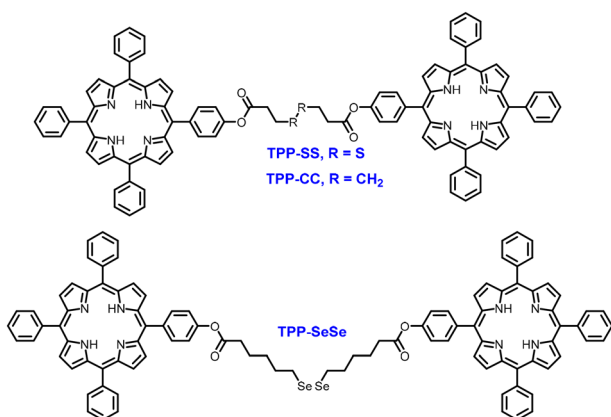


Fig. 35 Structures of GSH-activated porphyrin dimers.

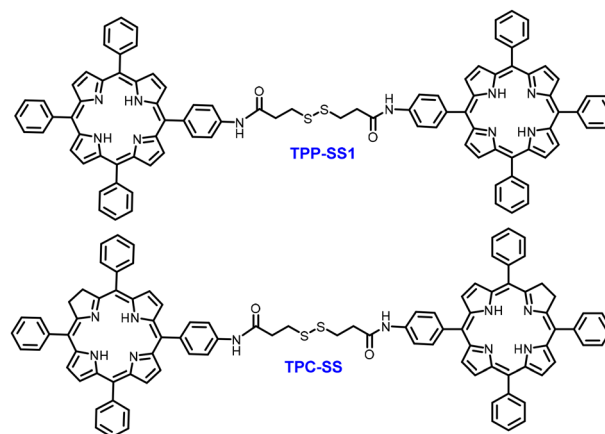


Fig. 36 Structures of disulfide-bonded porphyrin dimers.



Z-shape (3 and 4). Notably, a pair of saddle-like dimers from complex 2 interlocked to form a tetrameric assembly, while complexes 3 and 4, bridged by semi-rigid ligands, exhibited tighter packing and enhanced intermolecular interactions. In the crystal structure of complex 4, the ligand's naphthalimide moiety intercalated between adjacent ZnPc macrocycles, forming a slipped "ZnPc–naphthalimide–ZnPc" sandwich stabilized by dual π – π interactions. These supramolecular architectures exhibited broadened solid-state Q-band absorption across the visible–NIR region, substantial fluorescence quenching due to excitonic coupling, and exceptionally efficient photothermal effects. Upon laser irradiation, complexes 3 and 4 demonstrated robust photothermal conversion, with surface temperatures reaching 85.7 °C and 89.2 °C, respectively, and a photothermal efficiency of up to 66.6% under 730 nm excitation. This elevated performance surpassed that of most reported organic photothermal materials, enabling applications across photoacoustic imaging, superficial antimicrobial therapy, and cancer PTT.

While porphyrins and phthalocyanines possess highly planar π -conjugated frameworks that confer strong molar extinction coefficients and efficient NIR absorption, these same features often lead to poor solubility and a pronounced tendency toward aggregation, which may impair their performance in biological environments. Although dimerization strategies can improve photophysical performance, they may simultaneously intensify aggregation. Moving forward, rational molecular design incorporating hydrophilic substituents or responsive nanoassemblies presents a promising strategy to mitigate these challenges, ultimately enhancing the therapeutic efficacy and translational potential of chromophore-based systems.

3.4 Cyclometalated complex dimers

Phosphorescent transition metal complexes are central to organic light-emitting diode technologies, as their strong SOC enables efficient harvesting of triplet excitons, which are otherwise non-emissive. This mechanism substantially enhances device performance by permitting near-total exciton utilization. Recent research has shifted attention from mononuclear to multinuclear cyclometalated complexes, where the inclusion of multiple metal centers markedly influences excited-state dynamics. Notably, dinuclear Ir(III) and Pt(II) systems exhibit considerably faster radiative decay rates than their mononuclear counterparts. These enhancements arise from strengthened coupling between the lowest triplet and adjacent singlet states, thereby increasing the probability of phosphorescence. In addition to emission kinetics, these architectures offer considerable structural tunability; modifying bridging or ancillary ligands allows fine control over photophysical properties, from ultrafast decay to dual-emission behaviors where phosphorescence and fluorescence coexist.

Kozhevnikov and co-workers^{116–120} systematically investigated how ligand design governs the photophysics of Ir(III) complexes. As illustrated in Fig. 37, they first demonstrated that the geometry of the cyclometalating unit critically influences phosphorescence efficiency: relocating the cyclometalating function from the terminal to the core aryl ring (Ir-1 \rightarrow Ir-2)

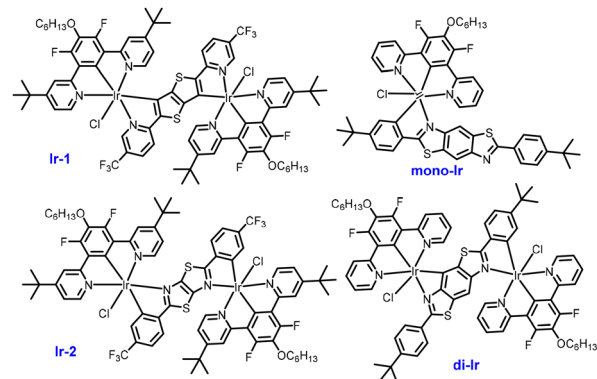


Fig. 37 Ir(III) dimeric complexes with different ligands.

substantially improved both the phosphorescence rate and quantum yield. This enhancement stemmed from diminished exchange interaction in the lowest triplet state (T_1), attributed to a more uniform distribution of frontier orbital electron density across the ligand. Building on this concept, they further reduced exchange interaction by π -expanding the ligand framework through benzannulation between the two thiazole rings of the Ir-2 bridging unit. This modification yielded a dinuclear complex (di-Ir) and its mononuclear analogue (mono-Ir). In degassed CH_2Cl_2 , mono-Ir emitted yellow light at 552 nm ($\Phi_{\text{PL}} = 70\%$, $\tau = 7.85$ ms), while di-Ir exhibited red-shifted emission at 560 nm with greater efficiency ($\Phi_{\text{PL}} = 85\%$) and a doubled radiative rate ($1.90 \times 10^5 \text{ s}^{-1}$). Both complexes efficiently sensitized singlet oxygen ($\Phi_{\Delta} = 78\%$ for mono-Ir, 71% for di-Ir), underscoring how cyclometalation geometry and ligand benzannulation jointly enhance phosphorescence and photodynamic performance.

Transition metal complexes are promising PSs for clinical application owing to their biocompatibility, efficient cellular uptake, and potent ROS generation or photocatalysis. However, Ru- and Ir-based complexes often exhibit short-wavelength absorption, which restricts tissue penetration and elevates phototoxicity. To address these challenges, Lanoë and co-workers¹²¹ developed Ir(III) complexes featuring enhanced two-photon absorption for TPA-PDT (Fig. 38). In their design, two Ir(III) centers were bridged by a non-conjugated bis(pyridylbenzimidazole) linker. Both the monomeric IrL1 and dimeric Ir2L2 displayed phosphorescence in the orange-red region at 610 and 625 nm, respectively, with comparable quantum yields ($\sim 24\%$). Notably, Ir2L2 exhibited fourfold greater brightness than IrL1 under both one-photon and two-photon excitation. It also achieved a markedly higher singlet oxygen generation efficiency, with a figure of merit ($\sigma_2 \times \Phi_{\Delta}$) of 40, compared to only five for the monomer. Under 800 nm TPA excitation, both complexes efficiently generated intracellular ROS and induced cancer cell death, affirming their potential as deep-tissue PDT agents. Overall, this study demonstrates that supramolecular dimerization effectively amplifies two-photon brightness and phototoxicity, providing a viable route to extend the clinical applicability of transition metal complexes in phototherapy.

Cyclometalated complexes not only induce anticancer effects through intracellular ROS production but also operate



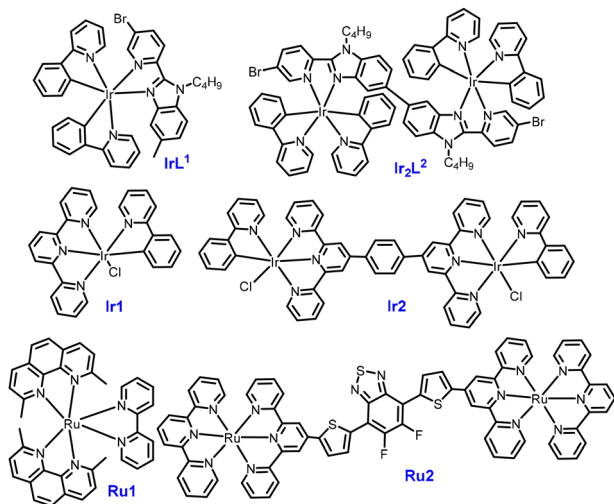


Fig. 38 Monomeric and dimeric Ir(III) and Ru(II) complexes featuring different linkers.

through alternative mechanisms, such as the photo-oxidation of cellular coenzymes. In particular, oxidation of reduced NADH and its phosphorylated analogue NAD(P)H, key reducing equivalents in respiration, biosynthesis, and redox homeostasis, offers a viable route to disrupt cancer metabolism, even under hypoxic conditions. In 2022, Huang *et al.*^{122,123} reported a dinuclear Ir(III) complex (Ir2) that exhibited excellent photostability and strong phosphorescence, serving as both a PS and an efficient photocatalyst for the oxidation of NAD(P)H and amino acids. Notably, Ir2 exhibited photocatalytic activity over 13 times greater than its mononuclear analogue Ir1, underscoring a pronounced synergistic effect. To further enhance absorption and charge-transfer capacity, D–A–D chromophores were introduced into Ru(II) bis-terpyridyl frameworks, yielding a dinuclear complex (Ru2) with red-shifted absorption ($\lambda_{\text{max}} = 521 \text{ nm}$, $\epsilon = 65\,620 \text{ L mol}^{-1} \text{ cm}^{-1}$) relative to Ru1 (478 nm, $\epsilon = 20\,331 \text{ L mol}^{-1} \text{ cm}^{-1}$).¹²⁴ This design enabled efficient type I and type II ROS generation and markedly accelerated NAD(P)H oxidation, with Ru2 achieving turnover frequencies of 2117–2525 h⁻¹, surpassing the performance of most reported metal-based photocatalysts.

Although incorporating D–A–D fluorophores into metal complexes enhances both absorption characteristics and photodynamic efficacy, these designs generally restrict light absorption to the visible region. Prior studies have revealed that transition metal complexes bearing diketopyrrolopyrrole (DPP) chromophores exhibit substantially red-shifted absorption and emission, shorter fluorescence lifetimes, reduced quantum yields, and elevated triplet-state populations. Building on this strategy, Huang and co-workers¹²⁵ conjugated DPP chromophores with transition metal complexes (Fig. 39), constructing a series of PSs activatable in the NIR region. Among these, the D–A–D-conjugated dinuclear Ru(II) complex Ru3 exhibited broad, intense absorption spanning the visible to NIR region, with a peak near 700 nm ($\epsilon = 6.6 \times 10^5 \text{ M}^{-1} \text{ cm}^{-1}$). This behavior stood in marked contrast to earlier dinuclear Ru(II)

complexes containing low-conjugation linkers (*e.g.*, phenylene), whose absorption peaks were confined to $\sim 450 \text{ nm}$. More importantly, Ru3 generated notably higher singlet oxygen yields than both its analogue Ru1 and the clinically employed PS Ce6, whose absorption at 700 nm is inherently limited. Under 700 nm excitation, Ru3 efficiently catalyzed NADH oxidation with a TOF of 152 h⁻¹, surpassing previously reported Ir(III)-based photocatalysts. In parallel, a related dinuclear Ru(II) complex, Ru4 (Fig. 39), not only preserved potent photosensitizing and photocatalytic activity but also catalyzed NAD(P)H oxidation, thereby disrupting the intracellular antioxidant defense system in cancer cells.¹²⁶ Mechanistic studies revealed that Ru4 induced intracellular redox imbalance, endoplasmic reticulum stress, and cytoplasmic Ca²⁺ overload, collectively resulting in irreversible cancer cell death. Consequently, Ru4 demonstrated outstanding anticancer efficacy. Under normoxic conditions and 700 nm irradiation, Ru4 achieved nanomolar IC₅₀ values (0.02–0.06 μM) and a phototherapeutic index as high as 637. Notably, Ru4 remained effective even under hypoxia (1% O₂), achieving IC₅₀ values as low as 0.6 μM .

Chao *et al.*¹²⁷ synthesized a ferrocene-bridged dinuclear cyclometalated Ir(III) complex (Ir₂BPIFc) designed for photo-uncaging-mediated photoimmunotherapy targeting hypoxic melanoma (Fig. 40). The ferrocene bridge effectively quenched the intrinsic emission of Ir₂BPIFc; however, upon irradiation with a 405 nm LED or a femtosecond laser at 970 nm, homolytic cleavage released mononuclear IrPICp and Fe²⁺ ions, accompanied by a restoration of phosphorescence at $\sim 565 \text{ nm}$. High-resolution mass spectrometry, nuclear magnetic resonance, and trapping experiments confirmed the formation of carbon-centered radicals, further substantiated by EPR and deuterium substitution. Mechanistic studies using ultrafast spectroscopy and DFT revealed that efficient metal-to-ligand charge transfer of the Ir(III) center, coupled with single electron transfer from ferrocene, initiated the generation of cyclopentadienyl radicals and radical-containing triplet states. Notably, the three-photon absorption cross-section reached $1.495 \times 10^{-78} \text{ cm}^6 \text{ s}^2 \text{ photon}^{-2}$ at 970 nm. Under hypoxic (2% O₂) tumor-mimicking conditions, facilitated multimodal ROS generation *via* (i) carbon-centered

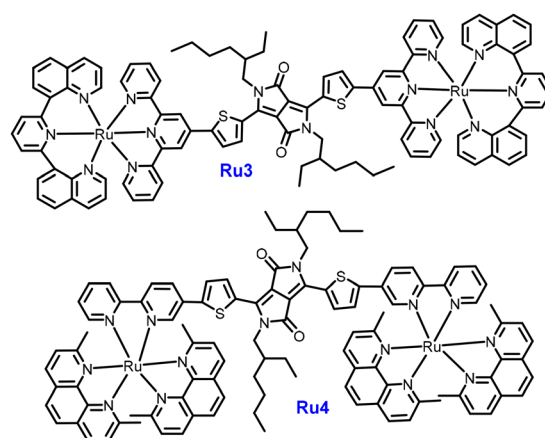


Fig. 39 Ru(II) complexes dimer bearing diketopyrrolopyrrole as linker.



radicals, (ii) Fenton reactions from Fe^{2+} , and (iii) photo-uncaged type-I PDT while simultaneously disrupting redox homeostasis through NADH and GSH oxidation. The hydroxyl radical yield of Ir_2BPIFc ($10\ \mu\text{M}$) was approximately 3.5-fold greater than that of IrPICp ($20\ \mu\text{M}$), despite identical Ir content, underscoring the central role of the photolysis pathway. Biologically, Ir_2BPIFc localized predominantly to mitochondria and exhibited potent photocytotoxicity against A375 cells under hypoxia ($\text{IC}_{50} = 2.06\ \mu\text{M}$, $405\ \text{nm}$, $20\ \text{mW cm}^{-2}$, $10\ \text{min}$), in contrast to its minimal dark toxicity ($\text{IC}_{50} = 16.32\ \mu\text{M}$).

Liu *et al.*¹²⁸ developed a heterotrinnuclear $\text{Ir(III)}\text{-Gd(III)}$ complex ($\text{Ir}_2\text{Gd1}$), described as a “mito-bomb,” for mitochondria-targeted, bimodal-imaging-guided precision cancer therapy (Fig. 40). This single-molecule approach overcomes the inherent limitations of nanocomposite-based theranostic platforms, which often suffer from complex formulation, poor reproducibility, and ambiguous pharmacokinetics. $\text{Ir}_2\text{Gd1}$ exhibited a Φ_{Δ} of 0.14 and functioned as both a PS and a high-relaxivity MRI contrast agent ($9.42\ \text{mM}^{-1}\ \text{s}^{-1}$). Upon light activation, it localizes to mitochondria and generates $^1\text{O}_2$, promoting cytochrome *c* release and triggering apoptosis and pyroptosis *via* the caspase-3/GSDME axis. It also photocatalytically oxidizes NADH, disrupts the electron transport chain, and depletes ATP, thereby compromising mitochondrial function. Notably, $\text{Ir}_2\text{Gd1}$ exhibited dark cytotoxicity comparable to cisplatin (A549, $\text{IC}_{50} = 30.9\ \mu\text{M}$ *vs.* $33.4\ \mu\text{M}$) and maintained high potency under hypoxia (A549, $\text{IC}_{50} = 1.7\ \mu\text{M}$ for normoxia, $1.8\ \mu\text{M}$ for hypoxia). However, despite its promising multimodal properties, its short excitation wavelength ($390\ \text{nm}$) remains a critical drawback, limiting tissue penetration and increasing the risk of phototoxicity.

Transition-metal complexes are widely recognized as promising candidates for PDT owing to their intrinsic heavy-atom effect, efficient ISC, and tunable coordination environments, features that support both robust ROS generation and, in some

cases, additional catalytic functionality. Nonetheless, several key challenges continue to impede their broader clinical translation. Most notably, their absorption in the ultraviolet-visible region restricts tissue penetration, limiting therapeutic efficacy to superficial tumors. Furthermore, structural complexity often results in poor aqueous solubility, aggregation, and physiological instability, thereby compromising pharmacokinetic behavior. The inclusion of heavy metals such as Ir, Ru, or Pt further raises concerns about long-term toxicity, metabolic clearance, and off-target accumulation. Although strategies such as conjugation with D-A-type chromophores and encapsulation into nanocarriers offer partial solutions, fundamental barriers, including short excitation wavelengths and systemic toxicity, remain unresolved.

3.5 D-A structure-based dimers

In designing NIR dyes, a common approach to achieving a small optical gap involves extending the π -conjugation, as exemplified by cyanine derivatives. Alternatively, donor-acceptor systems offer a tunable route to HOMO-LUMO gap narrowing, since the donor and acceptor units predominantly determine the HOMO and LUMO levels, respectively. This modularity enables precise electronic control. Notably, strong electron-accepting units with low-lying LUMO levels promote both red-shifted absorption and enhanced stability in air and under light irradiation.

Intramolecular B-N coordination has proven to be an effective strategy for enhancing electron-accepting strength while minimally disrupting the π -conjugated framework. Boron coordination thus serves as a powerful tool for lowering LUMO levels in D-A dyes, as evidenced by various boron-bridged chromophores such as N-B-N-bridged BODIPY derivatives and O-B-O-bridged boron diketonates.¹²⁹ In 2018, Wakamiya *et al.*¹³⁰ reported BF_2 -bridged azafulvene dimers as potent electron acceptors that were subsequently integrated with donor units to construct three distinct dyes (Fig. 41). In CH_2Cl_2 , dyes 1 and 2 displayed absorption maxima at $625\ \text{nm}$ ($\log \epsilon = 4.76$) and $457\ \text{nm}$ ($\log \epsilon = 4.57$), respectively, whereas the D-A-D dye 3 exhibited intense NIR absorption at $922\ \text{nm}$ ($\log \epsilon = 5.06$), with an absorption edge extending to $1150\ \text{nm}$. Remarkably, dye 3 retained 97% of its absorbance after 50 h of irradiation in non-degassed toluene, underscoring its exceptional photostability and resistance to oxidative degradation (Table 5).

Building on the BF_2 -bridged azafulvene acceptor framework, Liu and co-workers¹³¹ extended the design by incorporating electron-donating groups to develop a series of D-A-D type chromophores (Fig. 41). Specifically, 1,2-bis(4-*N,N*-dioctylamino-phenyl)-1,2-diphenylethene served as the donor for BAF4, while TPE, 1,2-bis(4-methoxyphenyl)-1,2-diphenylethene, and 1,2-bis(4-*N,N*-dimethylaminophenyl)-1,2-diphenylethene were employed to afford BAF1-3 as analogs. Spectroscopically, BAF1 exhibited an absorption maximum at $625\ \text{nm}$ ($\epsilon = 4.8 \times 10^4\ \text{M}^{-1}\ \text{cm}^{-1}$), while BAF2 and BAF3 displayed progressively red-shifted peaks at $685\ \text{nm}$ ($\epsilon = 4.3 \times 10^4\ \text{M}^{-1}\ \text{cm}^{-1}$) and $882\ \text{nm}$ ($\epsilon = 1.7 \times 10^4\ \text{M}^{-1}\ \text{cm}^{-1}$), respectively, corresponding to the increasing donor strength of methoxy and *N,N*-dimethylamino substituents. Strikingly, BAF4 further extended its λ_{abs} to $1000\ \text{nm}$

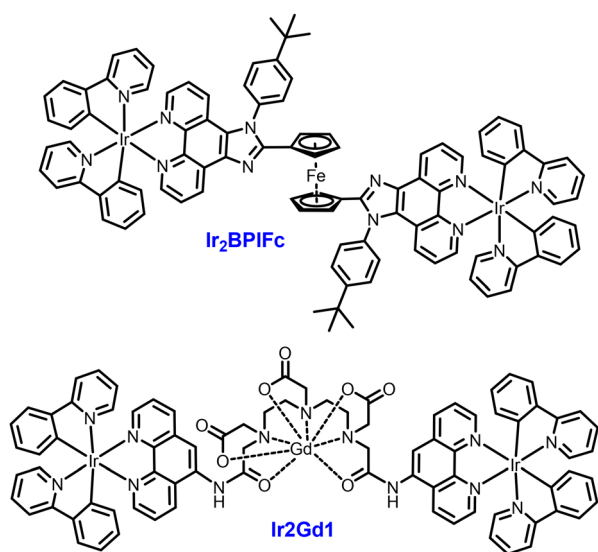
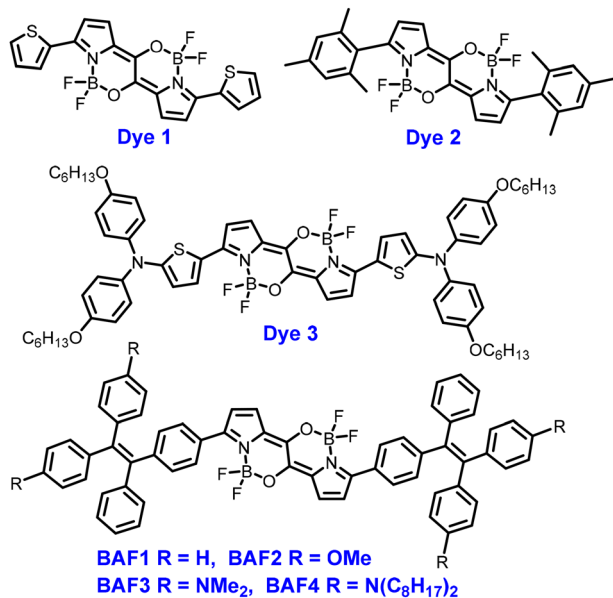


Fig. 40 Ferrocene- and Gd(III)-bridged dinuclear cyclometalated Ir(III) complexes.



Fig. 41 BF₂-bridged azafulvene dimers.

($\epsilon = 1.6 \times 10^4 \text{ M}^{-1} \text{ cm}^{-1}$), attributable to the superior electron-donating capacity of the *N,N*-dioctylamino group. The active intramolecular motions introduced by TPE units and long alkyl chains rendered BAF4 and its nanoparticles non-emissive in both solution and the aggregated state. This non-radiative relaxation mechanism contributed to an exceptionally high photothermal conversion efficiency of 80%, surpassing most reported organic photothermal agents. Biologically, BAF4 nanoparticles exhibited favorable biocompatibility, efficient tumor accumulation *via* the EPR effect, strong photoacoustic imaging capability, and notable photothermal therapeutic performance against both subcutaneous 4T1 tumors and deep-seated tumor models, resulting in substantial inhibition of tumor growth and metastasis *in vivo*.

Recent efforts have focused on addressing a long-standing limitation of D–A systems: their intrinsically low molar extinction coefficients (typically $1\text{--}2 \times 10^4 \text{ M}^{-1} \text{ cm}^{-1}$). Inspired by the strong electron-withdrawing ability of the BF₂-bridged azafulvene acceptor core, Tang and Fan's group¹³² employed it as an acceptor and systematically tuned donor groups to construct three novel PTAs, namely TPEBF, TPABF, and OTTBF, by linking TPE, TPA, and alkoxy-substituted TPA, respectively. These rationally designed molecules exhibited markedly enhanced absorption, with maximum λ_{abs} at 714 nm ($\epsilon = 6.34 \times 10^4 \text{ M}^{-1} \text{ cm}^{-1}$), 758 nm ($\epsilon = 6.73 \times 10^4 \text{ M}^{-1} \text{ cm}^{-1}$), and 892 nm ($\epsilon = 7.21 \times 10^4 \text{ M}^{-1} \text{ cm}^{-1}$). Notably, OTTBF extended its absorption tail to 1100 nm while still maintaining $\epsilon = 1.68 \times 10^4 \text{ M}^{-1} \text{ cm}^{-1}$ at 1064 nm, thereby enabling superior light-harvesting in the NIR-II region. Fluorescence emission in toluene was observed at 792 nm, 880 nm, and 1058 nm, respectively, highlighting the potential for dual photothermal/fluorescence imaging. Importantly, the PCEs of the corresponding NPs reached 22.5%, 37.3%, and 54.1% for TPEBF, TPABF, and OTTBF, respectively, with theoretical calculations attributing the efficiency of OTTBF to its narrow HOMO–LUMO gap and efficient nonradiative decay. Encapsulated into water-dispersible NPs, OTTBF exhibited remarkable photothermal performance under 1064 nm irradiation at a power density as low as 0.7 W cm^{-2} , the lowest reported threshold for NIR-II PTT to date, demonstrating excellent chemo- and photo-stability and strong translational potential for deep-seated tumor ablation (Fig. 42).

In 2023, Tang and co-workers¹³³ proposed a dual-acceptor engineering strategy to construct NIR-II-active aggregation-induced emission luminogens (AIEgens) for multimodal phototheranostic applications. As illustrated in Fig. 43, two molecular series were developed: the 1A system (D'–D–A–D–D'), comprising 2TT-BTD, 2TT-PTD, 2TT-DPTDQ, and 2TT-BBTD) and the 2A system (D'–D–A–A–D–D'), comprising 2TT-2BTD, 2TT-2PTD, 2TT-2DPTDQ, and 2TT-2BBTD). Within these frameworks, BTD, PTD, DPTDQ, and BBTD acted as progressively stronger acceptors, thiophene served as both donor and π -bridge, and

Table 5 Photophysical properties (absorption/emission maxima and fluorescence quantum yield), ROS and heat generation capability of various D–A molecules

Molecules	λ_{abs} (nm)	λ_{em} (nm)	Φ_{F}	ROS	Φ_{Δ}	PCE	Synthetic yield	Ref.
BAF1	625	—	<0.001	—	—	39%	68%	131
BAF2	685	—	—	—	—	41%	72%	
BAF3	882	—	—	—	—	47%	65%	
BAF4	1000	—	—	—	—	80%	57%	
TPEBF	714	792	—	—	—	22.5%	73%	132
TPABF	758	880	—	—	—	37.3%	—	
OTTBF	892	1058	—	—	—	54.1%	85.7%	
2TT-2BTD	509	668	—	—	—	—	89%	133
2TT-2PTD	546	716	—	—	—	—	92%	
2TT-2DPTDQ	688	886	0.016	—	—	—	98%	
2TT-2BBTD	773	1004	0.0025	—	—	41.7%	83%	
IID-PS-S	650	765	0.014	$\text{O}_2^{\bullet-}$	—	22%	38.2%	134
IID-PS-Se	677	775	0.006	$^1\text{O}_2$	0.15	35%	35.8%	
4THTPB	732	1058	0.03	—	—	87.6%	83%	135
4TT-PBPT	700	1026	0.019	—	—	73.8%	86.5%	136
4AM-OS	795	~930	—	$^1\text{O}_2, \text{O}_2^{\bullet-}, \bullet\text{OH}$	—	—	41%	137
dB TIC-S	735	~820	0.015	—	—	68.5%	44%	138
dB TIC-D	732	~820	0.02	—	—	61.4%	64%	



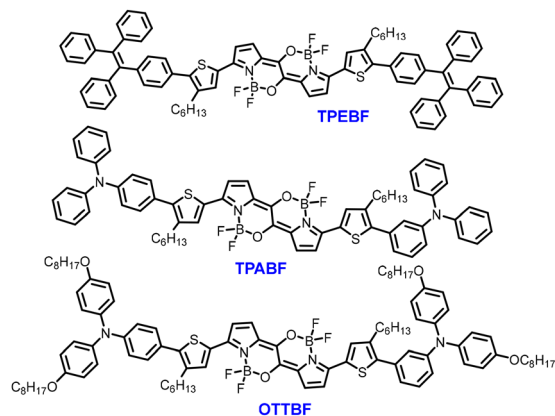


Fig. 42 BF₂-bridged azafulvene dimers with tunable donors.

TPA units contributed donor and rotor functionalities. Alkyl chains were incorporated to modulate steric hindrance and fine-tune backbone planarity.

Spectral analyses revealed that strengthening acceptor units in the 1A series produced bathochromic shifts in both absorption (511–824 nm) and emission (663–1104 nm). In contrast, the introduction of a second acceptor in the 2A series further increased ϵ (up to $4.29 \times 10^4 \text{ M}^{-1} \text{ cm}^{-1}$ for 2TT-2BBTD), albeit with partial blue-shifts, indicating that dual-acceptor substitution did not yield a linear enhancement in electrophilicity. Structural analyses showed enlarged dihedral angles in the 2A system, which disrupted conjugation and effectively converted ACQ molecules into AIE-active emitters. Functional evaluations identified 2TT-2BBTD nanoparticles as lead candidates,

exhibiting absorption and emission maxima at 799 and 1065 nm, respectively, with emission extending to 1400 nm. These nanoparticles achieved a PCE of 41.7% and demonstrated substantial superoxide generation for type-I PDT. These features enabled NIR-II fluorescence, photoacoustic, and photothermal imaging-guided trimodal photodynamic/photothermal therapy in orthotopic breast tumor models. Collectively, dual-acceptor engineering provides a robust molecular design strategy to simultaneously enhance molar absorptivity, extend NIR-II emission, amplify AIE characteristics, and unify synergistic ROS and thermal generation.

Dual-acceptor engineering within twisted D–A–A–D frameworks represent a promising yet synthetically demanding strategy for enhancing molar absorptivity, suppressing nonradiative decay, and elevating phototheranostic efficacy. Fan's group¹³⁴ recently developed D–A molecules featuring triple-acceptor architectures for combined PTT and PDT (Fig. 44). The prototype PS, composed of [1,2,5]thiadiazolo[3,4-*c*]pyridine and 3,4-ethylenedioxythiophene-tetraphenylethylene as the acceptor and donor, respectively, exhibited a high fluorescence quantum yield but suffered from a low extinction coefficient and negligible photosensitization. To overcome these limitations, isoindigo (IID) was introduced as a second acceptor, intensifying D–A conjugation and the ICT effect, which red-shifted absorption and doubled the extinction coefficient. However, IID-PSS exhibited marked fluorescence quenching, with the quantum yield falling below 1.4%. To further enhance SOC, sulfur was replaced with selenium, yielding IID-PSSe. This substitution narrowed the HOMO–LUMO gap and ΔE_{ST} , promoting ISC, elevating the $^1\text{O}_2$ yield to 15%, and achieving a PCE of 35%.

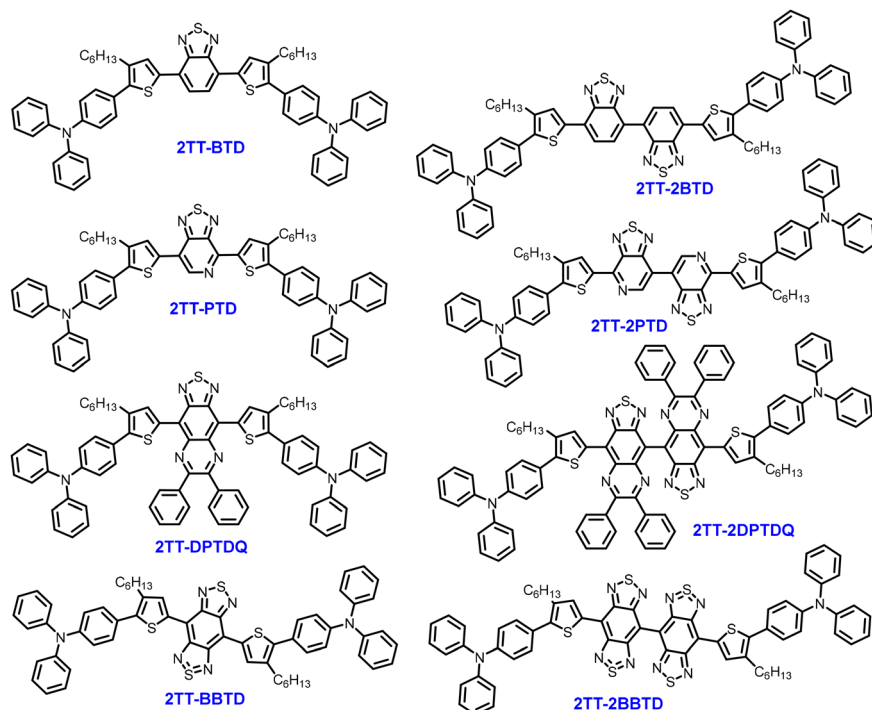


Fig. 43 AIEgens with single or dual-acceptor.



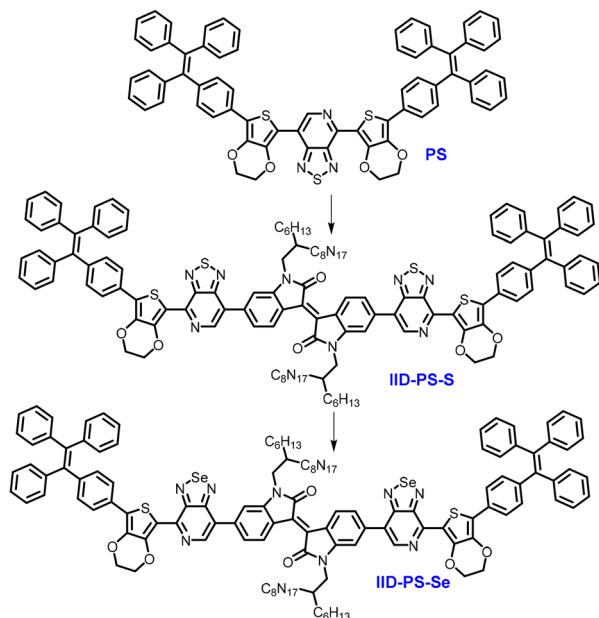


Fig. 44 Triple-acceptor architectures for phototherapy.

Although fluorescence declined to 0.6%, IID-PSSe maintained a high extinction coefficient and robust photothermal performance across cycles. Importantly, IID-PSSe nanoparticles demonstrated negligible dark toxicity yet induced potent tumor ablation upon irradiation, achieving strong therapeutic outcomes *in vitro* and *in vivo*.

Traditionally, the synthesis of dual-acceptor units such as dibromo-benzothiadiazole required multistep procedures and yielded low product quantities (<27%). To overcome this limitation, Tang's group¹³⁹ developed a one-step Suzuki coupling route for constructing both D-A-D (2DMeTPA-BT) and D-A-A-D (2DMeTPA-2BT) PSs, achieving a 47% yield for 2DMeTPA-2BT, the first reported instance of single-step dual-acceptor PS synthesis (Fig. 45). Structural characterization revealed large dihedral angles ($\sim 68^\circ$), a reduced ΔE_{ST} (0.265 eV), enhanced SOC (0.11 cm^{-1}), and a rapid ISC rate ($k_{ISC} \approx 3.41 \times 10^9 \text{ s}^{-1}$), collectively promoting long-lived triplet states and efficient type

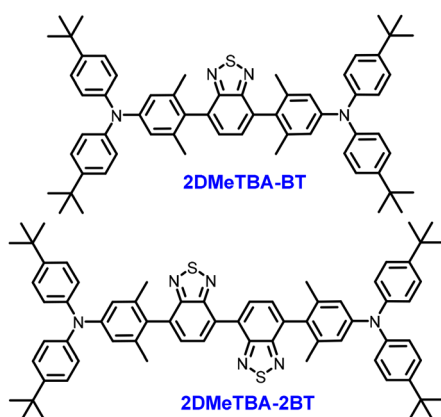


Fig. 45 Chemical structures of 2DMeTPA-BT and 2DMeTPA-2BT.

I/II ROS generation. Optical studies showed red-shifted absorption/emission peaks (636/713 nm) compared to the mono-acceptor counterpart, alongside solvent-dependent TICT behavior that conferred AIE characteristics in both aggregate and solid states (quantum yield: 25%). Nanoprecipitated 2DMeTPA-2BT nanoparticles exhibited a high ϵ ($1.17 \times 10^4 \text{ M}^{-1} \text{ cm}^{-1}$), strong photostability, and notably enhanced ROS output, with singlet oxygen yields reaching 1.42-fold those of RB. *In vivo*, these nanoparticles achieved approximately 90% tumor growth inhibition *via* synergistic type I/II PDT mechanisms.

AIE molecules are widely studied for fluorescence imaging and phototheranostics; however, their inherently twisted conformations often result in low molar extinction coefficients. Although dual-acceptor strategies developed by Tang and co-workers have enhanced light-harvesting capacity, AIE molecules continue to exhibit inferior absorption compared to conventional ACQ dyes. To address this, Li and colleagues¹⁴⁰ introduced a π -bridged dimerization strategy, in which monomeric AIE units (TPE-BTO and DTPE-BTO) were covalently linked *via* various π -spacers to yield a series of dimers (TPE-BTO-Dimer 1–6 and DTPE-BTO-Dimer 1–6; Fig. 46). This design considerably improved absorption (ϵ increased by 2.3–3.7-fold to $6.01\text{--}9.54 \times 10^4 \text{ M}^{-1} \text{ cm}^{-1}$) and induced marked redshifts in the absorption maxima. For instance, TPE-BTO-Dimer 1 exhibited a λ_{abs} of 500 nm and an ϵ of $8.61 \times 10^4 \text{ M}^{-1} \text{ cm}^{-1}$, compared to 449 nm and $2.69 \times 10^4 \text{ M}^{-1} \text{ cm}^{-1}$ for the monomer. DFT calculations showed that π -bridging planarized the molecular skeleton, yielding minimal dihedral angles ($0.1^\circ\text{--}2.7^\circ$) and promoting delocalization of both HOMO and LUMO orbitals across the π -framework. This conjugation enhancement endowed the dimers with high oscillator strengths and favorable charge-separation characteristics. Moreover, dimerization extended emission into the NIR region, making these systems strong candidates for photothermal cancer therapy.

Qin and co-workers¹³⁵ designed a D-A dimer wherein TPA-thiophene functioned as the donor and a benzothiadiazole derivative served as the acceptor. A large conjugated electron-withdrawing core (benzothiadiazole derivative) served as a bridge connecting two D-A segments within a single molecule, while peripheral alkyl chains introduced sufficient free volume for intramolecular rotor motion. This rational design endowed 4THTPB with notable photophysical and photothermal characteristics. Specifically, the twisted molecular conformation induced by the alkylthiophene units effectively suppressed aggregation-caused quenching, enabling a characteristic ICT absorption band at 696 nm in THF with a molar absorptivity of $2.46 \times 10^4 \text{ M}^{-1} \text{ cm}^{-1}$, which is 1.31-fold higher than that of the smaller-acceptor analogue TT1-oCB (793 nm). The fluorescence quantum yield of 4THTPB in THF was limited to 0.52% due to strong TICT and intramolecular rotations but increased to 3.2% in aqueous nanoparticles, confirming a typical AIE effect. These nanoparticles exhibited an ultrahigh PCE of 87.6%, surpassing many reported organic photothermal agents. This enabled deep-tissue NIR-II fluorescence imaging with penetration depths up to 840 μm , where capillaries as narrow as 3.4 μm were resolvable at 540 μm , and also supported precise photothermal thrombolysis.



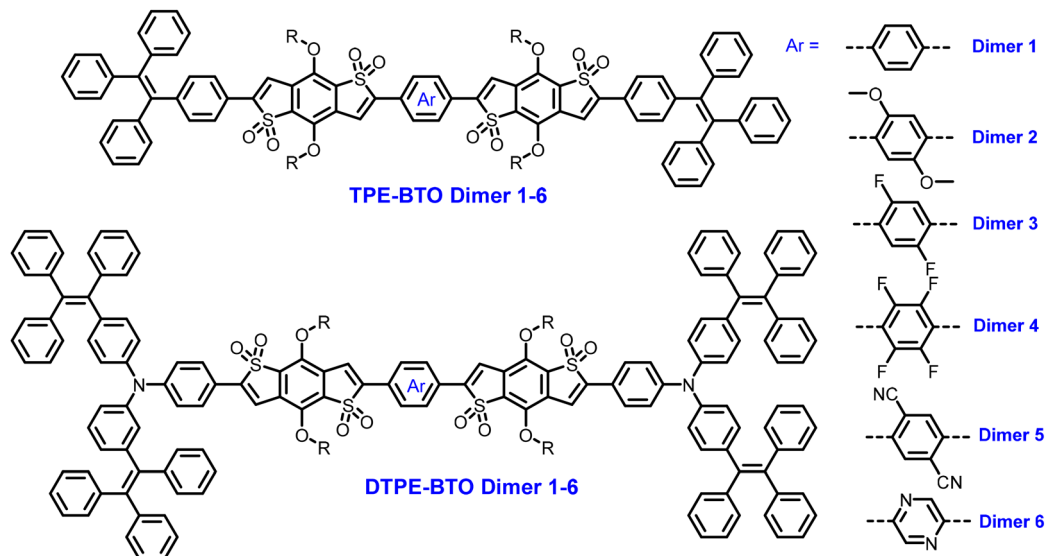


Fig. 46 π -Bridged dimerization strategy for phototheranostics.

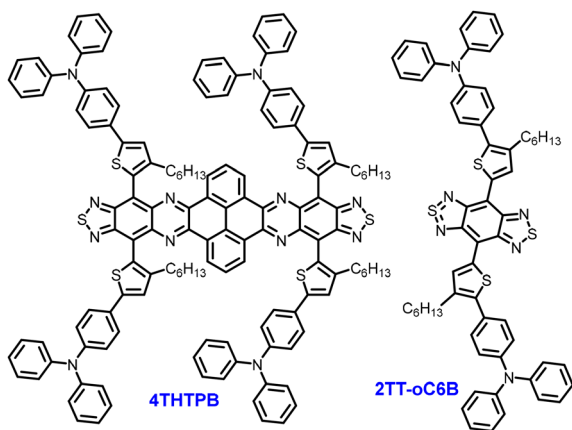


Fig. 47 D-A architectures incorporating benzothiadiazole cores.

In vivo studies further demonstrated that 4THTPB nanoparticles promoted vascular reconnection following treatment, underscoring their strong potential for simultaneous diagnosis and therapy of microvascular lesions (Fig. 47).

Tang *et al.*^{136,141} addressed the intrinsic limitations of conventional NIR-II luminogens, including poor stability, low synthetic yield, and limited therapeutic efficacy, by introducing a “strength in numbers” strategy based on N-heteroacenes (NHAs). As illustrated in Fig. 48, two acceptor skeletons, namely pyrene-fused phenazothiadiazoles (PPT, 5-ring) and pyrene-fused bisphenazothiadiazoles (PBPT, 8-ring), were incorporated into D-A-D frameworks to yield 2TT-PPT and 4TT-PBPT, respectively. Compared to 2TT-PPT (λ_{abs} 676 nm, λ_{em} 996 nm), 4TT-PBPT exhibited extended conjugation and stronger ICT, resulting in red-shifted absorption and emission (λ_{abs} 700 nm, λ_{em} 1026 nm with shoulder at 1270 nm) and a twofold increase in the molar extinction coefficient. The large Stokes shifts (> 300 nm) effectively suppressed self-absorption, a well-recognized limitation of cyanine

dyes. Photophysically, 4TT-PBPT NPs achieved a PCE of 73.8%, surpassing that of 2TT-PPT (67.3%) and 2TT-PBPT (53.0%). Upon 808 nm laser irradiation, tumor temperatures rose rapidly from 35.0 °C to 51.4 °C, supporting efficient PDT. In parallel, enhanced spin-orbit coupling and reduced energy gaps facilitated efficient ROS generation, thereby further improving PDT efficacy. The trimodal FLI/PAI/PTI imaging capability of 4TT-PBPT, coupled with its PDT/PTT synergy, enabled complete eradication of orthotopic bladder tumors in mice. Notably, no appreciable toxicity to normal tissues was observed, underscoring the system's excellent biosafety. Collectively, this study presents the first example of an AIEgen that concurrently integrates NIR-II brightness, a large Stokes shift, high PCE, robust ROS generation, and multimodal imaging-guided synergistic therapy, establishing a robust molecular design paradigm for overcoming the limitations of conventional NIR-II agents.

Open-shell π -conjugated molecules with intrinsic unpaired electrons are increasingly regarded as promising platforms for type-I PDT. To explore this potential, Tian *et al.*¹³⁷ systematically compared a closed-shell monomer (2AM-CS) and an extended dimer (4AM-OS) to examine how radical characteristics shape excited-state dynamics (Fig. 49). Although both systems exhibit nearly identical absorption maxima (793/795 nm in NPs) and NIR-II emission extending to 1400 nm, the dimer adopts a thermally accessible open-shell configuration that promotes broader radical delocalization and introduces additional electronic states. This feature leads to substantial reductions in $\Delta E_{S_1-T_3/T_1}$ (0.240/0.493 eV for 4AM-OS vs. 0.283/0.856 eV for 2AM-CS), thereby facilitating photo-induced charge transfer and enhancing type-I ROS generation ($\cdot\text{OH}$, $\text{O}_2^{\cdot-}$) alongside photocatalytic activity. These mechanistic advantages translate into markedly improved PDT efficacy, with IC_{50} values of 6.1/9.9 $\mu\text{g mL}^{-1}$ under normoxic/hypoxic conditions (vs. 33.2/51.2 $\mu\text{g mL}^{-1}$ for 2AM-CS), while both systems retain negligible dark toxicity. This study offers critical insights into the design of type-I PSs,



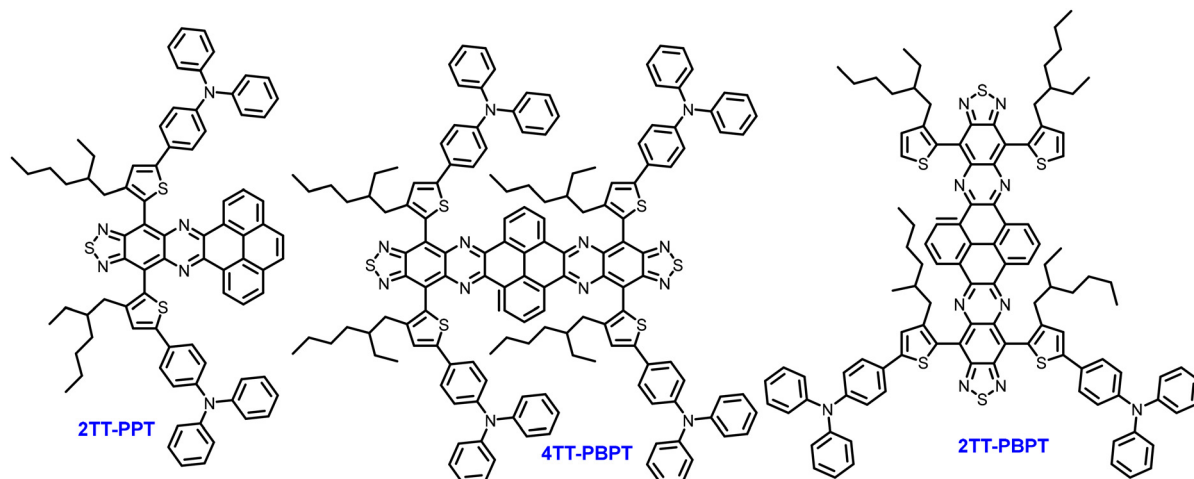


Fig. 48 Illustration of a "strength in numbers" strategy based on N-heteroacenes (NHAs) for constructing D-A-D dimers.

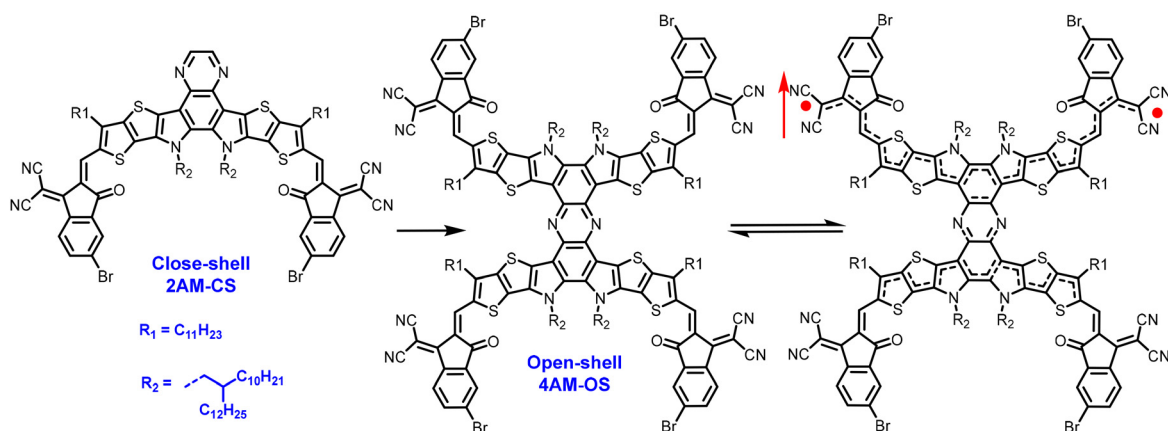


Fig. 49 Open-shell π -conjugated dimers.

though its applicability remains largely limited to fluorophores bearing functional motifs capable of stabilizing open-shell configurations. Broadening this strategy to encompass a wider range of chromophores remains an important challenge with the potential to substantially expand the chemical space for robust type-I PDT.

Although record-breaking PCEs continue to be reported, advancing clinical translation necessitates further enhancement of light-harvesting efficiency. To this end, Tian *et al.*¹³⁸ implemented an absorptivity-driven approach by dimerizing the high-PCE A-D-A monomer BTIC into single-bond- and vinyl-linked dimers, dB TIC-S and dB TIC-D, respectively. Upon dimerization (Fig. 50), only slight redshifts were observed in the absorption maxima. Even in the vinyl-linked variant, the extended π -conjugation failed to notably shift λ_{max} , suggesting that the introduction of a C=C bridge neither altered the intrinsic donor-acceptor strength nor promoted notable intermolecular energy-level coupling. Despite the minor spectral changes, both dimers exhibited considerable gains in molar absorptivity. In CHCl_3 , ϵ_{max} increased from 1.80×10^5 (BTIC) to 2.84×10^5 (dB TIC-S) and $2.25 \times 10^5 \text{ M}^{-1} \text{ cm}^{-1}$ (dB TIC-D). In aggregate form,

ϵ_{808} rose from 0.47×10^5 to 1.37×10^5 and $1.40 \times 10^5 \text{ M}^{-1} \text{ cm}^{-1}$, representing nearly three-fold enhancements relative to the monomer and surpassing the theoretical doubling. This trend is consistent with strengthened π - π electronic interactions and reorganized molecular packing. Notably, unlike many dimeric systems that suffer fluorescence quenching, both dimers exhibited increased Φ_{F} (0.8%, 1.5%, and 2.0% for BTIC, dB TIC-S, and dB TIC-D, respectively), with further enhancement observed in nanoparticle form, indicating a greater local excited-state character upon π -extension. All three systems maintained comparable PCEs (66.4%, 68.5%, and 61.4%), yet the substantially enhanced light absorption enabled dB TIC-D to achieve effective tumor ablation under low-power 808 nm laser irradiation (0.3 W cm^{-2}).

3.6 Supramolecular dimeric assemblies

Supramolecular chemistry, pioneered by the 1987 Nobel Laureates Cram, Lehn, and Pedersen, has advanced substantially over recent decades.¹⁴² In this context, supramolecular assemblies of PSs have emerged as compelling platforms for tumor phototherapy and related biomedical applications.¹⁴³⁻¹⁴⁵ Compared with single-molecule systems, supramolecular strategies offer



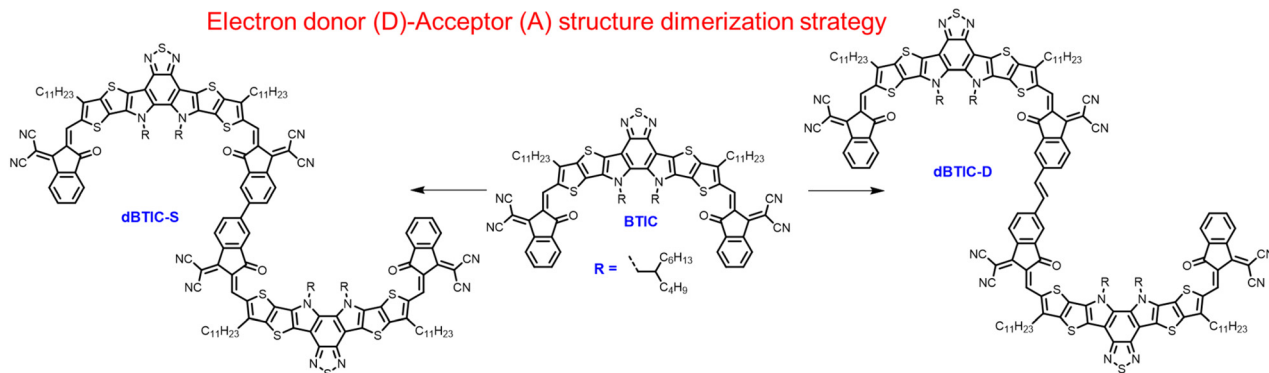


Fig. 50 Dimerization strategy for an A–D–A monomer.

improved water solubility, optimized photophysical behavior, enhanced cellular uptake, and increased tumor-targeting efficiency. In contrast to covalent dimerization, supramolecular self-assembly, driven by π - π stacking, van der Waals forces, hydrophobic interactions, hydrogen bonding, and host-guest recognition, provides a versatile approach for constructing dimeric or multimeric PS architectures.¹⁴⁴

Phthalocyanines, which are planar macrocyclic metal complexes, exhibit strong light absorption and high ROS and heat generation capacities, rendering them valuable agents for phototherapy. However, their inherent hydrophobicity limits clinical translation. To overcome this challenge, Yoon's group¹⁴⁶ developed a supramolecular dimerization approach based on cation-anion pairing (Fig. 51). Equimolar mixtures of oppositely charged Pc derivatives assembled into dimers, which subsequently aggregated into ~ 60 nm NPs. The ϵ of PcDA ($5.8 \times 10^4 \text{ M}^{-1} \text{ cm}^{-1}$) notably exceeded those of PcD ($4.0 \times 10^4 \text{ M}^{-1} \text{ cm}^{-1}$) and PcA ($3.1 \times 10^4 \text{ M}^{-1} \text{ cm}^{-1}$). Furthermore, intra-dimer FRET boosted both ROS and heat production. As a result, PcDA achieved superior photothermal efficiency (15.7%), substantially higher than that of PcD (3.7%) and PcA (3.1%). This pronounced photothermal effect also generated strong photoacoustic signals. *In vivo*, PcDA treatment (0.8 nmol g^{-1} , 300 J cm^{-2}) suppressed tumor growth by 95%, highlighting the therapeutic potential of supramolecularly engineered Pc assemblies.

Organic free radicals possess narrower band gaps than traditional π -conjugated dyes, facilitating red-shifted absorption. When intermolecular charge transfer occurs between radicals, the band gap narrows further, enabling absorption to extend into the NIR-II

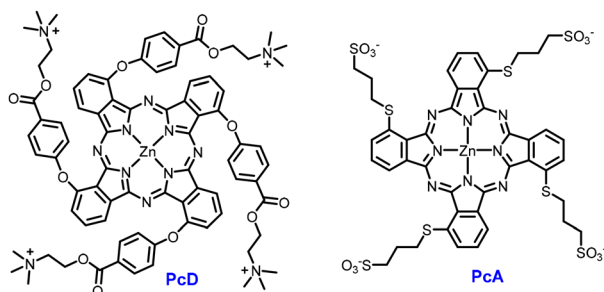


Fig. 51 Phthalocyanine dimers based on cation-anion pairing.

region. Rather than employing covalent dimerization, Zhang *et al.*¹⁴⁷ introduced a supramolecular assembly strategy to construct a supramolecular radical dimer (Fig. 52a). This dimer was formed by combining N,N' -dimethylated dipyrindinium thiazolo[5,4-*d*]thiazole (MPT²⁺) and cucurbit[8]uril (CB[8]), resulting in strong NIR-II absorption. Upon assembly, the two MPT²⁺ units adopt a parallel yet staggered conformation that facilitates intermolecular charge transfer. Under 405 nm irradiation in the presence of triethanolamine (TEOA) as an electron donor, photo-induced electron transfer from MPT²⁺ gradually generates MPT⁺ radicals, accompanied by distinct spectral evolution. During irradiation of 2MPT²⁺-CB[8], an initial reduction yielded species A, exhibiting absorption bands at 618 and 1308 nm. This intermediate then converted into species B, characterized by absorptions at 547 and 1004 nm. The molar absorption coefficient of species B at 1004 nm was determined to be $3.93 \times 10^4 \text{ M}^{-1} \text{ cm}^{-1}$. Notably, this transformation endowed the system with efficient NIR-II photothermal properties, achieving a PCE of 54.6%. Remarkably, even with a 5 mm chicken breast tissue barrier, the supramolecular radical dimer generated sufficient heat to ablate cancer cells effectively.

Jin *et al.*¹⁴⁸ designed a D- π -A structured molecule (SC-3) capable of forming a supramolecular dimer through host-guest assembly with CB[8] (Fig. 52b). The binding constant between

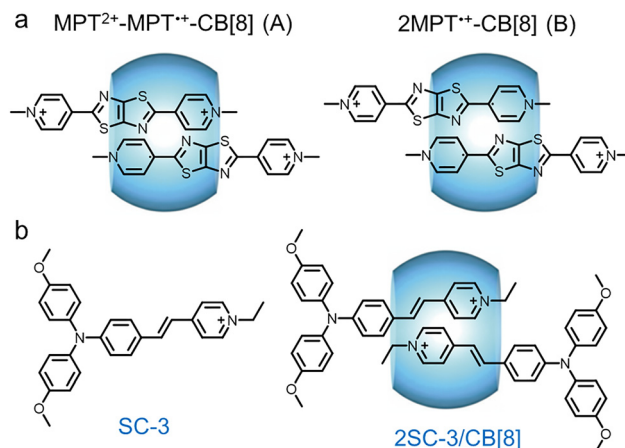


Fig. 52 Cucurbit[8]uril-mediated organic dimers.



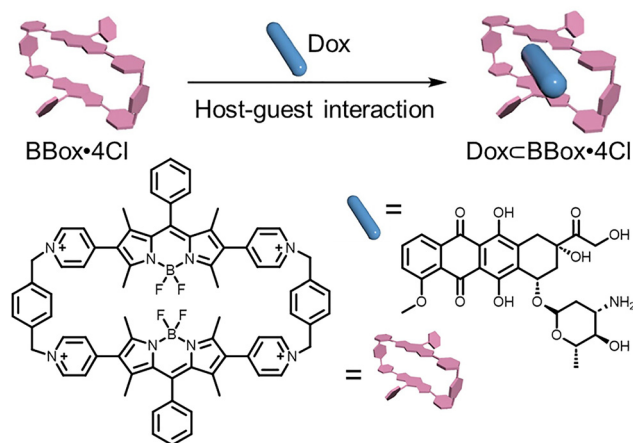


Fig. 53 Tetracationic BODIPY macrocycle integrated with doxorubicin via a host-guest interaction. Reproduced with permission.¹⁴⁹ Copy Right 2025 American Chemical Society.

SC-3 and CB[8] was measured as $1.39 \times 10^5 \text{ M}^{-1}$, confirming the successful formation of the supramolecular PS. Upon complexation, the resulting 2SC-3/CB[8] adopts a cage-like structure, wherein CB[8] offers a hydrophobic cavity, electrostatic shielding, and conformational restriction. These synergistic effects collectively suppress intramolecular motions and disordered aggregation while promoting π - π stacking and charge-transfer interactions, thereby enhancing intersystem crossing and triplet-state formation. Consequently, the dimeric PS displays a 1.35-fold increase in ROS generation efficiency compared with its monomeric form.

Liu *et al.*¹⁴⁹ constructed a supramolecular photoelectron “reservoir” (SPR) by assembling a tetracationic BODIPY macrocycle (BBox-4Cl), doxorubicin (Dox), and β -cyclodextrin-hyaluronic acid (HACD; Fig. 53). The resulting host-guest complex (Dox \subset BBox-4Cl) exhibited a high binding constant ($8.05 \times 10^5 \text{ M}^{-1}$) and further self-assembled into nanoparticles (Dox \subset BBox-4Cl@HACD). BBox-4Cl displayed broad absorption spanning 420–650 nm, with a dominant peak at 511 nm and emission between 541 and 547 nm. Strong π - π stacking interactions substantially reduced the fluorescence quantum yield from 34.15% in acetonitrile to 5.34% in water. Crucially, the supramolecular assembly markedly enhanced ROS production, achieving a singlet oxygen quantum yield of 160%, 2.1-fold higher than Rose Bengal (75%). Upon 660 nm irradiation, the excited triplet state $^3(\text{BBox})^*$ not only underwent energy transfer with O_2 to produce $^1\text{O}_2$ but also facilitated intramolecular disproportionation between two antiparallel BODIPY units, creating radical cations and anions. The radical anion (BODIPY) $^{\bullet-}$ efficiently transferred electrons to oxygen, yielding $\bullet\text{OH}$, while the radical cation (BODIPY) $^{\bullet+}$ was reduced by NADH, which was catalytically oxidized to NAD^+ ($k_{\text{obs}} = 0.187 \text{ min}^{-1}$). Dox embedded in the BODIPY cavity acted as an electron “pump” to mediate ICT, whereas HACD served as a “sponge” to concentrate assemblies and accelerate intermolecular transfer. Together, these components sustained photoelectron cycling and boosted ROS generation even under hypoxic conditions. This supramolecular design thus integrates favorable photophysical properties with

cascade-activated radical generation: efficient absorption in the visible range, high $^1\text{O}_2$ quantum yield, NADH-driven $\bullet\text{OH}$ production, and redox imbalance induction. Therefore, the system exhibited potent anticancer activity with IC_{50} values of 0.46 μM (normoxia) and 0.85 μM (hypoxia), with *in vivo* tumor inhibition rates reaching 95%, demonstrating its strong potential as a hypoxia-tolerant, type-I/II synergistic PDT platform.

In recent years, metal-based drugs have garnered growing interest within the biomedical field, and supramolecular coordination complexes (SCCs)—formed *via* coordination-driven self-assembly of PS ligands—have emerged as versatile platforms for constructing functional multimers. SCCs are discrete supramolecular entities with well-defined two- or three-dimensional architectures, in which metal centers or clusters coordinate with organic ligands in specific geometries.^{142,150} Within this domain, Sun and co-workers¹⁴² have made notable contributions, particularly in the development of SCCs with NIR-II emission for advanced biomedical applications. These complexes have been successfully employed in photodynamic therapy, PTT, and sonodynamic therapy, highlighting the versatility of metal-ligand coordination strategies. In such assemblies, pyridyl-functionalized BODIPY molecules and D-A-D-type ligands based on the BBD framework often serve as organic building blocks. Coordination between pyridine moieties and metal centers facilitates the formation of discrete dimers, trimers, or higher-order supramolecular architectures. These SCCs not only enhance the optical and photophysical properties of the constituent ligands but also enable precise spatial organization, offering new opportunities for synergistic multimodal cancer therapy.

Although SCCs offer notable advantages in PS design—for instance, metal coordination and rigid macrocyclic frameworks effectively separate PS units and suppress further aggregation, thereby enhancing ROS generation, while heavy atoms promote ISC to boost PDT efficiency, their potential toxicity presents notable biosafety concerns. To mitigate this issue, Sun’s group¹⁵¹ developed a series of aza-BDP ligands (Fig. 54) with varying electron-donating capacities and assembled them with Ru(II) complexes to construct metallacycle-based supramolecular PSs. These assemblies were conveniently obtained by mixing ligands with Ru complexes in a 1:1 ratio in methanol/chloroform at room temperature, yielding discrete metallacycles featuring three broad absorption bands (approximately 630, 740, and 850 nm) and strong NIR-II emission (1105–1115 nm), closely resembling that of the aza-BDP ligand. Theoretical calculations suggested that increased ligand distortion could enhance intramolecular CT and ROS generation, while steric hindrance inhibited π - π stacking, thereby reducing ROS quenching. Among these, RuD exhibited the lowest ΔE_{ST} (0.61 eV), facilitating efficient ISC and yielding superior ROS generation, including both singlet oxygen and superoxide anion. Importantly, RuD showed negligible dark toxicity ($\text{IC}_{50} > 700 \mu\text{M}$ in A549 cells) attributed to its bulky, electron-rich acceptor that minimized ligand exchange with biomolecules, unlike RuA, which showed higher dark toxicity. Upon laser irradiation, RuD delivered the strongest PDT performance ($\text{IC}_{50} = 1.8 \mu\text{M}$),



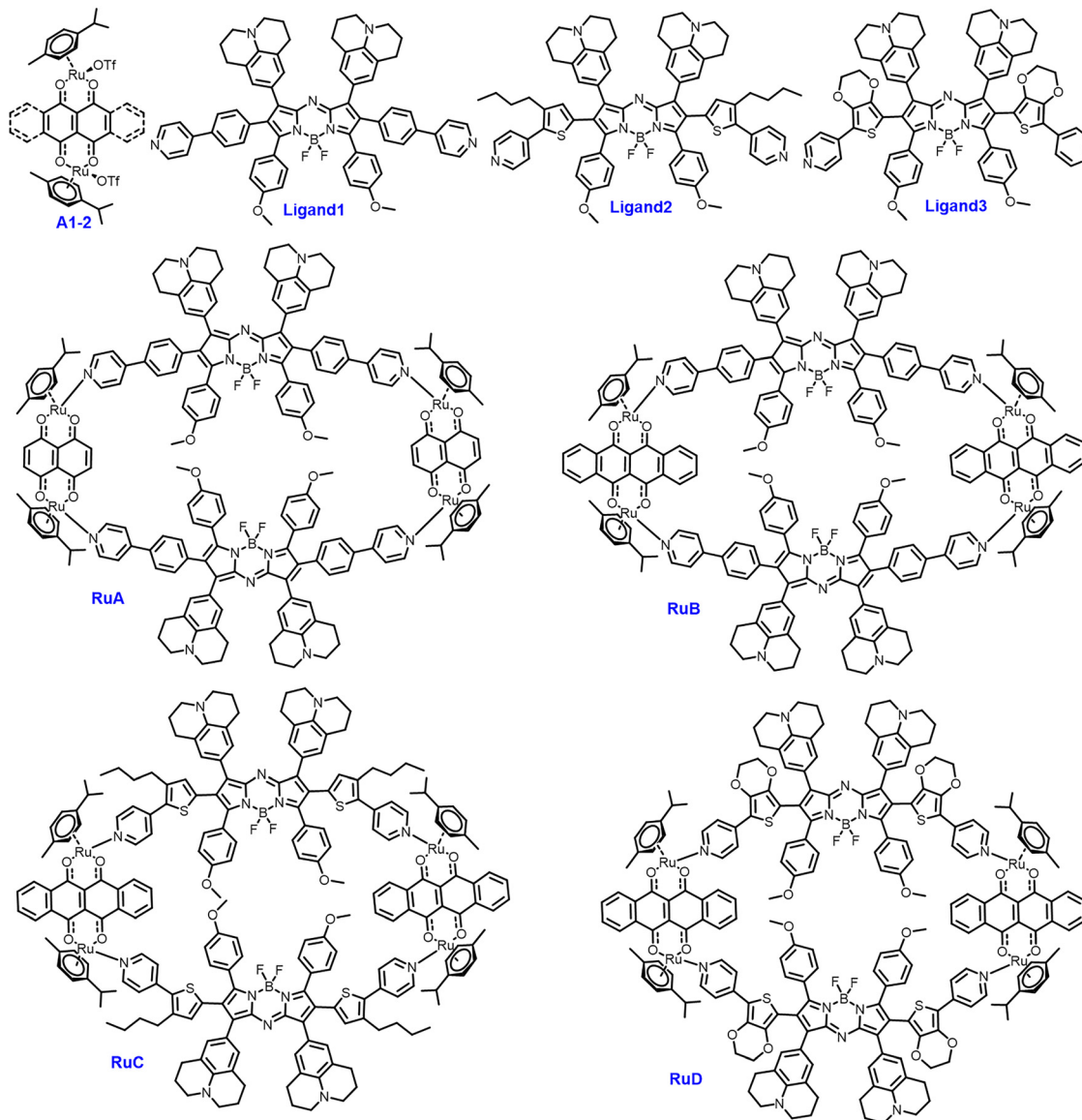


Fig. 54 Representative structural architectures of supramolecular coordination complexes.

consistent with its highest ROS productivity, and achieved an exceptional phototoxicity index of 406.5.

In addition to modulating the donor properties of aza-BDP ligands, Sun and co-workers¹⁵² implemented a π -expansion strategy on Ru(II) acceptors to construct a new series of metallacycles. This structural refinement not only reduced dark toxicity but also substantially enhanced phototoxicity, achieving a high phototoxicity index (~ 146). Notably, these compounds sustained strong PDT performance even under adverse conditions, exhibiting pronounced anti-tumor activity in deep tissue (~ 7 mm) and hypoxic environments. These findings underscore the effectiveness of π -expanded Ru(II) acceptors in simultaneously optimizing biosafety and therapeutic efficacy, thereby broadening the clinical applicability of metallacycle-based supramolecular PSS. Collectively, this study highlights how rational modulation of ligand electronics and steric environment in Ru-based SCCs can finely

tune the balance between biocompatibility and therapeutic performance.

SCCs have demonstrated considerable promise for anti-tumor PDT, antimicrobial PDT, and photoimmunotherapy. However, despite the deeper tissue penetration afforded by NIR-II light, treating deeply seated pathologies remains a notable challenge. To address this limitation, Sun and co-workers¹⁵³ designed ultrasound-activatable SCCs for the prevention of ventricular arrhythmias (VAs) following myocardial infarction. In this system, a modified aza-BODIPY dye (IR1105), incorporating a 180° dipyrroline ligand to enable long-wavelength emission, was coordinated with Ru(II) complexes featuring varying conjugation planes to generate metallacycles RuE and RuF (Fig. 55). Compared with IR1105, clinical dye ICG, and RuA, RuB exhibited superior ROS generation, achieving a Φ_{Δ} of 0.88 under ultrasound activation (*vs.* 0.70 for RuA and 0.25 for IR1105). This



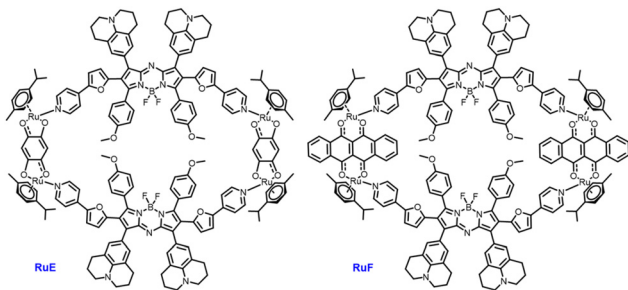


Fig. 55 SCCs with NIR-II properties.

enhanced performance was attributed to its larger π -conjugated framework and smaller ΔE_{ST} (0.54 eV vs. 0.90 eV for RuA). RuB efficiently generated ROS at low concentrations and under mild ultrasound conditions, thereby promoting pro-survival autophagy in microglial cells. *In vivo*, RuB-mediated ultrasound activation effectively attenuated sympathetic overactivity and inflammation, ultimately mitigating VAs.

4. *In situ* dimerization via CBT–Cys click chemistry

Pre-formed dimers generated through covalent bonding or supramolecular association constitute a direct “pre-activation” strategy, in which the functional state of the molecule remains permanently switched on following administration. Although such dimers can improve photophysical performance, their continuous activity during systemic circulation raises concerns about off-target effects and overall toxicity. Despite the inherently high spatiotemporal precision of phototherapy, pre-formed dimers often fail to achieve adequate tumor or lesion-specific activation, thereby limiting their clinical translational potential.

In 2009, Rao *et al.*¹⁵⁴ introduced a bioorthogonal CBT click reaction between 1,2-aminothiol and 2-cyanobenzothiazole (Fig. 56), which proceeds under specific physiological triggers, including pH variation, disulfide bond reduction, or enzymatic cleavage, both *in vitro* and in living systems. Remarkably, the resulting condensation products displayed distinct sizes, morphologies, and self-assembly profiles depending on monomer structure, allowing precise modulation of nanostructure formation. This concept enables the *in situ* construction of dye dimers: by incorporating responsive groups into the monomer backbone, dimerization can be selectively triggered by tumor-associated biomarkers. The resulting dimers may further engage in hierarchical self-assembly, promoting extended retention and improved lesion visualization. In addition, dimerization inherently strengthens intermolecular interactions such as energy transfer and charge transfer, thereby amplifying multimodal outputs, including

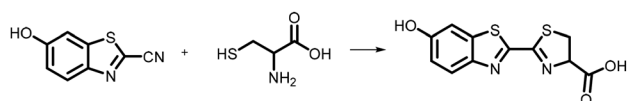


Fig. 56 CBT click chemistry.

fluorescence, photoacoustic signals, ROS generation, and photo-thermal effects, for precise diagnosis and therapy.

Building upon the CBT click chemistry strategy, Liang and co-workers developed a series of enzyme-activatable systems for disease detection and therapy, targeting biomarkers such as alkaline phosphatase, Granzyme B, and cathepsin B (CTSB).^{155–158} For example, CTSB, a lysosomal protease overexpressed in the early stages of many cancers, represents a valuable target for sensitive diagnosis. Liang and colleagues¹⁵⁹ designed a “smart” near-infrared photoacoustic probe, Cypate-CBT, wherein design principle and biological function were intimately interwoven (Fig. 57a). The key concept centered on leveraging enzyme-triggered self-assembly to convert fluorescence quenching into photoacoustic signal amplification: following intracellular glutathione-mediated reduction and CTSB cleavage, the probe underwent a CBT–Cys click reaction to form Cypate dimers, which spontaneously self-assembled into nanoparticles. This aggregation induced the formation of H-aggregates, suppressing fluorescence while promoting nonradiative decay, thereby notably enhancing photoacoustic output. Experimental validation confirmed this mechanism. Cypate-CBT exhibited pronounced intracellular accumulation and a 4.7–4.9-fold increase in photoacoustic intensity within CTSB-overexpressing MDA-MB-231 cells and xenografted tumors relative to unmodified Cypate. Furthermore, the probe’s PA response demonstrated a linear correlation with CTSB concentration (LOD = 0.095 U mL⁻¹), underscoring its high sensitivity and selectivity. By unifying enzyme-responsive dimerization, self-assembly, and signal transduction within a single platform, this work exemplifies how rational molecular design can enable tumor-selective activation and high-contrast imaging with clinical potential.

AD remains one of the most devastating neurodegenerative disorders, with chronic neuroinflammation playing a pivotal role in accelerating neuronal degeneration and cognitive decline. Among the inflammatory mediators, caspase-1 (Cas1) has emerged as a critical executor of pyroptosis, linking inflammatory activation to neuronal injury. The ability to visualize Cas1 activity with high sensitivity and specificity would thus offer valuable mechanistic insight into AD pathogenesis while enabling early diagnosis. To this end, Liang *et al.*¹⁶⁰ developed a Cas1-activatable molecular probe comprising a Val–Cit peptide substrate tethered to a CBT moiety. As illustrated in Fig. 57b, upon cleavage by Cas1, the newly exposed cysteine thiol undergoes a bioorthogonal CBT–Cys condensation reaction to yield a covalently linked dimer. These dimers spontaneously self-assemble into nanoscale aggregates, producing a two-tiered restriction mechanism: first *via* covalent dimerization, and subsequently *via* supramolecular nanoparticle formation. This hierarchical assembly substantially amplifies aggregation-induced emission, yielding a markedly stronger fluorescence signal than that of nonassembling analogues. Experimental validation confirmed the efficacy of this molecular strategy. The Cas1-triggered assembly generated nanoparticles with diameters of approximately 80–120 nm, as revealed by TEM imaging. Fluorescence measurements showed a nearly 6-fold enhancement in emission intensity compared to controls lacking the CBT condensation



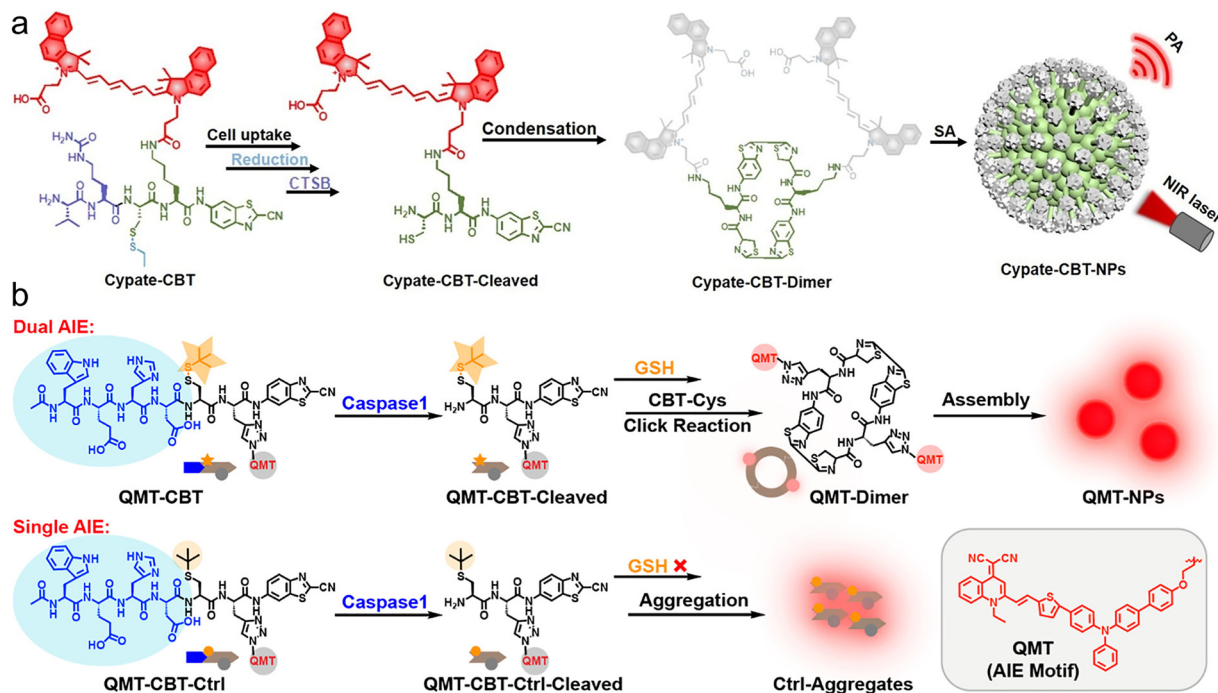


Fig. 57 (a) Diagram illustrating the CTSB-responsive assembly of Cypate-CBT nanoparticles for photoacoustic detection of CTSB activity both *in vitro* and *in vivo*. Reproduced with permission.¹⁵⁹ Copy Right 2021 Wiley-VCH GmbH. (b) Conceptual depiction of Cas1-induced dual aggregation of QMT-CBT, in contrast to the control probe QMT-CBT-Ctrl, which undergoes only a single aggregation pathway. Reproduced with permission.¹⁶⁰ Copy Right 2023 American Chemical Society.

motif, demonstrating that structural reorganization directly translates into signal amplification. Notably, in cellular studies employing AD-relevant inflammatory models, the probe sensitively visualized Cas1 activity, yielding bright intracellular fluorescence localized to regions of pyroptotic activation. *In vivo*, administration of the probe to AD mouse models resulted in intense fluorescence within inflamed brain regions, enabling real-time tracking of Cas1 activity throughout disease progression. This study not only provides a robust molecular tool for visualizing Cas1 activity in AD, but also establishes a generalizable design strategy in which enzymatic activation drives supra-molecular self-assembly to amplify diagnostic signals.

Building on this concept, Liang's group¹⁶¹ developed a tandem-targeting AIEgen for cancer imaging (Fig. 58a). The activatable probe β -*t*Bu-Ala-Cys(StBu)-Lys(Biotin)-Pra(QMT)-CBT (Ala-Biotin-QMT) integrates a biotin moiety to engage overexpressed biotin receptors and a β -*t*Bu-Ala substrate for leucine aminopeptidase (LAP), ensuring selective uptake and activation within tumor cells. Upon intracellular processing, the probe undergoes fluorescence turn-on, resulting in enhanced tumor accumulation and signal output. In living HepG2 cells and HepG2 tumor-bearing mice, Ala-Biotin-QMT exhibited 4.8-fold and 7.9-fold increases in NIR fluorescence, respectively, compared to controls pretreated with biotin or LAP inhibitors.

The self-assembly of small organic photothermal agents presents a powerful strategy to simultaneously modulate fluorescence and heat-generation properties. In the aggregated state, fluorophores typically undergo self-quenching, which suppresses

fluorescence emission and redirects absorbed energy toward nonradiative decay, thereby improving photothermal conversion efficiency. Leveraging this principle, Liang *et al.*¹⁶² developed a tumor-targeting PTA, Biotin-Cystamine-Cys-Lys(Cypate)-CBT (1), designed to undergo intracellular activation and achieve concurrent intra- and intermolecular fluorescence quenching, resulting in enhanced photothermal performance (Fig. 58b). Following biotin receptor-mediated internalization, compound 1 is reduced by intracellular GSH, producing a reactive intermediate (1-Red). This intermediate then undergoes CBT-Cys click condensation to form a cyclized dimer (1-Dimer), which engages in intramolecular quenching. The resulting dimers further self-assemble into nanoparticles (1-NPs), introducing an additional level of intermolecular quenching and yielding a dual-quenching effect. Fluorescence measurements confirmed this mechanism: 1-NP formation led to a 93.3% reduction in absolute fluorescence quantum yield, while 1-Dimer alone produced a 32.6% decrease. DFT calculations attributed this quenching to intramolecular FRET and intermolecular CT, validating the proposed nonradiative singlet energy decay pathways. This dual-quenching strategy considerably amplified photothermal performance. Upon 808 nm laser irradiation, 1-NPs achieved a PCE of $36.6 \pm 2.1\%$, 2.77-fold higher than that of the unassembled molecule and superior to comparable compounds. As a result, 1-NPs exhibited potent cytotoxicity against HeLa cells ($IC_{50} = 7.9 \pm 1.4 \mu M$) and induced complete tumor ablation following laser exposure. This work highlights how rationally engineered PTAs that exploit simultaneous intra- and intermolecular quenching can markedly enhance photothermal efficiency and therapeutic stability.



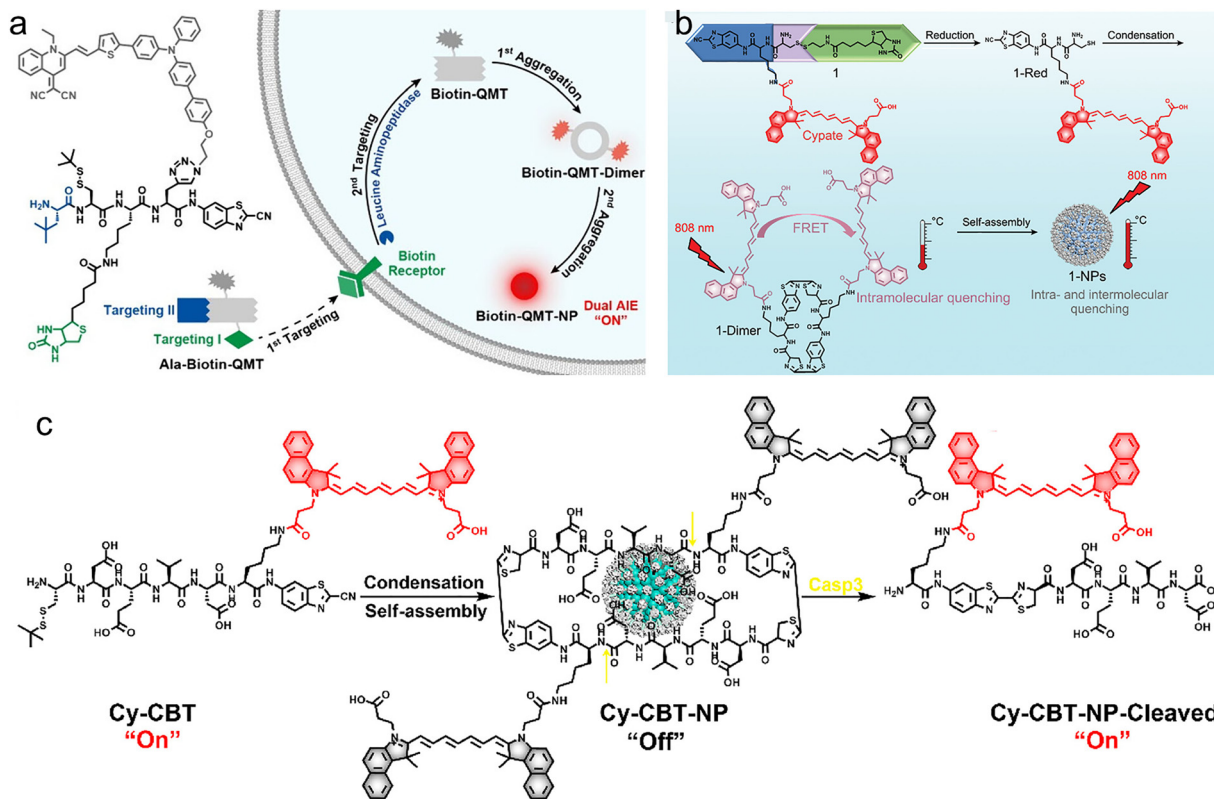


Fig. 58 (a) Schematic of the sequential tumor-targeting strategy and dual-assembly behavior of Ala-Biotin-QMT, enabling precise localization and amplified NIR fluorescence imaging of malignant tissues. Reproduced with permission.¹⁶¹ Copy Right 2024 American Chemical Society. (b) Illustration of the reductive transformation of compound 1 into its dimeric form (1-Dimer), which undergoes intramolecular fluorescence quenching. The dimer further self-organizes into 1-NPs, where additional intra/intermolecular quenching enhances the photothermal efficiency of the Cypate fluorophore. Reproduced with permission.¹⁶² Copy Right 2019 WILEY-VCH Verlag GmbH & Co. KGaA, Weinheim. (c) Diagram of the reduction-triggered condensation of Cy-CBT into nanoassemblies (Cy-CBT-NP), followed by Caspase-3-mediated cleavage that activates fluorescence. Reproduced with permission.¹⁶³ Copy Right 2020 American Chemical Society.

Precise control and real-time monitoring of PTT are essential for maximizing tumor ablation while minimizing collateral damage to surrounding healthy tissues. To address this challenge, Liang *et al.*¹⁶³ developed an intelligent near-infrared nanoparticle, Cy-CBT-NP, capable of self-assessing its therapeutic efficacy *via* a Caspase-3-responsive "off-on" fluorescence mechanism (Fig. 58c). This system incorporates a Casp3-cleavable DEVD peptide sequence into a dimeric precursor, Cys(StBu)-Asp-Glu-Val-Asp-Lys(Cypate)-CBT (Cy-CBT). Upon intracellular reduction of the disulfide bond, Cy-CBT undergoes CBT-Cys click condensation to form a cyclized dimer (Cy-CBT-Dimer), which subsequently self-assembles into NPs with quenched fluorescence. During PTT-induced apoptosis, activated Casp3 cleaves the DEVD sequence, triggering the formation of Cy-CBT-NP-Cleaved and restoring near-infrared fluorescence. This turn-on signal quantitatively correlates with apoptosis levels, enabling real-time evaluation of therapeutic outcomes. Cy-CBT-NPs display uniform morphology (~ 113 nm diameter, hydrated diameter ~ 246 nm), high stability in physiological environments, and strong specificity toward Casp3. Upon 808 nm laser irradiation, the nanoparticles exhibit efficient photothermal conversion ($\eta = 28.6\%$) and induce notable apoptosis in HeLa cells ($IC_{50} = 24.4 \pm 7.0$ μ M). Fluorescence imaging revealed a gradual NIR signal increase in irradiated

cells, directly corresponding to Casp3 activation. In HeLa tumor-bearing mice, the self-evaluation function was further validated: tumors treated with mild (44 $^{\circ}$ C) or severe (49 $^{\circ}$ C) PTT exhibited temperature-dependent fluorescence signals, with a 1.52-fold higher intensity in more severely apoptotic tissues. Histological staining and Casp3 immunolabeling confirmed that fluorescence intensity accurately reflected apoptotic activity.

5. Conclusions and perspectives

The dimerization of fluorophores has established a transformative design paradigm in tumor phototheranostics. Beyond its capacity to finely modulate photophysical properties, regulating excited-state dynamics to steer energy flow toward either photothermal or photodynamic pathways, this strategy profoundly reshapes key biophysical attributes, including hydrophobicity, conformational flexibility, and structural rigidity. These tailored modifications promote spontaneous self-assembly into well-defined nanostructures, thereby extending systemic circulation, enhancing tumor targeting, and improving cellular uptake efficiency. In this comprehensive review, we have systematically delineated the mechanistic roles of molecular dimerization as a



strategic modality in phototheranostics, emphasizing its dual functionality in optimizing both optical performance and biophysical behavior. We have also categorized a broad spectrum of small-molecule dimeric systems, including BODIPY dimers, cyanine dyes, porphyrins, phthalocyanines, donor-acceptor-type molecules, cyclometalated complexes, and supramolecularly assembled dimers, and critically evaluated their diverse applications in disease diagnosis, PTT, and PDT.

Despite the maturity of dimerization as a strategy for optimizing molecular performance, several challenges related to pharmacokinetics, metabolism, and safety remain unresolved. In particular, the clearance pathways, long-term retention, and potential off-target accumulation of dimeric systems require careful re-evaluation. Dimerization inherently increases molecular weight, rigidity, and hydrophobicity, often at the expense of aqueous solubility, which makes dimers more prone to aggregation. Consequently, dimeric fluorophores may exhibit pharmacokinetic behaviours that differ substantially from those of low-molecular-weight small-molecule dyes, which are generally favoured for their good biocompatibility and well-defined metabolic pathways. To address poor solubility, many dimeric systems are formulated into nanoparticles. While nanostructuring can improve solubility and circulation, it may also introduce drawbacks associated with nanomaterials, including complex metabolism and uncertain clearance, thereby shifting pharmacokinetic control from the molecular level to the nanoscale. Therefore, rational regulation of dimer pharmacokinetics is essential to fully exploit their advantages in tumor targeting and long-term retention. Future molecular design strategies can focus on enhancing intrinsic water solubility, reducing dimer size, regulating self-assembly behaviour, and developing carrier-free delivery systems.

Another major challenge lies in the environmental sensitivity of dimer performance, which poses constraints on clinical translation. Many BODIPY dimers that rely on SBCT or SOCT mechanisms exhibit a pronounced dependence on microenvironmental conditions. In particular, polar environments are essential for stabilizing the charge-separated states that underlie efficient reactive oxygen species generation in these systems. As such, the development of environmentally robust phototheranostic agents that maintain functionality across diverse biological settings remains a vital direction for future research.

Third, targeting specificity remains insufficient: most currently reported molecular systems are pre-designed without intrinsic affinity for pathological sites, raising the risk of off-target accumulation and related side effects. The “lesion-activated *in situ* self-assembly” strategy proposed by Liang *et al.* offers a compelling alternative, suggesting that dimers engineered to undergo selective activation at disease sites, particularly those formed *in situ*, could markedly enhance targeting precision while minimizing systemic toxicity.

Fourth, limited tissue penetration depth presents a persistent barrier to clinical translation. Existing phototheranostic agents primarily operate within the visible and first near-infrared windows, whose restricted penetration confines their utility to superficial tumors. Overcoming this limitation will require a multipronged strategy. One promising avenue is the

development of agents excitable in the second near-infrared window, which theoretically affords deeper tissue penetration. However, these systems face a fundamental trade-off: their narrow bandgaps facilitate rapid nonradiative decay, complicating the controlled distribution of excited-state energy and impeding efficient triplet-state formation. Alternative activation modalities that circumvent optical limitations, such as X-ray irradiation and ultrasound activation, offer attractive solutions for treating deep-seated lesions. In parallel, advanced delivery technologies, including endoscopic platforms for gastrointestinal tumors and implantable fiber-optic systems, can physically bridge the gap between external energy sources and internal pathological targets. The integration of these complementary strategies, uniting novel activation mechanisms with innovative delivery tools, will be essential to extend the reach of phototheranostics beyond current depth constraints.

Finally, artificial intelligence is reshaping phototheranostic design. Beyond image processing and drug discovery, AI is now entering the rational design of fluorescent probes and therapeutic agents. This shift is timely, as many phototheranostic systems already have well-defined parameters, such as absorption and emission wavelengths, singlet oxygen quantum yields, and photothermal conversion efficiencies. Recently, Peng *et al.*¹⁶⁴ developed independent regression-based machine learning models to predict singlet oxygen and fluorescence quantum yields, and constructed a virtual library of 2835 structurally diverse cyanine-based PSs using modular decomposition and algorithmic assembly, with synthetic accessibility and similarity filters to ensure feasibility. These advances suggest that AI can be further extended to predict intersystem crossing efficiency, optimize linker geometry, and screen dimer architectures. With systematic data curation and structured databases, such approaches can reveal hidden structure–property relationships, enable multi-parameter optimization, and accelerate the development of next-generation phototheranostics, marking a shift toward predictive and precision-guided molecular engineering.

By systematically addressing these challenges and strategically incorporating emerging technologies, dimerization-based platforms are poised to redefine the standards of phototheranostics, bridging the divide between laboratory innovation and clinical translation while advancing therapeutic precision and diagnostic fidelity.

Conflicts of interest

There are no conflicts to declare.

Abbreviations

AD	Alzheimer's disease
ACQ	Aggregation-caused quenching
AI	Artificial intelligence
AIE	Aggregation-induced emission
AIEgens	Aggregation-induced emission luminogens
BODIPY	Boron-dipyrromethene
Cas1	Caspase-1



CBT	2-Cyanobenzothiazole
CR	Charge recombination
CTSB	Cathepsin B
D–A	Donor–acceptor
DFT	Density functional theory
DMSO	Dimethyl sulfoxide
Dox	Doxorubicin
DPP	Diketopyrrolopyrrole
EPR	Enhanced permeability and retention effect
FDA	Food and Drug Administration
HOMO	The highest occupied molecular orbital
<i>H. pylori</i>	<i>Helicobacter pylori</i>
IC	Internal conversion
IC ₅₀	Half maximal inhibitory concentration
ICG	Indocyanine green
IID	Isoindigo
ISC	Intersystem crossing
LAP	Leucine aminopeptidase
LE	Local excited
LUMO	The lowest unoccupied molecular orbital
NAC	<i>N</i> -Acetylcysteine
NIR	Near-infrared
NPs	Nanoparticles
PBS	Phosphate-buffered saline
PCE	Photothermal conversion efficiency
PDT	Photodynamic therapy
PET	Photoinduced electron transfer
PSs	Photosensitizers
PTT	Photothermal therapy
PXZ	Phenoxazine
RET	Resonance energy transfer
ROS	Reactive oxygen species
RP-ISC	Radical-pair intersystem crossing
SBCT	Symmetry-breaking charge transfer
SCCs	Supramolecular coordination complexes
SOCT	Spin–orbit charge transfer
SV-ISC	Spin–vibronic coupling
TICT	Twisted intramolecular charge transfer
TPA	Triphenylamine
2PA	Two-photon absorption
Vas	Ventricular arrhythmias
VR	Vibrational relaxation
ZnPc	Zinc(II)phthalocyanine
Φ_F	Fluorescence quantum yield
Φ_Δ	Singlet oxygen quantum yield

Data availability

No primary research results, software or code have been included and no new data were generated or analysed as part of this review.

Acknowledgements

This research was supported by the Nano & Material Technology Development Program through the National Research

Foundation of Korea (NRF) funded by Ministry of Science and ICT (RS-2024-00407093, J. Y.) and Basic Science Research Program through the National Research Foundation of Korea (NRF), funded by the Ministry of Education (NRF-RS-2018-NR031064, M. H. K.). The authors also acknowledge the financial support from the National Natural Science Foundation of China (no. 22525803, 22090010, 22408233), China Postdoctoral Science Foundation (no. 2024M752118), the Young Scientists Fund of the National Natural Science Foundation of China (no. 22408232), Guangdong Basic and Applied Basic Research Foundation (grant no. 2025A1515012197), Shenzhen Science and Technology Program (grant no. JCYJ20250604181343059), Scientific Foundation for Youth Scholars of Shenzhen University (grant no. 000001032410).

References

- 1 Y.-Y. Zhao, S. Lee, Y. Lee, B. Hwang, H. Jung, Q. Hu, G. Song, H. Kang and J. Yoon, *Mater. Today*, 2025, **88**, 705–729.
- 2 T. C. Pham, V. N. Nguyen, Y. Choi, S. Lee and J. Yoon, *Chem. Rev.*, 2021, **121**, 13454–13619.
- 3 H. Xu, H. Hong, C. Kim, Y. Lee, Y. Li, Y. S. Zhang, P. Makvandi, G. Song, H. Zhang, H. Kang and J. Yoon, *Chem. Rev.*, 2025, **125**, 11461–11523.
- 4 W. Hu, P. N. Prasad and W. Huang, *Acc. Chem. Res.*, 2021, **54**, 697–706.
- 5 T. Zhang, X. Qu, J. Shao and X. Dong, *Chem. Soc. Rev.*, 2025, **54**, 8406–8433.
- 6 J. Zhao, K. Xu, W. Yang, Z. Wang and F. Zhong, *Chem. Soc. Rev.*, 2015, **44**, 8904–8939.
- 7 X. Zhao, J. Du, W. Sun, J. Fan and X. Peng, *Acc. Chem. Res.*, 2024, **57**, 2582–2593.
- 8 G. Feng, G. Q. Zhang and D. Ding, *Chem. Soc. Rev.*, 2020, **49**, 8179–8234.
- 9 M. Li, J. Xiong, Y. Zhang, L. Yu, L. Yue, C. Yoon, Y. Kim, Y. Zhou, X. Chen, Y. Xu, X. Peng and J. S. Kim, *Chem. Soc. Rev.*, 2025, **54**, 7025–7057.
- 10 A. Sharma, P. Verwilst, M. Li, D. Ma, N. Singh, J. Yoo, Y. Kim, Y. Yang, J.-H. Zhu, H. Huang, X.-L. Hu, X.-P. He, L. Zeng, T. D. James, X. Peng, J. L. Sessler and J. S. Kim, *Chem. Rev.*, 2024, **124**, 2699–2804.
- 11 Y. Y. Zhao, L. Lu, H. Jeong, H. Kim, X. Li, H. Zhang and J. Yoon, *Chem. Soc. Rev.*, 2025, **54**, 7749–7768.
- 12 S. Nandanwar, V. K. T. Nguyen, D. L. Tran, T. C. Pham and S. Lee, *Coord. Chem. Rev.*, 2026, **548**, 217165.
- 13 L. Wu, J. Liu, P. Li, B. Tang and T. D. James, *Chem. Soc. Rev.*, 2021, **50**, 702–734.
- 14 H. Bian, D. Ma, X. Zhang, K. Xin, Y. Yang, X. Peng and Y. Xiao, *Small*, 2021, **17**, e2100398.
- 15 H. Bian, D. Ma, Y. Nan, M. H. Kim, S. Kim, X. Chen, X. Peng and J. Yoon, *Coord. Chem. Rev.*, 2025, **534**, 216551.
- 16 H. Bian, D. Ma, F. Pan, X. Zhang, K. Xin, X. Zhang, Y. Yang, X. Peng and Y. Xiao, *J. Am. Chem. Soc.*, 2022, **144**, 22562–22573.



- 17 X. Ma, Y. Huang, S. A. A. Abedi, H. Kim, T. T. B. Davin, X. Liu, W.-C. Yang, Y. Sun, S. H. Liu, J. Yin, J. Yoon and G.-F. Yang, *CCS Chem.*, 2022, **4**, 1961–1976.
- 18 H. Bian, D. Ma, X. Zhang, Y. Qiu, X. Wu, M. Jia, X. Zhang, X. Liu, Y. Yang, X. Peng, J. Yoon and Y. Xiao, *J. Am. Chem. Soc.*, 2025, **147**, 39936–39952.
- 19 D. Ma, H. Bian, M. Gu, L. Wang, X. Chen and X. Peng, *Coord. Chem. Rev.*, 2024, **505**, 215677.
- 20 D. Ma, H. Bian, S. Long, P. Zhou, R. Tian, Y. Wu, H. Ge, M. Li, J. Du, J. Fan, Y. Zhang and X. Peng, *Sci. China Chem.*, 2022, **65**, 563–573.
- 21 L. Wu, C. Huang, B. P. Emery, A. C. Sedgwick, S. D. Bull, X. P. He, H. Tian, J. Yoon, J. L. Sessler and T. D. James, *Chem. Soc. Rev.*, 2020, **49**, 5110–5139.
- 22 Y. Zhou, L. Ma, A. V. Lunchev, S. Long, T. Wu, W. Ni, A. C. Grimsdale, L. Sun and G. G. Gurzadyan, *J. Phys. Chem. B*, 2021, **125**, 12518–12527.
- 23 Y. Zou, S. Long, T. Xiong, X. Zhao, W. Sun, J. Du, J. Fan and X. Peng, *ACS Cent. Sci.*, 2021, **7**, 327–334.
- 24 X. Hu, C. Zhu, F. Sun, Z. Chen, J. Zou, X. Chen and Z. Yang, *Adv. Mater.*, 2024, **36**, e2304848.
- 25 J. Xu, X. Zheng, T.-B. Ren, L. Shi, X. Yin, L. Yuan and X.-B. Zhang, *Coord. Chem. Rev.*, 2025, **528**, 216379.
- 26 J. W. Lee, J. S. Park, H. Jeon, S. Lee, D. Jeong, C. Lee, Y. H. Kim and B. J. Kim, *Chem. Soc. Rev.*, 2024, **53**, 4674–4706.
- 27 W. Wu, D. Mao, S. Xu, Kenry, F. Hu, X. Li, D. Kong and B. Liu, *Chem*, 2018, **4**, 1937–1951.
- 28 Y.-Y. Zhao, H. Kim, V.-N. Nguyen, S. Jang, W. Jun Jang and J. Yoon, *Coord. Chem. Rev.*, 2024, **501**, 215560.
- 29 X. Miao, W. Yao, R. Chen, M. Jia, C. Ren, H. Zhao, T. He, Q. Fan and W. Hu, *Adv. Mater.*, 2023, **35**, e2301739.
- 30 V. N. Nguyen, Y. Yan, J. Zhao and J. Yoon, *Acc. Chem. Res.*, 2021, **54**, 207–220.
- 31 Y. Wu, H. M. Wang, X. L. Hu, Y. Zang, J. Li, H. H. Han, X. P. He, S. E. Lewis, H. M. Ismail and T. D. James, *Chem. Soc. Rev.*, 2025, **54**, 12080–12141.
- 32 W. R. Algar and K. D. Krause, *Annu. Rev. Anal. Chem.*, 2022, **15**, 17–36.
- 33 S. Hohng, S. Lee, J. Lee and M. H. Jo, *Chem. Soc. Rev.*, 2014, **43**, 1007–1013.
- 34 A. N. Bader, S. Hoetzel, E. G. Hofman, J. Voortman, P. M. van Bergen en Henegouwen, G. van Meer and H. C. Gerritsen, *ChemPhysChem*, 2011, **12**, 475–483.
- 35 X. Zhang, Y. Bai, Y. Jiang, N. Wang, F. Yang, L. Zhan and C. Huang, *Anal. Methods*, 2021, **13**, 1489–1494.
- 36 F. Ali, E. Gehrman, T. Zhang, Q. Q. Kashif, R. K. Anand, D. L. Phillips and A. H. Winter, *Phys. Chem. Chem. Phys.*, 2025, **27**, 10730–10738.
- 37 Y. Liu, J. Zhao, A. Iagatti, L. Bussotti, P. Foggi, E. Castellucci, M. Di Donato and K.-L. Han, *J. Phys. Chem. C*, 2018, **122**, 2502–2511.
- 38 E. Sebastian and M. Hariharan, *Angew. Chem., Int. Ed.*, 2023, **62**, e202216482.
- 39 M. Kellogg, A. Akil, D. S. Muthiah Ravinson, L. Estergreen, S. E. Bradforth and M. E. Thompson, *Faraday Discuss.*, 2019, **216**, 379–394.
- 40 M. T. Whited, N. M. Patel, S. T. Roberts, K. Allen, P. I. Djurovich, S. E. Bradforth and M. E. Thompson, *Chem. Commun.*, 2012, **48**, 284–286.
- 41 M. Lv, Y. Yu, M. E. Sandoval-Salinas, J. Xu, Z. Lei, D. Casanova, Y. Yang and J. Chen, *Angew. Chem., Int. Ed.*, 2020, **59**, 22179–22184.
- 42 R. Montero, V. Martinez-Martinez, A. Longarte, N. Epelde-Elezcano, E. Palao, I. Lamas, H. Manzano, A. R. Agarrabeitia, I. Lopez Arbeloa, M. J. Ortiz and I. Garcia-Moreno, *J. Phys. Chem. Lett.*, 2018, **9**, 641–646.
- 43 E. Bassan, A. Gualandi, P. G. Cozzi and P. Ceroni, *Chem. Sci.*, 2021, **12**, 6607–6628.
- 44 M. H. Y. Cheng, K. M. Harmatys, D. M. Charron, J. Chen and G. Zheng, *Angew. Chem., Int. Ed.*, 2019, **58**, 13394–13399.
- 45 S. Wu, W. Zhang, C. Li, Z. Ni, W. Chen, L. Gai, J. Tian, Z. Guo and H. Lu, *Chem. Sci.*, 2024, **15**, 5973–5979.
- 46 Y. Yang, B. Sun, S. Zuo, X. Li, S. Zhou, L. Li, C. Luo, H. Liu, M. Cheng, Y. Wang, S. Wang, Z. He and J. Sun, *Sci. Adv.*, 2020, **6**, eabc1725.
- 47 K. Cai, X. He, Z. Song, Q. Yin, Y. Zhang, F. M. Uckun, C. Jiang and J. Cheng, *J. Am. Chem. Soc.*, 2015, **137**, 3458–3461.
- 48 X. He, X. Chen, L. Liu, Y. Zhang, Y. Lu, Y. Zhang, Q. Chen, C. Ruan, Q. Guo, C. Li, T. Sun and C. Jiang, *Adv. Sci.*, 2018, **5**, 1701070.
- 49 Y. Hou, J. Li, G. Jiang, T. Xia, Z. Li, H. Gu, X. Liu, Q. Yao, C. Zhang, W. Liu, J. Du, W. Sun, J. Fan and X. Peng, *Adv. Funct. Mater.*, 2024, **34**, 2316452.
- 50 J. Zhang, W. Wang, J. Shao, J. Chen and X. Dong, *Coord. Chem. Rev.*, 2024, **516**, 215986.
- 51 W. Feng, X. Mu, Y. Li, S. Sun, M. Gao, Y. Lu and X. Zhou, *Acta Biomater.*, 2024, **185**, 371–380.
- 52 A. S. Sherudillo, L. A. Antina and E. V. Antina, *Coord. Chem. Rev.*, 2025, **545**, 217030.
- 53 S. Wang, L. Gai, Y. Chen, X. Ji, H. Lu and Z. Guo, *Chem. Soc. Rev.*, 2024, **53**, 3976–4019.
- 54 V.-N. Nguyen, D. J. Lee, D. Zhang, J. Ha, K. M. K. Swamy, R. Wang, H. M. Kim, F. Yu and J. Yoon, *Chem. Mater.*, 2024, **36**, 5534–5541.
- 55 M. Broring, R. Kruger, S. Link, C. Kleeberg, S. Kohler, X. Xie, B. Ventura and L. Flamigni, *Chemistry*, 2008, **14**, 2976–2983.
- 56 B. Ventura, G. Marconi, M. Bröring, R. Krüger and L. Flamigni, *New J. Chem.*, 2009, **33**, 428–438.
- 57 X. Guo, B. Tang, Q. Wu, W. Zhong, Q. Gong, S. Ling, L. Jiao, X. Jiang and E. Hao, *ACS Appl. Mater. Interfaces*, 2024, **16**, 41916–41926.
- 58 Y. Hayashi, S. Yamaguchi, W. Y. Cha, D. Kim and H. Shinokubo, *Org. Lett.*, 2011, **13**, 2992–2995.
- 59 Z. Li, Y. Liu, X. Hou, Z. Xu, C. Liu, F. Zhang and Z. Xie, *J. Lumin.*, 2019, **212**, 306–314.
- 60 Y. Cakmak, S. Kolemen, S. Duman, Y. Dede, Y. Dolen, B. Kilic, Z. Kostereli, L. T. Yildirim, A. L. Dogan, D. Guc and E. U. Akkaya, *Angew. Chem., Int. Ed.*, 2011, **50**, 11937–11941.
- 61 X. F. Zhang and X. Yang, *J. Phys. Chem. B*, 2013, **117**, 9050–9055.
- 62 J. Cao, T. Zhang, X. Chen, X. Ma and J. Fan, *Smart Mol.*, 2025, **3**, e20240023.



- 63 T. Ozdemir, J. L. Bila, F. Sozmen, L. T. Yildirim and E. U. Akkaya, *Org. Lett.*, 2016, **18**, 4821–4823.
- 64 W. Pang, X. F. Zhang, J. Zhou, C. Yu, E. Hao and L. Jiao, *Chem. Commun.*, 2012, **48**, 5437–5439.
- 65 L. Guo, X. Guo, H. Zuo, H. Li, F. Lv, Q. Wu, L. Jiao and E. Hao, *ChemPhotoChem*, 2024, **8**, e202400100.
- 66 A. Prieto-Castaneda, F. Garcia-Garrido, C. Diaz-Norambuena, B. Escriche-Navarro, A. Garcia-Fernandez, J. Banuelos, E. Rebollar, I. Garcia-Moreno, R. Martinez-Manez, S. de la Moya, A. R. Agarrabeitia and M. J. Ortiz, *Org. Lett.*, 2022, **24**, 3636–3641.
- 67 K. X. Teng, W. K. Chen, L. Y. Niu, W. H. Fang, G. Cui and Q. Z. Yang, *Angew. Chem., Int. Ed.*, 2021, **60**, 19912–19920.
- 68 V.-N. Nguyen, J. Ha, C. W. Koh, B. Ryu, G. Kim, J. H. Park, C. Y. Kim, S. Park and J. Yoon, *Chem. Mater.*, 2021, **33**, 7889–7896.
- 69 L. Wang and Y. Qian, *Org. Biomol. Chem.*, 2023, **21**, 7339–7350.
- 70 L. Wang and Y. Qian, *J. Mater. Chem. B*, 2024, **12**, 6175–6189.
- 71 Q. Wu, Y. Zhu, X. Fang, X. Hao, L. Jiao, E. Hao and W. Zhang, *ACS Appl. Mater. Interfaces*, 2020, **12**, 47208–47219.
- 72 Z. Kang, W. Bu, X. Guo, L. Wang, Q. Wu, J. Cao, H. Wang, C. Yu, J. Gao, E. Hao and L. Jiao, *Inorg. Chem.*, 2024, **63**, 3402–3410.
- 73 S. Zhang, F. Zhang, Y. Gu, W. Zhang, M. Li, Y. Fan, X. Zhou and S. Zhu, *J. Org. Chem.*, 2025, **90**, 6146–6161.
- 74 Q. Gong, X. Zhang, W. Li, X. Guo, Q. Wu, C. Yu, L. Jiao, Y. Xiao and E. Hao, *J. Am. Chem. Soc.*, 2022, **144**, 21992–21999.
- 75 Q. Gong, Q. Wu, X. Guo, W. Li, L. Wang, E. Hao and L. Jiao, *Org. Lett.*, 2021, **23**, 7220–7225.
- 76 L. Wang, C. Cheng, C. Yu, Q. Wu, Z. Kang, H. Wang, L. Jiao and E. Hao, *Chem. Commun.*, 2024, **60**, 5054–5057.
- 77 X. Guo, J. Yang, M. Li, F. Zhang, W. Bu, H. Li, Q. Wu, D. Yin, L. Jiao and E. Hao, *Angew. Chem., Int. Ed.*, 2022, **61**, e202211081.
- 78 D. Yang, L. Sun, L. Xue, X. Wang, Y. Hu, J. Shao, L. Fu and X. Dong, *J. Innovative Opt. Health Sci.*, 2021, **15**, 2250004.
- 79 C. Zhao, T. Du, B. Zhu, Z. He, H.-Y. Wang and Y. Liu, *Coord. Chem. Rev.*, 2025, **544**, 216962.
- 80 S. Kolemen, M. Isik, G. M. Kim, D. Kim, H. Geng, M. Buyuktemiz, T. Karatas, X. F. Zhang, Y. Dede, J. Yoon and E. U. Akkaya, *Angew. Chem., Int. Ed.*, 2015, **54**, 5340–5344.
- 81 H. Chen, Q. Bi, Y. Yao and N. Tan, *J. Mater. Chem. B*, 2018, **6**, 4351–4359.
- 82 Q. Sun, J. Yang, Q. Wu, W. Shen, Y. Yang and D. Yin, *ACS Appl. Mater. Interfaces*, 2024, **16**, 127–141.
- 83 H. Huang, D. Ma, Q. Liu, D. Huang, X. Zhao, Q. Yao, T. Xiong, S. Long, J. Du, J. Fan and X. Peng, *CCS Chem.*, 2022, **4**, 3627–3636.
- 84 H. Huang, Q. Liu, J. H. Zhu, Y. Tong, D. Huang, D. Zhou, S. Long, L. Wang, M. Li, X. Chen and X. Peng, *Aggregate*, 2024, **6**, e706.
- 85 H. Gu, J. Zhang, P. Yuan, Z. Zheng, W. Liu, X. Xia, W. Sun, J. Du, J. Fan and X. Peng, *Chin. Chem. Lett.*, 2026, **37**, 111119.
- 86 H. Gu, P. Yuan, J. Zhang, X. Xia, Q. Pan, W. Liu, X. Zhao, W. Sun, J. Du, J. Fan and X. Peng, *J. Am. Chem. Soc.*, 2025, **147**, 20778–20789.
- 87 L. Li, N. El Islem Guissi, Y. Peng, S. Nie, H. Cai, C. J. Butch and Y. Wang, *Cell Rep. Phys. Sci.*, 2024, **5**, 101748.
- 88 X. Zhao, H. Zhao, S. Wang, Z. Fan, Y. Ma, Y. Yin, W. Wang, R. Xi and M. Meng, *J. Am. Chem. Soc.*, 2021, **143**, 20828–20836.
- 89 X. Zhao, Y. Ma, J. Di, Y. Qiao, J. Yu, Y. Yin, R. Xi and M. Meng, *ACS Appl. Mater. Interfaces*, 2024, **16**, 12310–12320.
- 90 J. F. Yu, J. Li and M. Li, *ACS Sens*, 2024, **9**, 3581–3593.
- 91 N. Kwon, G. O. Jasinevicius, G. Kassab, L. Ding, J. Bu, L. P. Martinelli, V. G. Ferreira, A. Dhaliwal, H. H. L. Chan, Y. Mo, V. S. Bagnato, C. Kurachi, J. Chen, G. Zheng and H. H. Buzza, *Angew. Chem., Int. Ed.*, 2023, **62**, e202305564.
- 92 X. Sun, Z. Zhang, M. Wang, Y. Chen, X. Meng, W. Zhao, J. Jin, W. Yang, C. Xia, Y. Wang, S. Li, B. Huang and N. Gu, *Nano Res.*, 2025, **18**, 94907281.
- 93 E. Feng, F. Lv, S. Tang, J. Du, S. Lv, Y. Wu, D. Liu, P. Zhou, F. Song and X. Peng, *Sci. China Mater.*, 2024, **67**, 3003–3011.
- 94 Y. Qiao, Y. Ma, Y. Tong, W. Liu, S. Wang, Y. Zheng, C. Men, J. Yu, J. Pan, D. Wan, Y. Yin, X. Zhao, R. Xi and M. Meng, *Small*, 2023, **19**, e2205248.
- 95 M. Wang, X. Wang, R. Wei, Y. Zhang, J. Chen, X. Luo, X. Qian and Y. Yang, *Sens. Actuators, B*, 2023, **394**, 134382.
- 96 X. Wang, J. Zhou, M. Wang, Y. Wang, Z. Shen, H. Sun, Z. Hu, X. Luo, Y. Yang and J. Chen, *Angew. Chem., Int. Ed.*, 2025, **64**, e202425422.
- 97 Z. She, R. Li, F. Zeng and S. Wu, *Adv. Healthcare Mater.*, 2024, **13**, e2400791.
- 98 Z. She, F. Zeng and S. Wu, *Biomater. Sci.*, 2025, **13**, 3006–3015.
- 99 Y. Lee, H. Jeong, H. Bian, Y. Li, J. Park, H. Xu and J. Yoon, *Sens. Actuators, B*, 2026, **449**, 139167.
- 100 Z. Zhu, L. Wei, A. K. Yadav, Z. Fan, A. Kumar, M. Miao, S. Banerjee and H. Huang, *J. Org. Chem.*, 2023, **88**, 626–631.
- 101 Y. Bu, T. Xu, X. Zhu, J. Zhang, L. Wang, Z. Yu, J. Yu, A. Wang, Y. Tian, H. Zhou and Y. Xie, *Chem. Sci.*, 2020, **11**, 10279–10286.
- 102 J. Wang, X. Zhu, J. Zhang, H. Wang, G. Liu, Y. Bu, J. Yu, Y. Tian and H. Zhou, *ACS Appl. Mater. Interfaces*, 2020, **12**, 1988–1996.
- 103 J. Wang, H. Li, Y. Zhu, M. Yang, J. Huang, X. Zhu, Z. P. Yu, Z. Lu and H. Zhou, *Chem. Sci.*, 2023, **14**, 323–330.
- 104 K. Dong, Y. Xu, Y. Tang and Q. Li, *Adv. Funct. Mater.*, 2025, **35**, 2504384.
- 105 Y. Tang, H. K. Bisoyi, X. M. Chen, Z. Liu, X. Chen, S. Zhang and Q. Li, *Adv. Mater.*, 2023, **35**, e2300232.
- 106 M. Yang, X. Li, G. Kim, R. Wang, S. J. Hong, C. H. Lee and J. Yoon, *Chem. Sci.*, 2022, **13**, 12738–12746.
- 107 H. A. Collins, M. Khurana, E. H. Moriyama, A. Mariampillai, E. Dahlstedt, M. Balaz, M. K. Kuimova, M. Drobizhev, V. X. D. Yang, D. Phillips, A. Rebane, B. C. Wilson and H. L. Anderson, *Nat. Photonics*, 2008, **2**, 420–424.
- 108 E. Dahlstedt, H. A. Collins, M. Balaz, M. K. Kuimova, M. Khurana, B. C. Wilson, D. Phillips and H. L. Anderson, *Org. Biomol. Chem.*, 2009, **7**, 897–904.
- 109 L. M. Mazur, T. Roland, S. Leroy-Lhez, V. Sol, M. Samoc, I. D. W. Samuel and K. Matczyszyn, *J. Phys. Chem. B*, 2019, **123**, 4271–4277.



- 110 J. Schmitt, S. Jenni, A. Sour, V. Heitz, F. Bolze, A. Pallier, C. S. Bonnet, E. Toth and B. Ventura, *Bioconjugate Chem.*, 2018, **29**, 3726–3738.
- 111 W. Zhang, W. Lin, X. Zheng, S. He and Z. Xie, *Chem. Mater.*, 2017, **29**, 1856–1863.
- 112 X. Zheng, L. Wang, S. Liu, W. Zhang, F. Liu and Z. Xie, *Adv. Funct. Mater.*, 2018, **28**, 1706507.
- 113 X. Li, K. Jeong, Y. Lee, T. Guo, D. Lee, J. Park, N. Kwon, J. H. Na, S. K. Hong, S. S. Cha, J. D. Huang, S. Choi, S. Kim and J. Yoon, *Theranostics*, 2019, **9**, 6412–6423.
- 114 R. Wang, K. H. Kim, J. Yoo, X. Li, N. Kwon, Y. H. Jeon, S. K. Shin, S. S. Han, D. S. Lee and J. Yoon, *ACS Nano*, 2022, **16**, 3045–3058.
- 115 Y. Zhao, K.-Q. Zou, W.-X. Zheng, C.-C. Huang, B.-Y. Zheng, M.-R. Ke and J.-D. Huang, *Dyes Pigm.*, 2022, **199**, 110037.
- 116 M. Z. Shafikov, C. Hodgson, A. Gorski, A. Kowalczyk, M. Gapińska, K. Kowalski, R. Czerwieńiec and V. N. Kozhevnikov, *J. Mater. Chem. C*, 2022, **10**, 1870–1877.
- 117 M. Z. Shafikov, R. Martinscroft, C. Hodgson, A. Hayer, A. Auch and V. N. Kozhevnikov, *Inorg. Chem.*, 2021, **60**, 1780–1789.
- 118 M. Z. Shafikov, P. Pander, A. V. Zaytsev, R. Daniels, R. Martinscroft, F. B. Dias, J. A. G. Williams and V. N. Kozhevnikov, *J. Mater. Chem. C*, 2021, **9**, 127–135.
- 119 M. Z. Shafikov, A. V. Zaytsev, A. F. Suleymanova, F. Brandl, A. Kowalczyk, M. Gapińska, K. Kowalski, V. N. Kozhevnikov and R. Czerwieńiec, *J. Phys. Chem. Lett.*, 2020, **11**, 5849–5855.
- 120 M. Z. Shafikov, R. Daniels and V. N. Kozhevnikov, *J. Phys. Chem. Lett.*, 2019, **10**, 7015–7024.
- 121 A. Barta, L. Vanwonderghem, M. Lavaud, F. Molton, G. Micouin, A. L. Bulin, A. Banyasz, J. L. Coll, F. Loiseau, A. Hurbin and P. H. Lanoe, *ACS Appl. Bio Mater.*, 2025, **8**, 4272–4284.
- 122 Z. Fan, Y. Rong, T. Sadhukhan, S. Liang, W. Li, Z. Yuan, Z. Zhu, S. Guo, S. Ji, J. Wang, R. Kushwaha, S. Banerjee, K. Raghavachari and H. Huang, *Angew. Chem., Int. Ed.*, 2022, **61**, e202202098.
- 123 Y. Liu, D. Zhu and Z. Xie, *ACS Med. Chem. Lett.*, 2021, **12**, 1374–1379.
- 124 Z. Wang, L. Wei, J. Lin, C. Huang, H. Chen, D. Fan, W. Hu, J. Liu, H. Huang, Z. Wang and X. Wang, *J. Med. Chem.*, 2024, **67**, 13435–13445.
- 125 L. Wei, R. Kushwaha, T. Sadhukhan, H. Wu, A. Dao, Z. Zhang, H. Zhu, Q. Gong, J. Ru, C. Liang, P. Zhang, S. Banerjee and H. Huang, *J. Med. Chem.*, 2024, **67**, 11125–11137.
- 126 A. Dao, S. Chen, L. Pan, Q. Ren, X. Wang, H. Wu, Q. Gong, Z. Chen, S. Ji, J. Ru, H. Zhu, C. Liang, P. Zhang, H. Xia and H. Huang, *Adv. Healthcare Mater.*, 2024, **13**, e2400956.
- 127 L. Xie, Z. Chen, T. Wang, J. Liang, Q. Lie, C. Jin, X. Zhang, Y. Chen and H. Chao, *Chem. Sci.*, 2025, **16**, 15045–15055.
- 128 J. Ru, Y. Chen, S. Tao, K. Xu, C. Liang, M. Kou, X. Tang and W. Liu, *Adv. Healthcare Mater.*, 2025, e01884, DOI: [10.1002/adhm.202501884](https://doi.org/10.1002/adhm.202501884).
- 129 T. Tan, T. Nakamura, R. Murdey, S. Hu, M. A. Truong and A. Wakamiya, *Chemistry*, 2023, **29**, e202300529.
- 130 H. Shimogawa, Y. Murata and A. Wakamiya, *Org. Lett.*, 2018, **20**, 5135–5138.
- 131 Z. Jiang, C. Zhang, X. Wang, M. Yan, Z. Ling, Y. Chen and Z. Liu, *Angew. Chem., Int. Ed.*, 2021, **60**, 22376–22384.
- 132 M. Yang, X. Ou, J. Li, J. Sun, Z. Zhao, J. W. Y. Lam, J. Fan and B. Z. Tang, *Angew. Chem., Int. Ed.*, 2024, e202407307, DOI: [10.1002/anie.202407307](https://doi.org/10.1002/anie.202407307).
- 133 S. Yang, J. Zhang, Z. Zhang, R. Zhang, X. Ou, W. Xu, M. Kang, X. Li, D. Yan, R. T. K. Kwok, J. Sun, J. W. Y. Lam, D. Wang and B. Z. Tang, *J. Am. Chem. Soc.*, 2023, **145**, 22776–22787.
- 134 H. Gu, W. Sun, J. Du, J. Fan and X. Peng, *Smart Mol.*, 2024, **2**, e20230014.
- 135 D. Zhou, G. Zhang, J. Li, Z. Zhuang, P. Shen, X. Fu, L. Wang, J. Qian, A. Qin and B. Z. Tang, *ACS Nano*, 2024, **18**, 25144–25154.
- 136 C. You, Y. Zhu, J. Zhu, Z. Xu, Q. Liu, L. Wang, W. Zhang, J. Hou, D. Wang and B. Zhong Tang, *Angew. Chem., Int. Ed.*, 2025, **64**, e202417865.
- 137 H. Li, Y. Gu, Y. Ding, J. Huang, Z. Yang, P. Ding, M. Wang, L. Han, B. Yang, L. Guo, Y. Zhang, F. He and L. Tian, *Angew. Chem., Int. Ed.*, 2025, **64**, e202423023.
- 138 H. Li, Q. Li, Y. Gu, M. Wang, P. Tan, H. Wang, L. Han, Y. Zhu, F. He and L. Tian, *Aggregate*, 2024, **5**, e528.
- 139 Z. Wang, C. Liu, X. Zou, W. Chi, Y. Zhang, X. Luo, Y. Xu, J. Liu, N. Zhao, W. Zhang, M. Zu, W. Yin, L. Meng and D. Dang, *Small*, 2025, **21**, e2411643.
- 140 L. Dou, H. Zheng, H. Xiong, S. Fu, C. Wang and D. Li, *Aggregate*, 2025, **6**, e70068.
- 141 S. Liu, C. Chen, Y. Li, H. Zhang, J. Liu, R. Wang, S. T. H. Wong, J. W. Y. Lam, D. Ding and B. Z. Tang, *Adv. Funct. Mater.*, 2019, **30**, 1908125.
- 142 Z. Zhang, H. Ye, F. Cai and Y. Sun, *Dalton Trans.*, 2023, **52**, 15193–15202.
- 143 F. Ding, Z. Chen, W. Y. Kim, A. Sharma, C. Li, Q. Ouyang, H. Zhu, G. Yang, Y. Sun and J. S. Kim, *Chem. Sci.*, 2019, **10**, 7023–7028.
- 144 W. T. Dou, H. B. Yang and L. Xu, *Acc. Chem. Res.*, 2025, **58**, 1151–1167.
- 145 Y. Sun, F. Ding, Z. Zhou, C. Li, M. Pu, Y. Xu, Y. Zhan, X. Lu, H. Li, G. Yang, Y. Sun and P. J. Stang, *Proc. Natl. Acad. Sci. U. S. A.*, 2019, **116**, 1968–1973.
- 146 Y. Y. Zhao, X. Zhang, Z. Chen, Y. Xu, H. Kim, H. Jeong, Y. R. Lee, J. Lee, X. Li and J. Yoon, *Aggregate*, 2024, **5**, e514.
- 147 B. Tang, W. L. Li, Y. Chang, B. Yuan, Y. Wu, M. T. Zhang, J. F. Xu, J. Li and X. Zhang, *Angew. Chem., Int. Ed.*, 2019, **58**, 15526–15531.
- 148 W. Liu, Z. Zhang, Q. Huang, R. Pai, L. Liu, Z. Ding, X. Wang and Z. Jin, *ACS Appl. Nano Mater.*, 2025, **8**, 21009–21018.
- 149 Z. Lei, Y. H. Song, Y. L. Leng, Y. J. Gu, M. Yu, Y. Chen, Q. Yu and Y. Liu, *J. Med. Chem.*, 2025, **68**, 5891–5906.
- 150 L. Tu, C. Li, Q. Ding, A. Sharma, M. Li, J. Li, J. S. Kim and Y. Sun, *J. Am. Chem. Soc.*, 2024, **146**, 8991–9003.
- 151 L. Tu, C. Li, X. Xiong, J. Hyeon Kim, Q. Li, L. Mei, J. Li, S. Liu, J. Seung Kim and Y. Sun, *Angew. Chem., Int. Ed.*, 2023, **62**, e202301560.
- 152 C. Li, L. Tu, J. Yang, C. Liu, Y. Xu, J. Li, W. Tuo, B. Olenyuk, Y. Sun, P. J. Stang and Y. Sun, *Chem. Sci.*, 2023, **14**, 2901–2909.



- 153 Y. Pang, Q. Li, J. Wang, S. Wang, A. Sharma, Y. Xu, H. Hu, J. Li, S. Liu and Y. Sun, *Angew. Chem., Int. Ed.*, 2025, **64**, e202415802.
- 154 G. Liang, H. Ren and J. Rao, *Nat. Chem.*, 2010, **2**, 54–60.
- 155 Y. Deng, K. Yan, L. Xu, X. Liu, F. Zhao, S. Wang, F. Zhang, G. Liang and R. Wang, *Chem. Commun.*, 2025, **61**, 544–547.
- 156 G. Gao, X. Sun, X. Liu, Y. W. Jiang, R. Tang, Y. Guo, F. G. Wu and G. Liang, *Adv. Funct. Mater.*, 2021, **31**, 2102832.
- 157 X. Hu, X. Sun, X. Liu, H. D. Xu, L. Yang, S. Liu, R. Wang and G. Liang, *Anal. Chem.*, 2023, **95**, 14511–14515.
- 158 X. Sun, L. Xu, H. D. Xu, L. Xie, R. Wang, Z. Yang, W. Zhan, S. Shen and G. Liang, *Adv. Healthcare Mater.*, 2024, **13**, e2303472.
- 159 C. Wang, W. Du, C. Wu, S. Dan, M. Sun, T. Zhang, B. Wang, Y. Yuan and G. Liang, *Angew. Chem., Int. Ed.*, 2022, **61**, e202114766.
- 160 L. Xu, H. Gao, W. Zhan, Y. Deng, X. Liu, Q. Jiang, X. Sun, J. J. Xu and G. Liang, *J. Am. Chem. Soc.*, 2023, **145**, 27748–27756.
- 161 Y. Deng, L. Xu, X. Liu, Q. Jiang, X. Sun, W. Zhan and G. Liang, *J. Am. Chem. Soc.*, 2024, **146**, 25462–25466.
- 162 W. Du, Y. Chong, X. Hu, Y. Wang, Y. Zhu, J. Chen, X. Li, Q. Zhang, G. Wang, J. Jiang and G. Liang, *Adv. Funct. Mater.*, 2019, **30**, 1908073.
- 163 Y. Wang, W. Du, T. Zhang, Y. Zhu, Y. Ni, C. Wang, F. M. Sierra Raya, L. Zou, L. Wang and G. Liang, *ACS Nano*, 2020, **14**, 9585–9593.
- 164 B. Diao, S. Shi, J. Li, L. Yang, L. Zheng, H. Guo and X. Peng, *Adv. Mater.*, 2025, e15813, DOI: [10.1002/adma.202515813](https://doi.org/10.1002/adma.202515813).

